UNIVERSITÉ DE SHERBROOKE

Faculté de génie

Département de génie électrique et de génie informatique

CONVERTISSEURS À BOBINE VARIABLE POUR APPLICATIONS DE TRANSPORT DURABLES

VARIABLE INDUCTOR BASED CONVERTERS FOR SUSTAINABLE TRANSPORTATION

Thèse de doctorat

Spécialité : génie électrique

Mebrahtom W. Beraki

Jury João P. F. Trovão (Directeur)

Ta Cao Minh

François Boone

Marina Perdigão

Dhaker Abbes

Sherbrooke (Québec) Canada April 2020

MEMBRES DU JURY

M. João Pedro F. TROVÃO, Directeur

Professeur Agrégé, Université de Sherbrooke (UdeS), QC, Canada

M. Minh C. Ta, Évaluateur

Professeur Agrégé, Université de Sherbrooke (UdeS), QC, Canada

Mme. Marina Perdigão, Évaluateur

Adjunct Professor, ISEC, Polytechnic of Coimbra, Portugal

M. Dhaker ABBES, Évaluateur

Enseignant – Chercheur HDR, Département EEA , HEI, une école d'Yncréa Hauts-de-France, France

M. François Boone, Rapporteur

Professeur Titulaire, Université de Sherbrooke (UdeS), QC, Canada

Acknowledgement

My most sincere gratitude to my supervisor Professor Joao Pedro Trovao for giving me the opportunity to conduct my PhD research at the e-TESC lab. I am also very thankful for his diligent guidance, continuous support, encouragement, and invaluable mentoring throughout this thesis work. I am so grateful for everything I learned from him through my PhD time.

I would like also to express my gratitude to Canada Research Chairs Program (Grant 950-230672) and the Natural Sciences and Engineering Research Council of Canada (Grant RGPIN-2017-05924), Arbour Foundation Scholarship, and University of Sherbrooke Faculty of Engineering Excellence Scholarship for their financial support during this study.

I wish to express my sincere appreciation to the jury members, Prof. François Boone, Prof. Minh Ta Cao, Prof. Marina Perdigão, and Prof. Dhaker Abbes for their encouragement, invaluable comments, and insightful questions.

I am also indebted to give my sincere appreciation to Professor Marina Perdigão, for the continuous collaboration. Professor Marina`s input on the revision of our research papers and continuous constructive feedback is worth appreciated.

I would like to express my deep gratitude to e-TESC lab members, colleagues, and friends. A special thanks to my friend Ahmad Shah Mohammadi and his wife Zara Akbari, who were always the source of my energy to push forward and I am deeply grateful for all their support and motivations.

I would like to express my heartfelt appreciation to my family members and friends for their unconditional love, patience, and constant encouragement.

Last but not least, my special thanks and appreciation goes to my wife Yordanos T. Kahsay and my daughters Elda, Sidon and Ruth for their unconditional love, continuous motivation and patience throughout my studies.

Résumé

Les convertisseurs d'électroniques de puissance sont des composants clés de la conversion et gestion efficace de l'énergie électrique dans une large gamme d'applications. Pour des utilisations véhiculaires, il est inévitablement nécessaire d'améliorer leurs performances et de réduire leur taille. Ceci est particulièrement important dans le cas des convertisseurs à courant continu (CC) de la chaine de traction où des performances améliorées en réponse à une large gamme de variations de charge sont recherchées tout en respectant les spécificités, caractéristiques et limitation d'espace nécessaires aux véhicules électrifiés. Ces objectifs définissent une cible de recherche et en particulier des progrès sont essentiels dans le domaine des composants passifs, des dispositifs semi-conducteurs, des topologies des convertisseurs et leurs commandes pour généraliser l'utilisation de véhicules électriques. Les composants passifs, en particulier les inductances de puissance, sont des composants dominants qui affectent le volume global, le coût et les performances de ces convertisseurs d'électroniques de puissance.

Compte tenu de ces aspects, cette thèse propose un concept de bobine variable afin de réduire le poids et la taille des inductances de puissance qui sont traditionnellement encombrantes et ont une gamme de fonctionnement assez limitée. En modulant la perméabilité du matériau magnétique, ce concept améliore la capacité de gestion du courant des bobines de puissance, contrôle les ondulations du courant et réduit les pertes magnétiques et par commutation, bien comme les contraintes appliquées aux dispositifs de commutation. En outre, il permet l'utilisation de noyaux plus petits, ce qui entraîne une réduction de masse et de volume, en permettant une amélioration du fonctionnement du convertisseur et de ses performances globales. Cependant, pour l'intégrer aux convertisseurs CC-CC utilisés dans la chaine de traction, il est fondamental de se questionner sur la conception du composant lui-même, la sélection du matériau magnétique, la commande du courant de l'enroulement auxiliaire et la gestion de la saturation du noyau magnétique. Cette thèse aborde de manière systématique ces différents défis de recherche.

Une attention particulière est accordée à l'étude expérimentale d'un prototype de bobine variable pour faire la preuve de concept à petite échelle afin d'explorer sa viabilité. Par la suite, une large caractérisation par éléments finis a été développée pour déterminer le fonctionnement intrinsèque de ce composant passif. De plus, cette thèse propose une méthode systématique de design de bobine variable basée sur le courant RMS pour réduire le surdimensionnement traditionnellement associer aux inductances de puissance pour des applications véhiculaires. Dans cette méthodologie, la sélection appropriée du matériau pour le noyau magnétique est une étape cruciale pour garantir des convertisseurs plus petits et efficaces, donc une démarche de sélection simplifiée basée sur la méthode des propriétés pondérées pour le choix de noyau magnétique approprié au besoin de l'application a été mis au point.

De plus, pour valider l'intégration de ce concept dans une topologie de convertisseur CC-CC traditionnellement utilisée dans la chaine de traction des véhicules électrifiés, une méthode de synthèse affine a été utilisée pour définir les paramètres des contrôleurs de courant et une stratégie de gestion de la saturation du noyau a été proposée pour permettre le contrôle dynamique de la

bobine variable. La commande du convertisseur et la stratégie ont été évaluées par simulation d'une chaine de traction complète d'un véhicule récréatif réel.

Les résultats expérimentaux à petite échelle et simulations à pleine échelle ont démontrés des capacités intéressantes de cette bobine variable pour l'amélioration des performances des convertisseurs CC-CC, ayant la capacité de gestion de la saturation du noyau magnétique tout en réduisant la taille et le poids de ces composants passifs, dans le but de son utilisation dans la chaine de traction des véhicules électrifiés.

Mots-clés: Synthèse affine, processus de hiérarchie analytique, véhicule électrique, analyse par éléments finis, matériaux de noyau magnétique, convertisseur CC-CC, bobine variable, transport durable, méthode de la propriété pondérée.

Abstract

Power electronics converters are key components and enable efficient conversion and management of electrical energy in a wide range of applications. For vehicular use, there is an inevitable need to improve their performance and reducing their size. This is particularly important in case of powertrain DC-DC converters as they are required to have improved performance while respecting the specifications, characteristics and stringent space limitations. These objectives define research targets and a particular progress is essential in the field of passive components, semiconductor devices, converter topologies and control. At the current state of technologies, the passive components particularly the power inductors are dominant components which affect the overall volume, cost and performance of power electronic converters.

Considering the aforementioned critical aspects, this thesis proposes a variable inductor (VI) concept in order to reduce the weight and size power inductors which are traditionally bulky and have fairly limited operating range. By modulating the permeability of the magnetic material, this concept enhances the current handling capability of power inductors, controls the current ripples, reduces the magnetic and switching losses, as well as the stresses applied to switching devices. Furthermore, it enables the use of smaller cores which leads to the reduction of mass and volume allowing improvements in the converter operation and its overall performance. However, to integrate it into powertrain DC-DC converters, it is fundamental, to question the design of the component itself, the selection of suitable magnetic core materials, and the control of current in the auxiliary winding and saturation management of magnetic cores. This thesis systematically addresses these different research challenges.

A particular attention is paid to the experimental study of a VI prototype to demonstrate the concept on a small-scale in order to explore its viability. Subsequently a detailed characterization was developed using finite element analysis to determine the intrinsic functionality of the passive component. Furthermore, this thesis proposed an RMS current based VI design to reduce oversizing of power inductors for electric vehicles application. In this methodology, the selection of a suitable magnetic core material is a crucial step to assure smaller and efficient converters. Hence, this thesis proposes a simplified approach based on weighted property method (WPM) for an appropriate selection of magnetic core in accordance to the needs of the user.

Furthermore, to validate the integration of this concept in DC-DC converter topology used in the powertrain of electrified vehicles, an affine parameterization method is used to design the control parameters and a simple management strategy is proposed to enable dynamic control of the VI. The converter control and the proposed strategy are evaluated through simulations of a complete powertrain of a three-wheel recreational vehicle.

The small-scale experimental and simulations, and full-scale simulations have demonstrated an interesting capacity of the VI for improving the performance of DC-DC converters for electrified vehicles and manage the saturation of the magnetic core while reducing the size and weight of magnetic components.

Keywords: Affine parameterization, analytical hierarchy process, electric vehicle, finite element analysis, magnetic core materials, powertrain DC-DC converter, variable inductor, sustainable transportation, weighted property method.

Table of Contents

Nomenclature

Variables

A_c	Cross-sectional area of the core
A_{mcu}	The cross-sectional area of the main winding
A_{pdes}	Desired Area product
A_{S_area}	The total surface area of the core
B	Magnetic field density
B_1	The magnetic field density in core 1
B_2	The magnetic field density in core 2
B_{max}	Maximum Flux density
B_{sat}	Saturation flux density
d_{dc}	Diameter of the control winding wires
D_{max}	Maximum Value of the duty cycle
D_{min}	Minimum Value of the duty cycle
D_{nom}	Minimum Value of the duty cycle
E	Strip width
E_s	Energy stored in the power inductor
H	Magnetic field intensity
H_1	Magnetic field intensity of core 1
H_2	Magnetic field intensity of core 2
I_b	Auxiliary winding current
$I_{b_{RMS}}$	Auxiliary winding RMS current
$I_{spk,i}$	Peak current across the i^{th} switch
I_{RMS}	Inductor current RMS value
i_s	Main winding current
Δi_s	Inductor current ripple

Δi_{spk} Peak to peak current ripple

I_{srms} Main winding RMS current

i_{s_sat} Main winding saturation current

J Current density

K, x and y Steinmetz parameters

K_{gp} Gap loss coefficient

K_{ns} A factor to consider the non-sinusoidal nature of the waveform for power converters

K_p^b Proportional gain of the auxiliary winding current controller

K_p^c Proportional gain of the current controller (PI)

K_p^v Proportional gain of the voltage controller (PI)

K_i^b Integral gain of the auxiliary winding current controller

K_i^c Integral gains of the current controller (PI)

K_i^v Integral gains of the voltage controller (PI)

K_u Window utilization factor

K_{ua} Actual window utilization factor

l Mean length of the magnetic core

L_{dif} Differential inductance

l_g Length of the air gap

L_m Main winding inductance

L_s Inductance of the power inductor

L_{min} Minimum value of inductance

M Mutual inductance

M_{core} Mass of the core material

MLT_b Mean length a single turn of the auxiliary winding

MLT_m Mean length a single turn of the main winding

N_b Auxiliary winding number of turns

N_m The main winding number of turns

P_{copper} Copper losses of the power inductor

P_{nom} Nominal power

P_{core} Core losses

P_{L_Total} Total losses in the power inductor

r Current ripple factor

R_{Lm} Resistance of the main winding

R_{Lb} Auxiliary winding, the resistance

T_s Switching period

ΔT Temperature rise

V_b Voltage induced in the auxiliary winding

V_{dc} Average DC-link voltage

$V_{dcpk,i}$ The peak voltage across the i^{th} switch

V_m Voltage induced in the main winding

V_o Output voltage range

V_{o_nom} Nominal output voltage

V_s Input voltage

V_{s_min} Minimum value of input voltage

V_{s_nom} Nominal input voltage

ΔV Voltage ripple

W_{am} Area occupied by the main winding conductors

W_{a_eff} Effective window area

Greek symbols

β Scaling factor

γ Performance Index

ζ Damping factor, and z is the zero

δ Skin depth

λ_1 Flux linkage in core 1

λ_2 Flux linkage in core 2

μ Permeability of the core material

μ_1 Permeability of core 1

μ_2 Permeability of core 2

ω_n Undamped natural frequency

Abbreviations

AHP	Analytical hierarchy processes
CCM	Continuous Conduction Mode
CO_2	Carbon Dioxide

CR	consistency ratio
EMI	Electromagnetic interference
ESS	Energy Storage System
e-TESC	e-Transport, Energy Storage and Conversion
EV	Electric vehicles
FEA	Finite Element Analysis
FEM	Finite Element Method
HEV	Hybrid electric vehicles
IC	Integrated Circuits
IGBT	Insulated Gate Bipolar Transistor
GHG	greenhouse gas
MMF	magnetomotive force
MOSFET	Metal-Oxide Semiconductor Field-Effect Transistor
NMPZ	Non-minimum phase zero
PI	Proportional-integral
PID	Proportional-integral-and derivative
PWM	Pulse width Modulation
RMS	Root mean Square
Si	Silicon
SSP	Switching stress parameter
VI	Variable Inductor
WBG	Wide band gap
WPM	Weighted Property Method

List of Figures

List of Tables

Chapter 1 Introduction

1.1 Background and Context

Our world is witnessing urgent and growing threats of climate change. This is mainly due to greenhouse gases (GHGs) emission leading to global warming, resulting in environmental and health risks. The scope and intensity of these risks will increase and it will be a significant threat for the generations to come [1]. Hence, sustainable actions are needed to deal with this global issue. The transportation sector, which uses about 20% of the global primary energy (Figure 1.1), emits about 8.6 Gt of CO_2e per year. The scale of this sector is expected to grow at a faster pace due to growing demand of vehicles. This demand represents incredible challenges in exacerbating climate change threats and energy scarcity [2]. Furthermore, the mercurial costs of fossil fuels and their future uncertainty puts additional pressure on the socio-economic development of our world. To tackle these global problems, there is a growing interest for the development of environmentally friendly and efficient electrified vehicles.

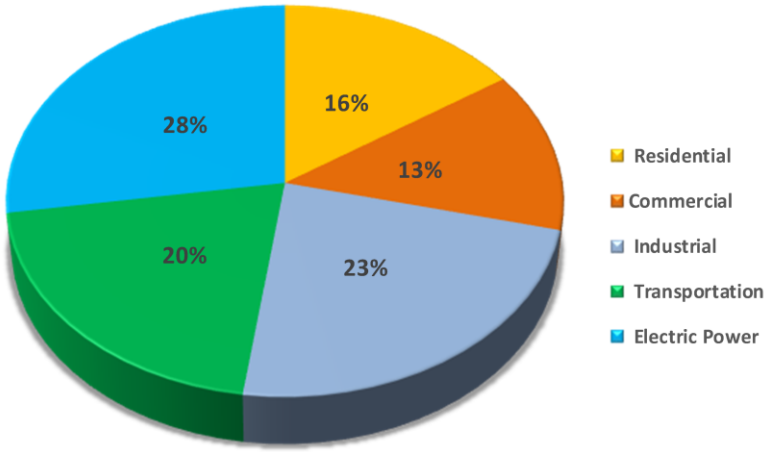

Figure 1.1: Global Energy Consumption by Sector in 2018 [3].

Electrified vehicles help in reducing GHG emission and fossil fuel reliance leading to worth recording health, economic and environmental benefits [4], [5], [6]. Furthermore, they will play a significant role in the transformation of the transportation sector to meet the global sustainable development goals. Subsequently, several countries and institutions are setting lofty goals to reduce and finally end the sale of gas and diesel powered vehicles starting from 2040 [7]. Hence, the electrified vehicles market is showing a promising trend in the automotive industry. The global

sales of electrified vehicles exceeded 5.1 million in 2018 [8]. The trend is expected to increase faster due to stringent CO_2 regulations, plummeting battery prices and global awareness.

The aforementioned reasons have driven an increased interest in research and innovations to increase the rate of transportation electrification. Major emphasis is given to reducing the size, weight, volume, cost and enhancing the performance of energy storage systems, power converters and electric motors. In this context, significant improvements are achieved in terms of reducing the cost, improving the performance and reducing the cost of power electronic converters, electric motors and energy storage systems [9]. Nonetheless, still there is a long way and additional research is needed to increase the penetration of electrified vehicles for long lasting impact of the transportation sector electrification.

This thesis focuses on accelerating this trend by developing more efficient, more compact and more reliable power electronic converters for electric vehicles. Power electronic converters are required for processing, controlling and conversion electrical energy in electrified vehicles. They are key enabling technologies for achieving fuel economy, reducing CO_2 emission goals and oil reliance. Next to the energy storage systems, the power electronic converters are the most expensive and they dominate the size and weight. Furthermore, they are the most vital components as they are used as a bridge for charging the energy sources, delivering power to traction motor and auxiliary converters. Therefore, there is a critical need to improve their performance, reduce their size, weight and cost. In electrified vehicles, smaller size and higher performance power converters are key requirements, and they are influenced by circuit components such as passive components. This mandates innovations, in converter topologies, control, materials, passive (inductors and capacitors) and active components. The size and weight of power electronic converters in EVs is dominated by the bulky and saturation limited power inductors. Hence, reducing their size and weight and controlling their saturation behavior provides an opportunity in addressing the aforementioned issues and introduces a challenge of controlling and integrating it to existing and new converter topologies.

This research seeks a practical solution for scaling down the size of magnetic components by controlling the saturation of magnetic core materials using the variable inductor concept, in order to reduce size and enhance the performance of EV converters. The size reduction of the magnetic

component is achieved using a small dc current injected in an auxiliary winding of the magnetic component. The small dc current in the auxiliary winding will be used to control of the saturation characteristics of the magnetic core enabling it to operate in different conditions leading to the enhancement of the current handling capability of the magnetic core. This adds a major merit in magnetic core optimization, converter operation and performance enhancement. However, it introduces realization, modeling, characterization, design and suitable magnetic materials selection challenges. Furthermore a closed loop control of the overall system and a strategy are vital for the integration of the VI in power electronic converters for electrified vehicles. This thesis systematically addresses these different research challenges.

This thesis is completed at the electric – Transport, Energy Storage and Conversion Laboratory (e-TESC Lab.), University of Sherbrooke, Quebec, Canada. It is part of the Canada Research Chair in Efficient Electric Vehicles with Hybridized Energy Storage Systems aiming at improving the efficiency and performance of the components of EVs and HEVs. The Chair has four research axes focused on energy management, design and control of electrical machines, design, control and development of power electronic converters for EV applications and energy storage systems. This PhD thesis is under the power electronics axis focused on the size and weight reduction and performance of enhancement of the DC-DC converters for sustainable transportation application. A schematic summary is provided in Figure 1.2.

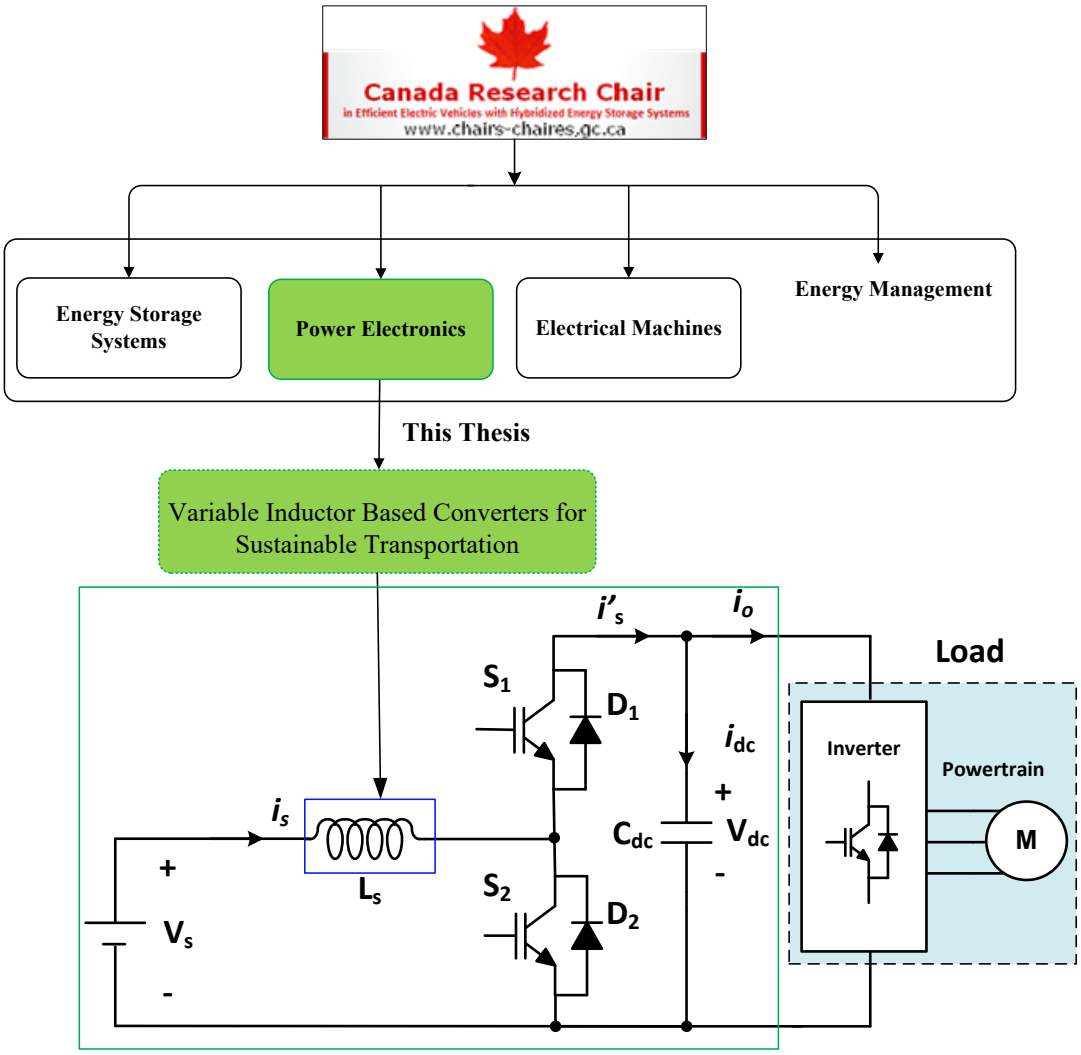

Figure 1.2: Context and position of the thesis at e-TESC lab

1.2 General Overview of the Study System

The overall schematic diagram for illustrating the powertrain of an electric vehicle and the main components that make up the complete system is depicted in Figure 1.3. It is composed of ESSs, bidirectional DC-DC converter, a DC-DC converter for powering up the auxiliary components, an inverter (DC/AC) a powertrain (consisting of an electric motor and the drivetrain) and the control [10].

The energy storage systems could be battery, supercapacitor, flywheel, fuel cell or else a combination based on the specific requirements. Due to the wide range load variations in typical EVs, none of these technologies can fulfil power demand of EVs independently [11]. Coupling multiple ESS with complementary characteristics is essential to meet higher load demands or driving range.

The power electronics converters play a key role in obtaining adjustable speed performances. The bidirectional DC-DC converter is the heart of the electric drive system, and it is used for converting, regulating, transferring and interfacing the low voltage from the ESSs to the high voltage dc-link in the propelling mode and vice-versa in the regenerative mode. Furthermore, the DC-DC converter connected to the accessories is used to provide power to the auxiliary components of the EV. The inverter (DC-AC converter) is used to convert DC supply into multiphase AC supply to drive the drivetrain of an EV.

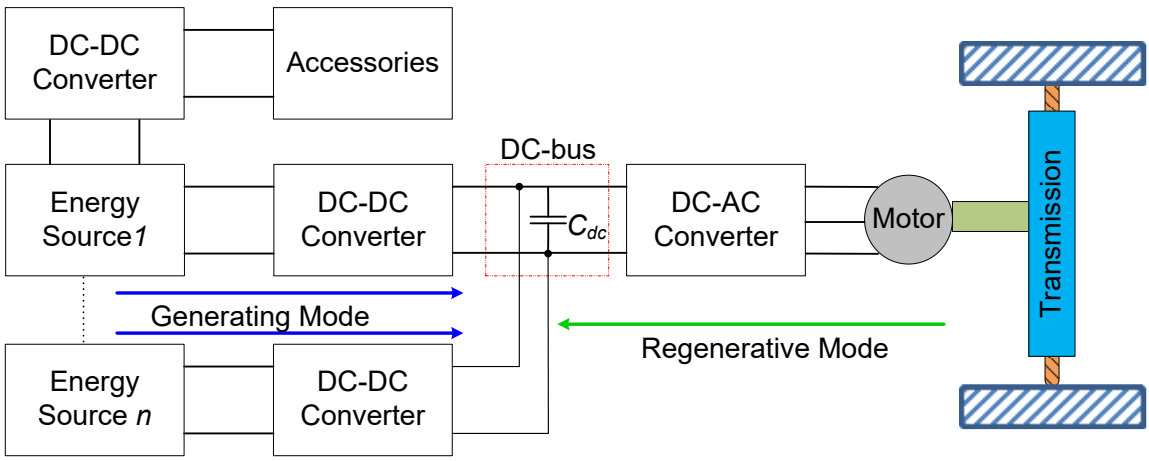

Figure 1.3: Schematic diagram of electric drive components

The electrical motor provides the rotational speed and torque to the mechanical load to propel the EV system. . The transmission system converts the motor torque into a higher torque value in order to turn the wheels. In EVs, the mechanical load is composed of the road characteristics, the wheels, the vehicle components and passengers' masses. The control system is governed by control algorithms and is used to control the key variables of an EV such as rotational speed, torque, currents and voltages.

In all the aforementioned converters, the magnetic component and the capacitor are very vital and dominant components. They significantly influence the size, weight, cost and performance [12]. As such, this thesis aims at the miniaturization of the bidirectional DC-DC converter, improving the current handling capability of the power inductor and enhancing the performance of the converter by managing the saturation level of the power inductor.

1.2.1 Half-bridge Bidirectional DC-DC Converter

The thesis is based on a half-bridge DC-DC converter shown in Figure 1.4. It is composed of an energy storage system (ESS), a half-bridge DC-DC converter, dc-link capacitor, the powertrain of an EV and the control layer. To reduce the size of such type of converters, the saturating power inductor is replaced with a VI. The VI is composed of two windings, the main winding and the auxiliary winding (for providing controlled current to regulate the saturation level of the main winding). This enable the control of the saturation of the power inductor in such bidirectional DC-DC converters.

The control layer includes the controllers for the bidirectional converter and a strategy for the auxiliary winding of the VI. The function of the dc-link controller is to maintain the dc-link voltage at the desired levels, attenuate ripple current, reduce EMI and suppress surge voltage caused by leakage inductance and switching operations [13]. Furthermore, it decouples the DC voltage source and provides low impedance path for ripple currents associated with the inverter. In motoring mode, the DC-link voltage tends to fall to provide more power to the load but in case of regeneration mode, the DC-link voltage tends to increase, hence the DC-link controller helps in regulating the DC-link voltage for the smooth operation of the vehicle in different modes of operation [14].

The current controller of the bidirectional DC-DC converter monitors the current to be delivered by the ESSs during propelling mode of operation and vice-versa in regenerative mode. This converter topology is selected due to its worth recording benefits in simplicity. The management strategy layer is used for determining the modes of operation of the VI and the amount of auxiliary winding current needed by the auxiliary winding in order to regulate the magnetic properties of the variable inductor.

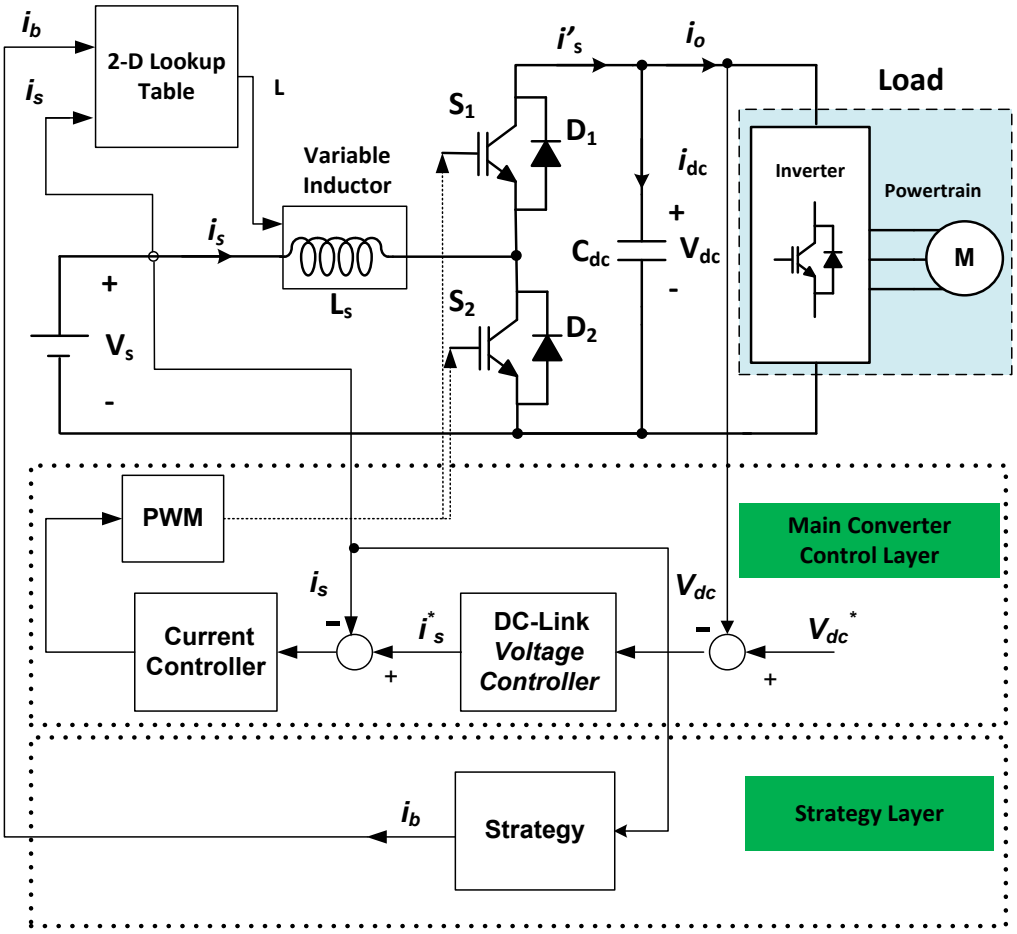

Figure 1.4: Schematic Diagram of the Study System

1.2.2 Variable Inductor

The variable inductor (VI) is a current controlled magnetic device [15], [16]. Unlike classical power inductors, it is composed of two groups of windings (main and auxiliary). The main winding carries the main winding current and the auxiliary winding is used for providing a small dc current. The small current in the auxiliary winding is used for adjusting the magnetic property of the magnetic core in the B-H curve. The principle of operation of the VI concept is based on the fundamental electromagnetism laws. It can be illustrated with the simplest VI topology shown in Figure 1.5.

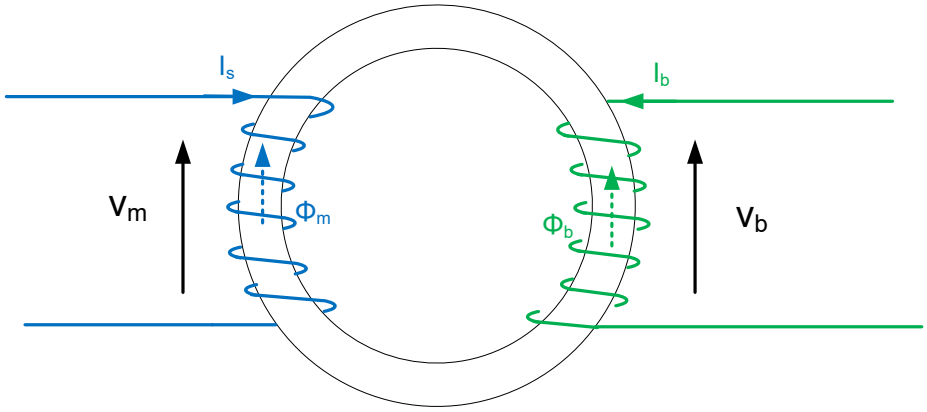

Figure 1.5: Simple VI configuration with one main and one auxiliary windings

Using Ampere's law, the flux intensity as a function of both the main winding and auxiliary winding parameters such as the number of windings and currents of each winding can be written as:

$$H = \frac{N_m i_s - N_c i_b}{l} \tag{1.1}$$

where H, N_m, i_s , N_c, i_b and l are the magnetic field intensity of the magnetic core, the total main winding number of turns, the main winding current, the auxiliary winding total number of turns, the auxiliary winding current and the mean length of the magnetic core in respective order.

The magnetic flux density, B and the magnetic field intensity, H, are related by the permeability of the material, μ, as:

$$B = \mu H \tag{1.2}$$

The total flux of a magnetic coil multiplied by the number of turns gives the flux linkage (λ).

$$\lambda = N_m \oint B dA = N_m B A \tag{1.3}$$

Replacing B in (1.3) by (1.2), the linkage flux (λ) can be written as:

$$\lambda = N_m \mu H A \tag{1.4}$$

Rewriting the magnetic flux intensity in terms of the main current and auxiliary current, the flux linkage in the magnetic core can be expressed as:

$$\lambda = N_m \mu A \left(\frac{N_m i_s - N_c i_b}{l}\right) \tag{1.5}$$

From the flux linkages in (1.5) the apparent (absolute) inductances L of the main windings can be calculated as shown in (1.6).

$$L = \frac{\lambda}{i_s} \tag{1.6}$$

Replacing λ in (1.6) with (1.5) the inductance can be written as:

$$L = \frac{N_m \mu A \left(\frac{N_m i_s + N_c i_b}{l}\right)}{i_s} \tag{1.7}$$

As clearly shown in (1.7), the inductance depends up on several variables. To vary the inductance, it is required to change any of the variables revealed in (1.7). The number of turns, the cross-sectional area and the mean length depend on the geometry of the magnetic material and require moving or replacing parts to adjust the inductance. Hence, it is cumbersome to change one of these parameters. However, the control current can be easily controlled to adjust the permeability of the material leading to the change of effective inductance by changing the core material property instead of the physical structure. From (1.7), it can be shown that the inductance of a magnetic material depends up on the permeability of the magnetic core and it depends up on the magnetomotive force (MMF). Hence, by changing the MMF either by adding to the main winding MMF or by subtracting from the main winding MMF, the permeability of the magnetic core can be modified, hence it can be used to adjust the effective inductance of the main power inductor.

The topology presented in Figure 1.5, is simple and suitable to illustrate the VI concept and its principle of operation. Nonetheless, it is prone to parametric coupling between the two windings. The parametric coupling leads to higher voltage induced in the auxiliary winding that can damage the auxiliary winding circuit. These phenomena of this configuration can be clearly shown with analytical expressions.

The voltage induced in the main winding can be expressed as:

$$v_m(t) = L_m \frac{di_m(t)}{dt} - M \frac{di_b(t)}{dt} \tag{1.8}$$

In a similar manner, the voltage induced in the auxiliary winding can be expressed as in (1.9):

$$v_b(t) = L_b \frac{di_b(t)}{dt} - M \frac{di_m(t)}{dt} \tag{1.9}$$

where L_m , M, i_m, and i_b are the main winding inductance, the mutual inductance, the main winding current and the auxiliary winding current in respective order. By keeping the auxiliary winding current constant, the voltage induced in the main winding due to the auxiliary winding and its effects can be minimized. Nonetheless, as the current in the main winding is quite large and it is varying in nature, there will be an induced voltage in the auxiliary winding due to the main winding current. At times, it can be very large and can damage the auxiliary circuit. To overcome the aforementioned issue, several topologies are proposed in literature. In this thesis a two magnetically decoupled cores based VI topology is used in order to avoid the parametric coupling in the magnetic device. The detailed studies of the topology, its operation and detailed characterization are presented in [17].

1.3 Scope and Objectives

The focus of this thesis is to improve the performance of bidirectional DC-DC converters in traction systems while reducing the size, cost and volume. Particular emphasis is given to the bulky power inductor. The conventional power inductor is replaced with a two winding VI, where one winding is used to regulate the magnetic property of the magnetic material in order to adjust its permeability using a small control current. A small current is used to produce a magnetic field in opposing direction to the main winding; hence delaying its saturation. This enhances the current handling capability of the magnetic material, which means a magnetic core designed for small currents can be used for higher currents. The reduction in the magnetic material with this approach mitigates the critical weight issue and enables more compact integrated design and implementation

of power electronic converters. The small DC current in the auxiliary winding provides control of the saturation characteristics of the magnetic core. However, it introduces realization and control challenges. To this end, this thesis provides detailed characterization of the current controlled magnetic device (VI) in order to understand its operation for addressing its challenges of integrating in power electronic converters. Furthermore, a systematic design procedure is proposed in order to benefit from the feature of the current controlled magnetic device. Besides, a closed loop control system, which consists of the converter control and a strategy to determine the operation of the device is developed and verified with simulations for large scale powertrain DC-DC power conversion.

The main objectives of this thesis are:

- ✓ To explore a way of improving the existing practices of building DC-DC converters for the next generation electrified vehicles by incorporating the VI.
- ✓ To provide detailed experimental and simulation characterization of the small-scale VI to demonstrate the concept to explore its viability, its intrinsic functionality and to extract essential parameters for integrating it to power electronic converters.
- ✓ To provide a systematic design procedure of VI for electrified vehicles and selection of suitable magnetic core materials for powertrain DC-DC converters.
- ✓ To develop a dynamic model of the device considering the target application and accordingly develop an integrated closed loop control with a strategy to enable continuous regulation of the magnetic properties of the VI.

1.4 Contributions

The main contributions of this work are summarized, and the detailed contributions are included in five published papers.

1. Experimental Characterization of a small-scale proof of concept VI (IEEE TVT 2017)
2. Characterization of VI using the FEM simulations in order to investigate its viability and to extract essential parameters for its integration to power electronic converters (SIMPAT 2019).

3. A systematic design of VI and selection of suitable magnetic core materials (IET EST 2019 and IEEE ISIE 2019).
4. Modeling of VI considering the target application and accordingly develop an integrated closed loop control and a simple strategy to enable continuous regulation of the magnetic properties of the VI (IET EST 2020)

1.5 Outline of the thesis

This thesis presents the use of VI concept to control saturation of magnetic cores to enable size and volume reduction and performance enhancement of power electronic converters for electrified vehicles. It is organized into eight chapters.

The first chapter provides a general introduction, overview of the study system, the objectives and main contributions of the thesis.

Chapter 2 provides the detailed literature review on bidirectional DC-DC converters for EV applications, Wide Band Gap (WBG) switching devices and VI topologies and applications for the purpose of enhancing the efficiency and reducing the volume, weight and cost of the power train DC-DC converters.

The third chapter presents the experimental characterization of a VI in regards, its current ripple control capability and its control, and its integration in a small-scale prototype.

Chapter 4 provides the characterization of VI to verify its suitability for DC-DC converters with wide range of load variations using Finite Element Analysis tool MagNet Infolytica software. The inductance characterization, the losses and improvements in the saturation level are used to quantify the capability of the VI. The characterization and analysis are essential base for researchers and designers to integrate the VI in converters and help them in choosing suitable VI configurations for their application.

Chapter 5 provides a step by step design procedure of a VI considering the nature and requirements of a three-wheel recreational electric vehicle.

Chapter 6 presents systematic approach for selecting suitable magnetic core materials and a comprehensive review of magnetic core materials for powertrain DC-DC converters as a supplement to the design of VI.

Chapter 7 provides the dynamic modelling of VI considering the target application and the development of an integrated control loop and a simple strategy to enable continuous regulation of magnetic properties of the VI and analysis of the performance enhancements due to its introduction to powertrain DC-DC converters.

Finally, the main concluding remarks and possible future trends of this thesis work are provided in the last chapter.

Chapter 2 State-of-the-Art

2.1 DC-DC Converters for EV Application

The generic schematic of the state-of-the-art architecture of EV with its vital power electronic converters, ESSs and an electrical motor is revealed in Figure 2.1. The role of bidirectional DC-DC converter is very significant, especially in terms better utilization of energy sources, power management, dynamic performance, flexibility, system optimization and reduction of weight and cost [18]. Furthermore, these converters enable the hybridization of energy sources. Thereby enhancing the lifetime of batteries, efficiency and reliability and cost reduction of energy storage systems. Besides stepping up the energy storage systems voltage to a higher dc-link voltage, they are used to decouple the battery voltage variations and enable the reduction of the oversizing of the electric motor [19].

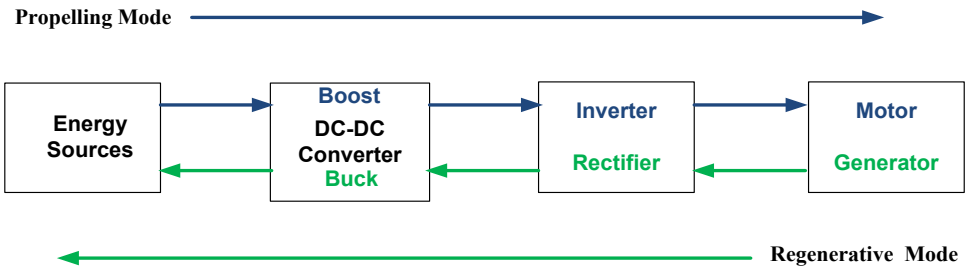

Figure 2.1: Schematic Diagram of EV System Components

DC-DC converters enable electrical drives to make full use of their power sources, increase their power density and provide bidirectional power flow capability. In the forward power flow mode, the voltage from the energy storage systems is stepped up by the DC-DC Converter to the dc-link voltage level and a three-phase inverter change the stepped-up voltage into three-phase voltage to drive the motor and create the required torque. On the other hand, when, the electric motor works as a generator, the regenerated energy flows backwards to recharge the ESSs and the inverter operates as a rectifier and the bidirectional converter works as buck converter to charge the ESSs [11]. These converters should be smaller size, lighter in weight, and have lower cost and higher performance. This is particularly important in transportation electrification due to stringent space limitations. Nonetheless, downsizing of high power DC-DC converters and improving their

performance efficiency is challenging [20], due to the presence of bulky and heavy passive components.

Sometimes, the battery packs can be directly connected to the dc-link in parallel with the dc-link capacitor [21]. If the ratio the dc-link to the battery voltage is much higher than the battery pack voltage, a number of battery modules/sub-packs are connected in series. This requires more space, increases the cost, deteriorate the reliability, adds additional critical failure points, complexity to the battery equalization circuitry, and require more maintenance [22]. Furthermore, if the battery packs are connected directly to the dc-link, the battery lifetime will be affected due to the current variations [23]. Lower inverter input voltages will affect the efficiency and the cost due to higher currents. Currently, the commonly used motor drive voltage tends to be significantly higher than the typical battery voltage, generally 500-700V. At these voltages, the conductors in the motors can be smaller, allowing for higher density and higher power rating motor drive components. Therefore, there is an immense need of high-step up and higher efficiency power electronic converters for higher power applications in EVs [24].

With a particular emphasis of improving the efficiency, voltage gain, power handling capability, size, volume and power density, several step-up converters with different configurations and topologies are presented in [25], [26], [27]. Reference [26], identified the most commonly used step-up topologies and noted the fundamental challenges of several topologies. Accordingly, categorized them based on their circuit configurations and their applications. The comprehensive comparison of bidirectional converter topologies and their control schemes is provided in [27].

For EV applications, the DC-DC converters are needed to have a high efficiency, low cost, compact design and smaller input current and output voltage ripples [28]. Furthermore, they are required to have bidirectional power flow capability and they can be classified as non-isolated and isolated ones [29], [27]. The first group of converters are suitable in applications where galvanic isolation is not important and they have reduced size, weight and volume, better efficiency and less components count [30], [31]. Such types of converters are suitable for applications where smaller size and weight are important requirements such as automotive applications. Isolated boost converters provide high boost ratio and they are suitable for interfacing energy storage systems

such as batteries, fuel cells and supercapacitor. Besides, isolation and safety, they have salient features in current regulation, adaptable step up ratio adjustment and transfer energy over wider range of voltage [26], [32]. These converters are suitable for on-board applications [33]. Nonetheless, these converters are composed of high frequency isolating transformer and more passive components that add up to the components count and affect the efficacy of the converter for EV applications. The use of isolated DC-DC converters reduces the power density and increases the cost and complexity. Due to all the aforementioned facts, for applications such as traction, where efficiency, size, weight and low cost are stringent requirements, the non-isolated converters are more attractive and preferable [23].

The non-isolated converters can also be classified into conventional, multilevel, interleaved, switched capacitor, and derived converters. Some of the commonly used conventional, derived and multilevel converters are shown in Figure 2.2. The class C DC-DC Chopper (half-bridge) shown in Figure 2.2 (a) is the simplest and low cost converter that can be used for stepping up voltage for EV applications without isolation [34], [35]. However, it needs to operate at higher duty cycle for high step up voltage and this leads to more ripple and larger passive components. This also introduces practical implementation challenges due to reverse recovery issues and massive losses. Furthermore, operating at higher duty cycles causes high switching stress resulting in more losses and larger heat sinks [26].

Furthermore, new converter topologies derived from cascading of the conventional converters can be obtained. Cascading the conventional converters can increase the flexibility of voltage gain variation and can help in reducing the input current ripples. Unfortunately, the higher number of passive components, active switches and diodes complicate the system control, deteriorate the efficiency and robustness of the system [26], [36]. Hence, cascading is not suitable approach for high power density and higher efficiency converters for EV.

Multilevel topology of converters offers high step up voltage for high power applications. The rating of the switching devices is greatly reduced resulting in increased efficiency and fault tolerance capability. Nonetheless, this family of converters require voltage balancing circuits which complicate and increase the size of the converters. Furthermore, these types of converters require complicated control structures [37]. They are characterized by low voltage stress, smaller passive

components, reduced losses and EMI, and they are applicable for high power applications [38]. Nonetheless the voltage unbalance between different levels and higher number of output capacitors increase the components count and complicate the control circuitry [36], [39].

In the pursuit of increasing the power level of power electronics converters at higher efficiency, performance and power density, paralleling of devices has been considered as one of the common solutions for increasing the power levels, but this solution fails to correct the input and output ripples. Furthermore, it requires current balancing circuits which complicate the system and affect the overall size of the converter [26], [40].

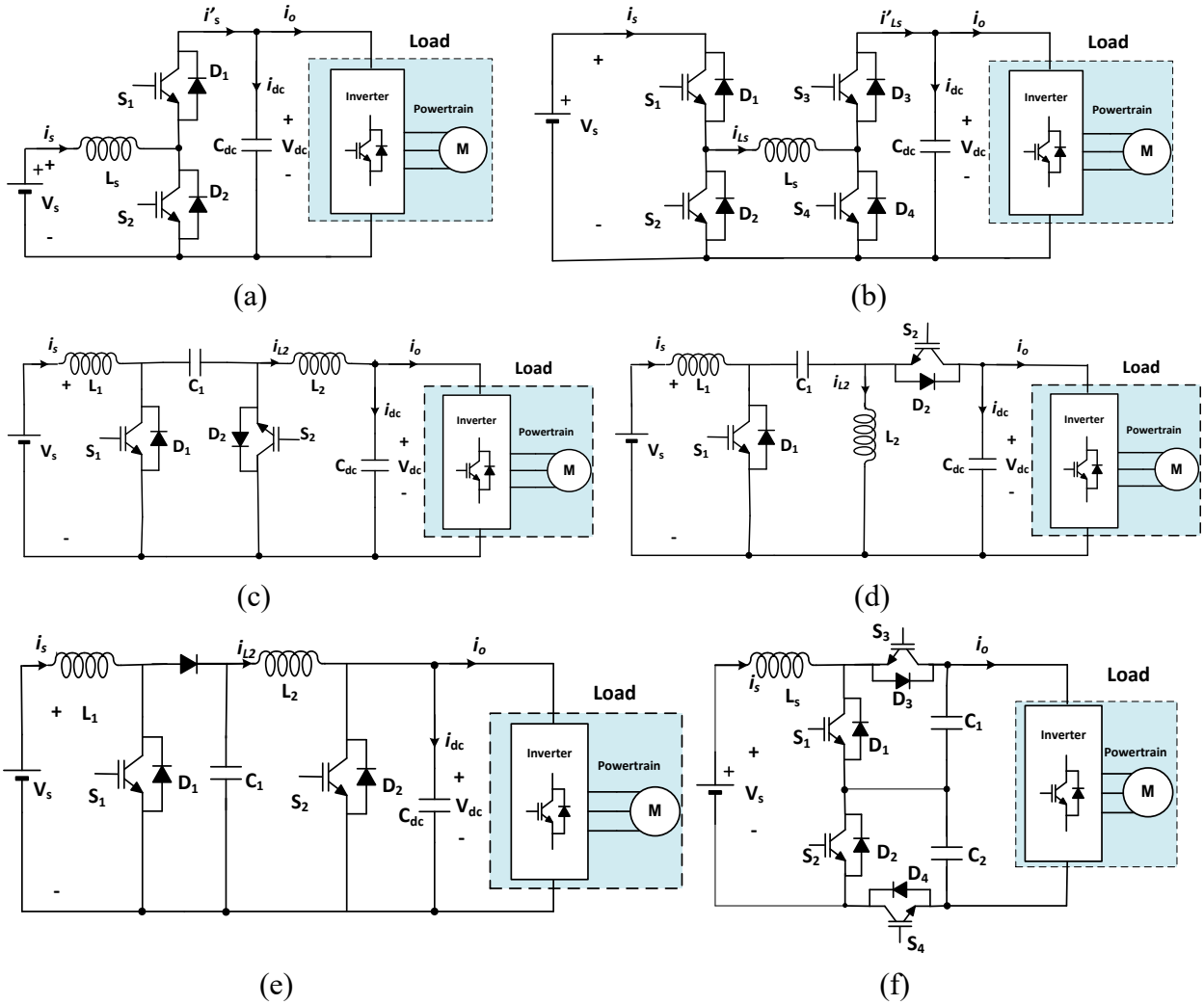

Figure 2.2 DC-DC Converters for EV (a) Half-bridge (b) Full-bridge (c) Cuk (d) SEPIC (e) Cascaded boost (f) Three Level

Interleaving multiple cells to increase the power levels and simultaneously splitting the overall system into smaller sub systems with relatively low power rating is one technique for stepping up voltage without the need of extreme duty cycles. This technique provides promising significance in reducing device stress, reducing filter size, current ripple, harmonic reduction, reducing the size of output filter capacitors, enhancing power density, improving performance efficiency and better reliability [28], [41],[42], [43]. Furthermore, the interleaved converter can be used to improve the efficiency by partial operation of the individual phases at light loads and improve the reliability under faulty condition of one of the phases [28]. Subsequently, several interleaved based converters are proposed in literature and some of them are provided in Figure 2.3.

Increasing the number of phases in interleaving greatly reduces the filter size (volume by $(1/N^2)$ times, device stresses and enhance the dynamic response [41]. The reduction of current ripple content in the total current relieves the current stress on both high and low side capacitors. Furthermore, The power inductors in interleaved converters can be integrated in a single core with specific coupling methods in order to reduce the size of the magnetic core and reducing the switching losses resulting in improved efficiency and easier thermal management [44], [45]. The performance and power density of interleaved converters can further be enhanced by coupled inductors where all the inductors are wound in the same magnetic core. Furthermore, by the use of inverse coupling, the circulating currents can be suppressed and the transient performance can also be enhanced [46]. The salient features of these types of converters makes them attractive for the automotive applications where smaller space and lighter weight are stringent requirements. However, there is a considerable leakage inductance due to the non-ideal coupling of the coupled inductors that results in high voltage spikes, parasitic ringing and losses in the converter, which make the converter performance degraded. Hence, they require additional circuitry and have complex control and driving circuitry to compensate these effects [47]. Besides the increase of cost and components count, these converters require multiple current sensors and are prone to unbalance of currents [30].

Double dual boost converter [48], [49], and multi-device interleaved boost converters [50] are also proposed. Though, these topologies can be used in cancelling the ripple currents and reducing the size of input and output filters, the higher number of components count increases the cost, control complexity and reduces the reliability.

Floating interleaved power converters are proposed in [51]. These converters provide notable significance in controlling the current ripple and improving the power density of converters for ESSs such as batteries and fuel cells. Nevertheless, the higher number of active components leads to higher cost and control complexity.

To increase the voltage gain limit of interleaved boost converters, voltage doubler is introduced in [52]. A unity turn ratio autotransformer is used for equally sharing the currents between the switches. This configuration reduces the current ripple and voltage stress of the switches. Nevertheless, the autotransformer increases the size and cost. A two phase interleaved charge pump topology with high voltage conversion capability, higher efficiency and simpler control strategy is presented in [53]. Unlike the classical interleaved converters, this topology uses two switches in the same path and have additional charge pump capacitor.

An impedance (Z) source inverter which incorporates the functionalities of both DC-DC converters and inverter is used to connect the energy storage systems (ESS) to the motor [54]. This configuration has less number of switching components, at the expense of bulky passive components [37].

To recap, the state-of-the-art DC-DC converters for high power EV applications several topologies are presented in Figure 2.2 and Figure 2.3, and a summary of their comparison considering their merits and demerits, voltage ratio, switching devices stress and number of active and passive components is provided in Table 2.1.

Several topologies are presented in literature. To improve the performance and reduce the size of components in the topologies, new trends in topologies, control, switching devices such as introducing wide bandgap (WBG) switching devices and improvements in passive components are needed. The comparison of the state-of-the-art converter topologies is provided in order to choose suitable candidates. WBG switching devices provide an opportunity for scaling down passive components and reducing switching losses. Nonetheless, as they are in their nascent stage, still a lot of work is needed. At the state of current technologies, the use of VI can play a significant role in reducing the size of magnetic components. It is important to note that with advancements in the WBG topologies, the VI can be integrated in WBG based converters. The combination of the VI

and WBG switching devices can provide an opportunity for further reducing the size and improving the performance of power electronic converters. The state-of-the-art review of each of them is presented in the remaining part of this section.

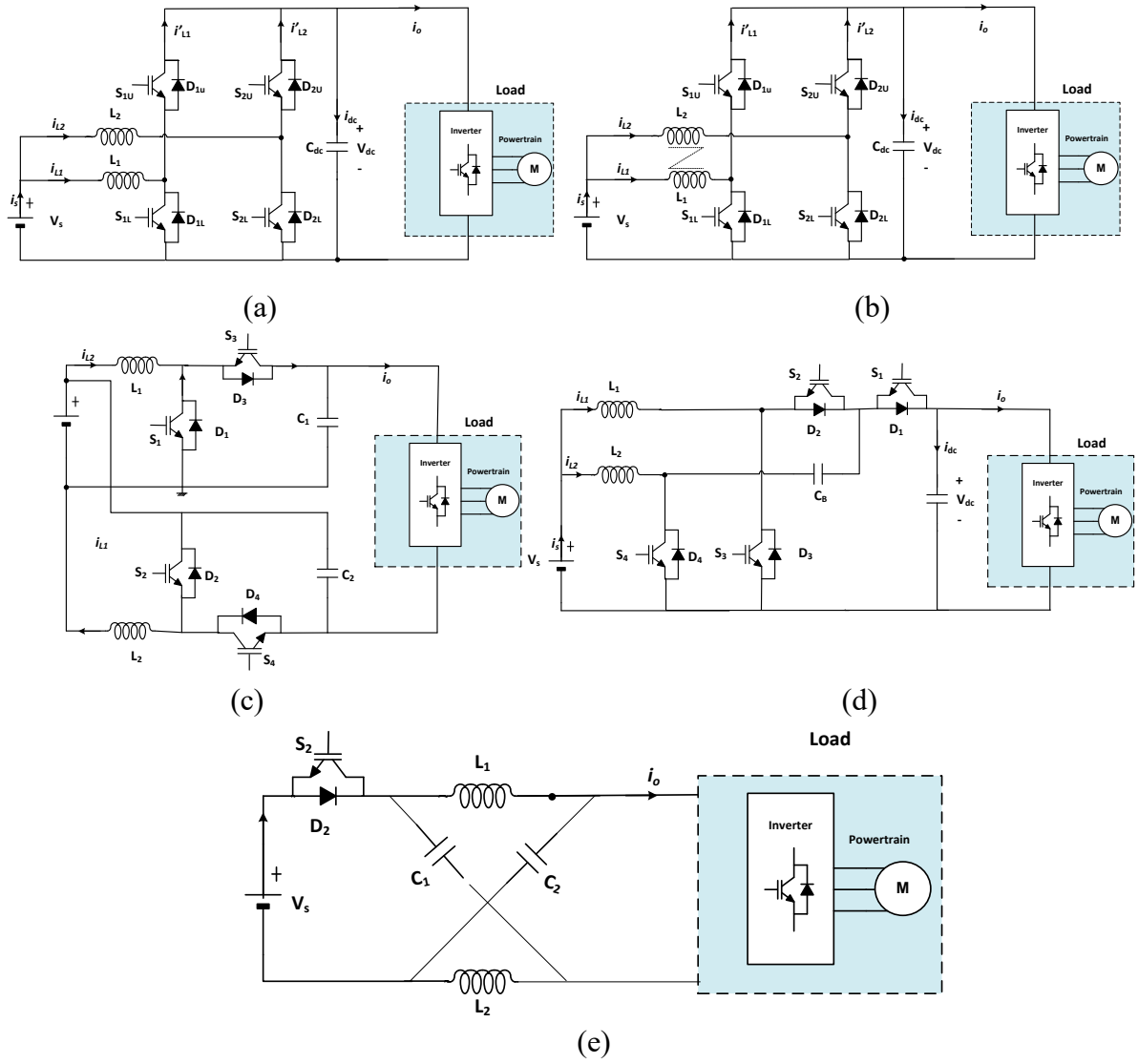

Figure 2.3 Interleaved Converters and Z-source Converter (a) Two-phase interleaved (b) Coupled inductor two-phase interleaved (c) Floating Interleaved (d) Interleaved converter with charge pump (e) Z-Source Converter

Table 2.1: Comparison of Step up DC-DC Converters

Topology	Conversion Ratio ($M(D) = \frac{Vo}{Vs}$)	Switching Devices	Magnetic Components	Output Capacitor	Switches Voltage Stress	Remarks
Half-bride	$\frac{1}{1-D}$	2	1	1	V_{dc}	Simple topology, low cost and components count Limited range of voltage and output capacitor to filter the output current
Full bridge	$\frac{1}{1-D}$	4	1	1	$V_{dc} + V_s$	Can operate in four quadrant and is flexible topology Less switching stress and better reliability Higher number of switches which complicates its control and increases its size
Cuk	$\frac{D}{1-D}$	2	2	2	$V_{dc} + V_s$	Provides filtered input and output currents Higher number of components Not easy to stabilize
SEPIC	$\frac{D}{1-D}$	2	2	2	$V_{dc} + V_s$	Provides filtered input and output currents Higher number of components Not easy to stabilize
Cascaded	$\frac{1}{1-D_1}.\frac{1}{1-D_2}$	4	2	2	V_{dc}	Wider conversion ratio, reduced stress on the first two switches and reduced current ripples. Its robustness is compromised due to higher number of passive components and its reduced efficiency [36]. The control scheme is also complex. It could be costly
Three level	$\frac{2}{1-D}$	4	1	2	$\frac{V_{dc}}{2}$	Enable wide range of conversion, has continuous input current, semiconductor switches are rated at half of the output voltage and it can be built in a modular way [38]. It has higher switching components and two output capacitors, which makes it larger size. The output diode reverse recovery problem is a concern
Two phases interleaved	$\frac{1}{1-D}$	4	2	1	V_{dc}	The power inductors are rated at half of the input current, smaller and lighter weight components, this gives more flexibility in component selection. High power density Can provide redundancy with improvements in reliability, expandability, availability and maintainability [55]. The ripple current in each arm can be higher which requires attention. More active and passive components and control complexity.
Coupled inductor two phase interleaved	$\frac{1}{1-D}$	4	2	1	V_{dc}	Coupling inductors interleaving improves efficiency, reliability and reduces the size of magnetic components Non-ideal coupling may result in high voltage spikes and losses, requiring an additional circuitry for compensation. For high power applications, the coupled inductors are difficult to manufacture and the cost will be significantly increased [56].
Floating interleaved	$\frac{1+D}{1-D}$	4	2	2	$\frac{V_{dc}}{1+D}$	Smaller inductors as they are rated at half of the input current, suitable for high power applications and it has higher voltage gain. Nonetheless, it has higher current stress and two capacitors at the output [31]. Interleaving should be pair in order to balance the floating bus [57]. It also needs isolated gate drivers, has lower efficiency and floating load connection. furthermore, these converters have drawbacks including parts count, circuit complexity, and control complexity
Interleaved with charge pump	$\frac{2}{1-D}$	4	2	2	$\frac{V_{dc}}{2}$, (S_1, S_3, S_4) V_{dc} (S_2)	Doubles the output voltage in comparison the simple boost, less conduction losses, reduced voltage stress in switches but it has higher number of passive components [53].
Z-source	$\frac{1}{1-2D}$	1	2	2	$\frac{V_{dc}}{1-2D}$	It uses single conversation stage hence saves components count and cost Larger size, and higher component stress, complex control ,limited boost ratio, less reliability [58], [42].

2.2 Wide Bandgap Switching Semiconductor Devices

The switching frequency is one of the key parameters in the design and selection of the power electronics converters. It significantly impacts the inductor current ripple, energy source current ripple, input capacitor current ripple and the losses. Hence, an optimized switching frequency is needed to achieve a better trade-off between converter size, cost, and system efficiency [59]. The most commonly available automotive power converters use Silicon (Si) based semiconductor switches. These types of switching devices are constrained to operate at a lower frequency (few kHz), this is mainly due to high switching losses which compromise the efficiency of power electronic converters [60]. Furthermore, lower switching frequencies lead to larger passive components (power inductors and capacitors), which limits their application for high power applications greater than 100 kW range [61]. Consequently, the size of the passive components particularly the power inductor and capacitor is large in such types of converters [62]. This in turn increases the overall size of the power electronic converters and limits the space for ESSs in electrified vehicles, constraining the autonomy.

Wide bandgap switching semiconductor devices such as Gallium Nitride (GaN) and Silicon Carbide (SiC) enable high frequency switching. High frequency switching enables in reducing the energy requirements of power inductors, leading to the scaling down the size and weight of power inductors leading to the reduction of power electronic converters [63]. Subsequently, they are promising and they are expected to be the backbone for future power electronics converters for traction application [64]. These switching devices have lower losses and they can have faster switching speed, low switching and conduction losses, high operating temperature (well above 200^{o}C possible for SiC vs 150^{o}C in case of Si [65]) and small packaging size. Furthermore, these devices have higher frequency of operation, leading to faster switching, smaller components and less thermal management challenges in comparison to the conventional Silicon based semiconductor devices.

The introduction of these devices to the traction power conversion can be rewarding in scaling down the size of passive components. Nonetheless, due to fast switching transition, parasitic inductance, and low on-state resistance, converters with such types of switching devices are prone to overshoot and oscillations which lead to losses and EMI challenges [66], [67]. Furthermore, losses due to skin and proximity effects, and fringing losses are difficult to reduce requiring specialized design of passive components for high frequency operation [68]. These technologies are in their nascent stage with limited production and limited power levels. As a result, their cost is still prohibitive compared to Si-based semiconductor switches [69]. Even though

they have a promising potential in the future of automotive power electronic converters, there is still a long way to go to address the aforementioned issues that impede the design and implementation of these devices [70].

2.3 Variable Inductor Topologies and Applications

2.3.1 Background

The VI is a magnetic device, which is composed of two groups of windings. One group of windings make the main winding of the VI and the other windings make up the auxiliary winding, which is used to control the effective inductance of the main winding with a very small controlled current. Due to its control flexibility, it is suitable for applications with a wide range of load variations [71].

Moving cores, moving air gap, tapped inductors, switched decade boxes, gyrator circuitry, electromagnet and permanent magnet biasing are the common ways of realizing the VI [15], [16], [72]. The mechanical servo system requirement of moving cores and air gap makes them very demanding and inefficient. Similarly, the switched decade boxes fail to provide precise regulation. The use of permanent magnet biasing also offers considerable impact in improving the current handling capability and saturation control of inductors, but it has limited flexibility and controllability. The gyrator circuitry is also an emulation of inductance. Nonetheless, the saturable core reactor provides better flexibility, higher accuracy as it can be easily controlled with a small electrical current [15]. The use of electro-permanent magnets biasing is another way of increasing the power density of inductors by regulating the magnetic properties of the core material. Nonetheless, such type of inductor is composed of electromagnet and permanent magnet which makes them intricate to design and control. The saturable reactor is deliberately saturated with a small dc-current to drop the inductance of power inductor drastically. Unlike, this device, the VI can be used to either increase or decrease the inductance of power inductors as per the user requirements.

The comparison of different techniques for VIs implementation and the fundamental mathematical equations which characterize a VI are also provided in [15]. In [73] a method of predicting the inductance of a coil with change of an applied DC current is proposed for optimization of the power inductor in power conversion applications. The 3D finite element analysis model of VI is studied in [74] and used to model distribution of flux density and determine the region of saturation. The detailed modelling and behavioral model of VI for magnetically controlled electronic ballasts with E core magnetic material is presented in [75]. A detailed review of VI, its applications and configurations is provided in [76]. Nonetheless, the detailed

characterization of the VI to integrate it to power electronic converters for traction applications still requires further investigation. Furthermore, the systematic design of the VI taking into consideration the nature of traction applications is not yet addressed. Part of this thesis is focused on these two important aspects that are essential for the integration of the VI in power electronic converters to enhance their performance and reduce their size.

2.3.2 Topologies

Several patents and research articles present different VI topologies. Some of them are presented in Figure 2.4. The parameters with *m* subscript are for the main winding and those with *b* subscript are for the auxiliary winding. The simplest topology is the one that is shown in Figure 2.4 (a). It consists of the main winding and the control winding in the same magnetic core. This configuration provides a precise control of the flux in the core; nonetheless, as both windings are strongly coupled to each other, there is might be a huge voltage in the auxiliary winding due to the main winding currents variation, which compromises the safety of the auxiliary winding circuit. In Figure 2.4 (b) and (c) two double E-cores are shown, in the first one main winding is divided into two equal parts and placed in the side limbs of the core. The main winding coils are connected in series to each other and the control winding is placed at the central arm. In this topology, there is still a voltage induced in the auxiliary winding due to the currents in the main winding. However, in the later topology, the main winding is placed in the central arm and the control windings are placed at the side limbs. Such configuration reduces the auxiliary winding voltage due to the main winding currents. Nonetheless, in both configurations both windings are coupled to each other.

Another way of cancelling the effect of mutual flux coupling in VI is to use two separate rectangular magnetic cores as revealed in Figure 2.4 (d), where the main windings are connected in series and the control windings are connected in series but with opposite flux linkage to each other. The opposing series connection of the control windings make the net voltage across this winding nil.

In Figure 2.4 (e), the main winding is placed in the center of two gapped E-cores and the control winding is placed in the center leg of an additional E-core. In this configuration, the mutual coupling and voltage induced in the auxiliary winding is reduced. The VI realized in two toroidal cores where the main and the control windings are split in two toroidal cores and connected in series as shown in Figure 2.4 (f) [77]. In this topology, the control windings are connected in series and they are wound in such a way that there is no coupling between them, hence there is opposing flux from each winding resulting in a nil voltage reflection and no coupling between the two windings.

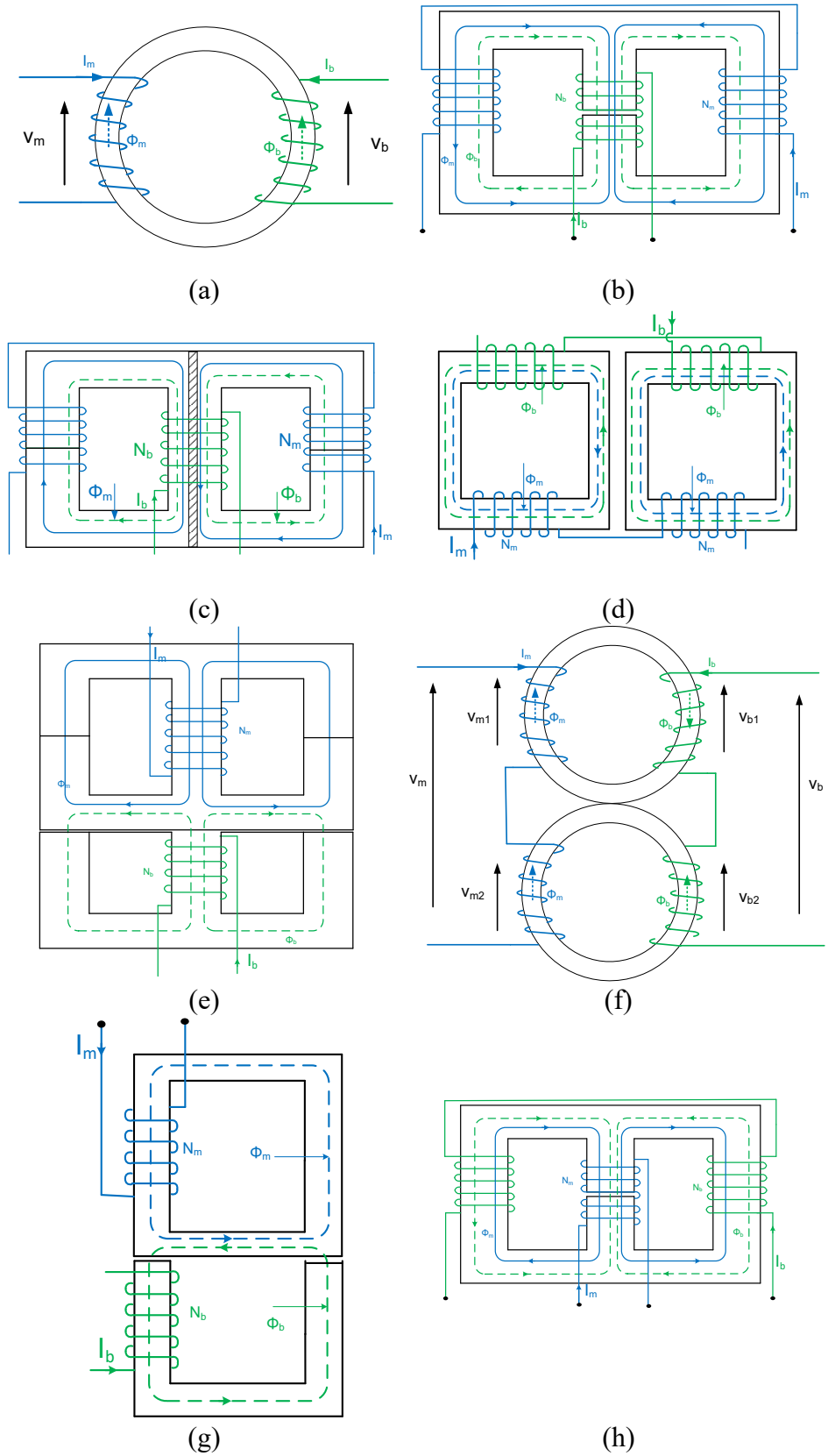

Figure 2.4: Different VI topologies

A combination of a rectangular core and U core is shown in Figure 2.4 (g). This configuration is also prone to the effects of voltage induced in the auxiliary winding. In Figure 2.4 (h), a small air gap is placed in the central arm in order to reduce the losses and unwanted hysteresis in the inductor.

In all configurations, the addition of the control winding adds complexity to the system and have some additional costs, but its significant role in regulating the effective inductance, reducing the losses and the current ripple leads to smaller volume cores, which overcomes the drawback of its addition. Subsequently, there is a need to a simpler and cost effective VI topology with a simple control and strategy to integrate it to power electronic converters without sacrificing the performance of the converter. This aspect is dealt in part of this thesis.

2.3.3 Applications

The practical use of these devices stems from the beginning of the 20th Century. Initially the concept of VI was introduced in the form of magnetic amplifiers, where they were used in long-range radio communication. In the end of the World War II, this device was popularly used in German military equipment in range of applications such as servo controllers in planes, voltage regulators in the V-1 bombs and German naval fire control [76], [78]. As a result, its popularity both in military and industrial control application emerged and has been used in effective stabilization of guns, sonar and radar. Furthermore, it is used in electric power system networks as voltage and frequency regulator [76]. With time, the principle of these devices evolved to VI. The variable inductor is a very powerful and promising device that can have considerable practical applications. This device has been effectively used in power control of resonant filters, in lamp driver applications, in LED lamp drivers, inductive power transfer [79], PV systems [80], [81], electric lighting systems [82], [83], and VAR compensation in electrical power system networks. Furthermore, it has worth recording applications in resonant AC and DC-DC converters [84], [85], power factor correction [83], power flow control and fault current limiting [86], harmonic control and voltage regulations [71].

2.4 Control and Strategy

The most widely used control approaches for DC-DC converter are the average current and the peak current control methods [87]. The first one uses the information of the average current of in order to provide precise reference tracking. This provides good stability, noise immunity and fast response and correct perturbations and disturbances. However, the maximum achievable bandwidth of this concept is limited due to the inevitable closed loop delays [87]. The peak current control is also another simple and low-cost solution.

However, in its conventional implementation, its transient response is severely affected by the need for slope compensation, which is required for stability in a wide operating region [87]. Furthermore, hysteretic controller is also presented in literature [88]. This control method provides excellent large signal properties and its implementation is simple. Nonetheless it suffers from switching frequency jittering [87]. Sliding mode (SM) controller based non-linear controller are deemed to be promising for such DC-DC converters due to their improved robustness in providing transient responses over a wide range of operating conditions [89]. Furthermore, it is robust even against the plant parametric variation and can compensate the modelling approximations [90]. PWM based sliding mode current control are suitable for non-minimum phase converters [91], [92]. However, their conceptual complexity makes them impractical [89]. This is mainly due to the unavailability of SM controllers in integrated circuits (IC) forms for power electronics applications. Furthermore, this control method introduces steady state errors which makes it not suitable for applications which require precise control [91].

PID or PI is a widely used and industry standard controller in power electronic converters. However, their tuning is demanding task due to the non-linear transfer functions. Furthermore, controller parameters are affected by parameter variations, load disturbances and speed variations [93]. This case is more demanding in case of EV converters due to the wide range of load variations and uncertainty of driving situations. These problems can be addressed by fuzzy logic controllers, which does not require mathematical models but are based on linguistic rules that can be obtained from the human experience. Fuzzy logic-based controllers are commonly used, and they are based on the human experience and fuzzy control rules. These controllers are cheaper, robust, efficient, reliable and customizable. Nonetheless, they require more data, an extensive human expertise and regular update of the rules is needed. PI controllers provide better performance in steady state, but fuzzy logic controller provides better performance during transient performances. Hybrid of PI and Fuzzy are also proposed in literature to exploit the complementarity of the two types of controllers [94].

In this work, the affine parameterization (Q-parameterization or Youla parameterization) design is proposed to build stable feedback controller to regulate the control parameters. Unlike the classical control design methods, this method starts with the nominal closed loop transfer function of desired closed loop performances. Affine parameterization simplifies model-based controller designs [95]. The controller parameters are directly derived from desired closed-loop models. Furthermore, this method being internally stable provides faster dynamic response to adapt the rapid dynamic load variations [96]. This method provides an insight into control system design and it renders the closed loop sensitivity functions in a design

variable. Furthermore, it provides a simpler description of all stabilizing controllers for both the open loop stable and unstable linear plants. It gives valuable insight into the control problem and opens the door to various optimization based strategies for design [97]. Affine parameterization makes the control parameter tuning straight forward and more flexible and assure the control stability [96].

For controlling the VI, both the auxiliary biasing circuit [9], voltage controlled current source based on linear regulation [98], and forward converter [99] are reported in literature. In references [16], [100], a separate DC supply with variable resistors have been used. However, this does not provide a precise control of current and it is not efficient. Similarly, the forward converter could provide better flexibility and it can be integrated to the application circuit but as it requires isolation, it has larger size, less efficiency and higher number of components. To address these issues, a digitally controlled, simple and low-power buck converter that can be integrated to DC-DC converters for regulated adjustment of the auxiliary current is implemented.

2.5 Summary

This chapter presents the state-of-the-art review in the major research areas which provide an opportunity for improving the performance and reducing the size of DC-DC converters for electrified vehicles. A focus is given to the DC-DC converter topologies, WBG devices, variable inductors topologies and their application and control. The comparison of several DC-DC converters and VI topologies is provided in order to explore the potential candidates and select a suitable converter topology. Several approaches have been proposed in literature and their merits and drawbacks have been identified. Furthermore, brief review of the merits and challenges of WBG devices are illustrated. The advancement of WBG provides a significant opportunity in improving the performance and miniaturization of automotive converters, yet their challenges needs to be addressed. It is important to note that, not only the size and weight but also the performance of power electronic converters in EVs dominantly influenced by the bulky and saturation limited power inductors. Hence, reducing their size and weight, and controlling their saturation behavior provides an opportunity in reducing the size of power electronic converters but it is challenging. To this end, this thesis seeks a solution for scaling down the size of magnetic components by controlling the saturation characteristics of magnetic core materials. The magnetic saturation control provides a salient merit in core reduction, converter operation and performance enhancement. Nonetheless, it introduces, characterization, modelling, design and suitable materials selection, control and the need of strategy challenges. The focus of this thesis is based on these issues in order to integrate the VI in new and existing converter topologies for electrified vehicles.

Chapter 3 Variable Inductor Based Bidirectional DC–DC Converter for Electric Vehicles

Original Title: Variable Inductor Based Bidirectional DC-DC Converter for Electric Vehicles

Authors and affiliation: **Mebrahtom Woldelibanos Beraki**: PhD Student, Université de Sherbrooke, Faculté de génie, Département de génie électrique et de génie informatique

João P. Trovão : Professor, Université de Sherbrooke, Faculté de génie, Département de génie électrique et de génie informatique

Marina S. Perdigão: Professor, Instituto de Telecomunicações and Polytechnic Institute of Coimbra, 3030-290 Coimbra, Portugal

Maxime R. Dubois: Professor, Université de Sherbrooke, Faculté de génie, Département de génie électrique et de génie informatique

Date of Acceptance: May 10, 2017

State of acceptance: Published

Reference: IEEE Transactions on Vehicular Technology, DOI:10.1109/TVT.2017.2710262

Summary

Content: This article presents the viability of VI for building DC-DC converters for applications with a wide range of load variations such as EVs. The conventional power inductor in DC-DC converter is replaced by VI in order to have better ripple control, enhanced current handling capability and adaptive control of the saturation level of a power inductor. Experimental approach is used to study the potential significance of the VI for converters with wide range of load variations. More emphasis is given to the details of the device and its application for ripple control and enhancing the current handling capability of an inductor and the control of the overall system.

Results: The validity of the proposed VI, the biasing circuit and the improved DC-DC converter are verified through experimental studies. The presented results reveal the importance of VI in enhancing the current handling capability of magnetic core materials and controlling current ripples.

Contribution to the thesis: Magnetic components are bulky and dominant components in DC-DC converters. This article presents the use of the VI for scaling down the size of such components and enhance the performance by controlling the magnetic properties of magnetic core materials. The proof of concept small scale prototype developed in this study and the results are used as a benchmark to perform detailed studies such as the characterization, design and selection, modeling and control of the VI in order to exploit its merits for large scale electrified vehicles DC-DC converters.

Abstract

This paper presents the feasibility study of variable inductor (VI) based bidirectional DC-DC converter for applications with wide range of load variations such as electric vehicles (EVs). An additional winding is introduced to the conventional power inductor to inject a control current for adjusting the permeability of magnetic cores. This has significant merits in controlling the current ripple and enhancing the current handling capability of power inductors thereby reducing the size of magnetic components and improving the performance. For current values, twice and three times the rated current, the current ripple is reduced by 40.90 % and 36.10 % respectively. Nonetheless, this device requires a precisely controlled dc-current. As such, a small current controlled, low-power and low-cost buck converter is built to power up the auxiliary winding. To improve the reliability and robustness of the VI, an integrated closed loop control that enables the control of the main converter and the auxiliary converter is also implemented and tested in real time to test the viability of the VI.

Keywords

Bidirectional DC-DC converter, electric vehicle, magnetic core, ripple control, traction, variable inductor

3.1 Introduction

In traction systems, energy sources should be connected to the motor drive by efficient and suitable power electronics converters. These converters are vital in adapting the voltage levels, managing the power flow and provide better performances [101], [102], [103]. Their sizing, selection and design is very critical, since they are required to have smaller size, higher efficiency, higher power density and enhanced overall performance [104]. The power inductor and the dc-link capacitor are key components that dominate the size and dynamic performance of power electronic converters [105]. Due to wide range of load variations in traction applications, the selection of these components, particularly the power inductor requires a meticulous attention. This is mainly due to the core material limitations, losses and its impact on the overall performance[16],[106],[107]. Conventionally, this component is selected to meet the ripple specifications under all operating conditions. Nonetheless, in applications where there are wide range of dynamic load variations and with multiple kind of energy storage systems, such as EVs, the transient currents during acceleration and regenerative braking may reach very high values. Selecting power inductors to meet the high transient currents will lead to bulky and heavy power inductors. This increase the size and weight of power electronic converters. Larger power electronic converters, limit the space for energy sources, thereby restricting the autonomy of EVs. Therefore, it is vital to scale down the size of passive components in order to reduce the overall size of these converters. This has motivated the adoption of numerous studies [104], [6], [50]. Several methods such as the development of new materials, winding configurations, assembly techniques, increasing the switching frequency, interleaving techniques, the use of coupling inductors and the use of permanent magnets have been proposed and explored in recent literature [6], [7], [108], [109].

Magnetic-based solutions have been presented in recent literature; integrated winding coupled inductors have been used to reduce the size and volume of the magnetic material. However, they have higher switching losses due to close coupling and stray capacitance [109]. Furthermore, interleaving technique has been successfully used to reduce the size of passive components, reducing the input current ripple, improving the efficiency and dynamic performance, reliability and modularity [110]. Nevertheless, it requires higher number of components count and current balancing control which complicate the control circuitry [47].

Power inductors in interleaved converters can be also integrated in a single core with specific coupling methods in order to reduce the size of the magnetic core and improve the performance [44, 45]. However, there is a considerable leakage inductance due to the non-ideal coupling of the coupled inductors which

results in high voltage spikes and parasitic ringing, which require additional circuitry to compensate this effect. The use of permanent magnets to partially cancel the magnetic fluxes in magnetic cores have been also used to enhance the saturation current and reduce the size of power inductors[106]. Even though this solution provides remarkable improvement in doubling the saturation current, its control flexibility is limited.

In this paper, a current controlled magnetic device, the so-called variable inductor (VI) is introduced into a half-bridge bidirectional DC-DC converter (as shown in Figure 3.1) to enhance the inductor flux density capability. By feeding the auxiliary winding with a controlled dc-current in closed loop operation, it is possible to detect high current load demands and regulate the saturation level of the core. For this, a power control layer and an additional converter are designed and implemented. The auxiliary converter used in this study is smaller and has less number of components compared to the H-bridge [108] and forward [111] converters proposed in literature. Besides improving the current handling capability of the power inductor by effectively controlling the reluctance of the magnetic core, the VI will also act as a current ripple regulator. Furthermore, with faster controllers, by forcing the power inductor to saturation, faster transient performances can be obtained [108]. This points out another salient advantage of the VI.

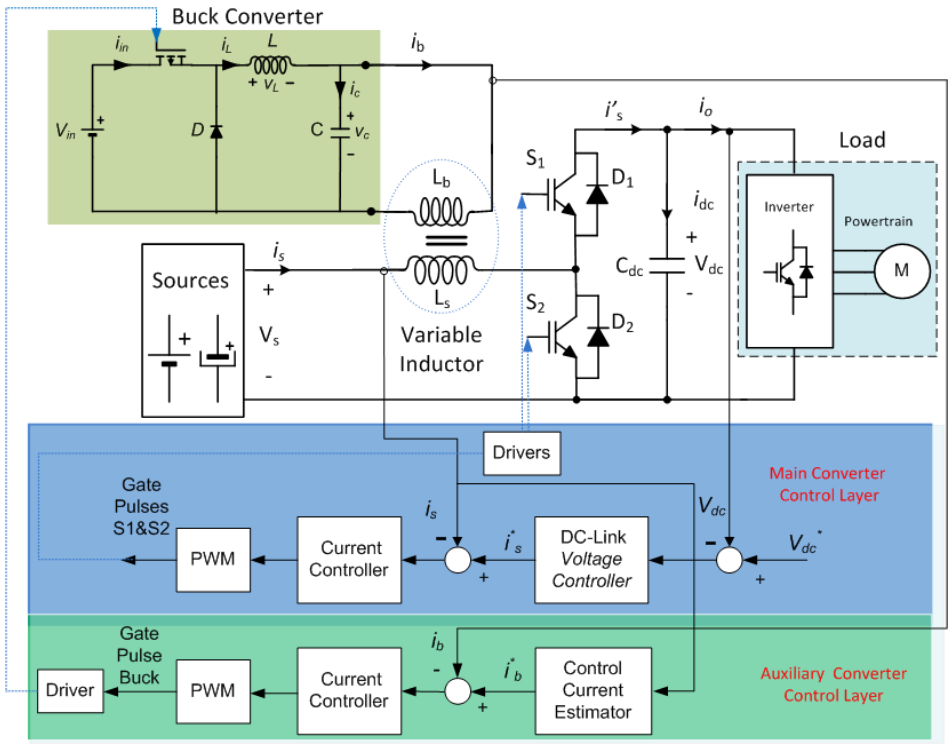

Figure 3.1: Schematic Diagram of VI based bidirectional Converter and its control structure

This paper is organized in five sections. The introduction is presented in section 3.I. Section 3.2 introduces the VI-concept, including its operating principles, its application in ripple control, the selected topology and its configuration. The general overview of the studied system and the design of the controllers for the main and auxiliary converter are provided in section 3.3. Section 3.4 presents the experimental system and the results. Finally, the concluding remarks and future works are presented in section 3.5.

3.2 Variable Inductor Concept

3.2.1 Operating principle and ripple control

A VI is a dc-current controlled, multiple winding inductor realized in various geometries and magnetic cores [112], [113], [114]. It consists of a main winding and an auxiliary winding where the dc-control current is applied to adjust the reluctance level of the core. The controlled current in the auxiliary winding alters the magnetic flux density of the core and adjusts the operating point in the $B-H$ curve. To illustrate the fundamental concepts involved a classical $B-H$ curve is revealed in Figure 3.2.

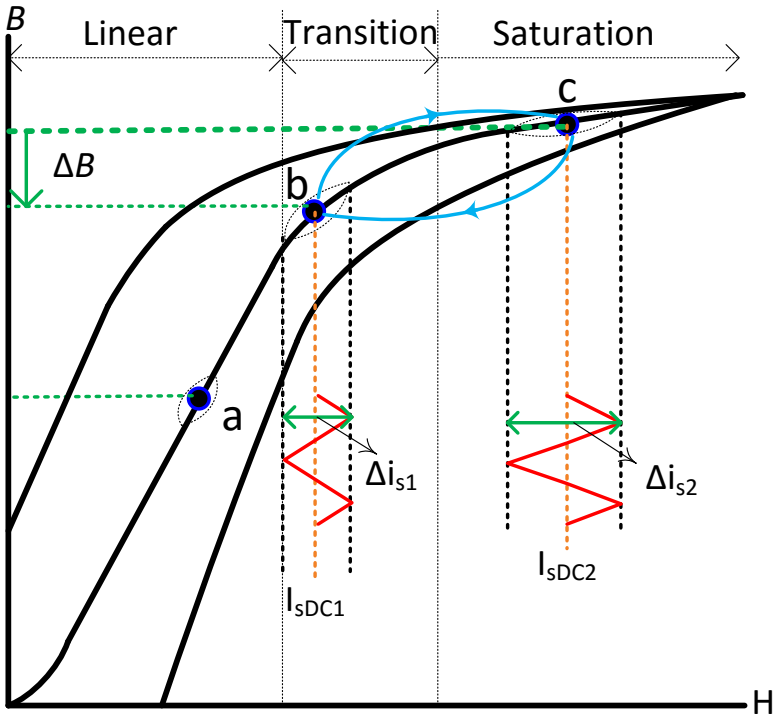

Figure 3.2: B-H Curve for illustrating the operation of VI

In the proposed bidirectional converter, a C-Class chopper, the amount of the inductor current ripple is given by:

$$\Delta i_s = \frac{V_s D_s T_s}{L_s} \tag{3.1}$$

where V_s is the source voltage, D_s is the duty cycle (the ratio of the on-time to the switching period), L_s is the inductance of the power inductor and Δi_s is the current ripple. As shown in (3.1), the amount of current ripple is inversely proportional to the inductance of the power inductor. If the power inductor is operated in the saturation region of the $B - H$ curve, its inductance will fall due to the reduction in the permeability of the material. This will influence the dynamic performance of the converter as well as the expected levels of current ripple and losses.

Referring to Figure 3.2, three different load conditions are considered, a – light load, b – transition load (which corresponds to an average current level (I_{sDC1}), in the power converter) and c – heavy load (corresponding to a higher average current level (I_{sDC2}). In point a, the power inductor operates in the linear region, hence there is no effect on the level of the current ripple, since the value of the inductance remains constant. By pushing the operating point to b and c, the core enters in the transition and saturation regions. Consequently, the inductance of the power inductor will be reduced. As a result, the current ripple will increase. The increase in the current ripple and reduction of the inductance leads to higher rms current leading to higher losses and heating in the power converter and switches.

With a control, current injected into the VI, the operating point c, at heavy-load, can be adjusted. By cancelling part of the main winding flux density, the operating point can be moved down to the transition region from point c to point b as shown by the blue arrow. In fact, resulting in inductance, which is higher than the inductance at point c, maintaining the level of the current ripple at reasonable values. For two operating points b and c, the projected waveforms are to illustrate the effect of the change in inductance with increase of current and its impact in the current ripple. I_{sDC2} is greater than I_{sDC1} consequently, Δi_{s2} is greater than Δi_{s1}. In conclusion, operation in the saturation leads to the higher current ripples and more losses.

3.2.2 VI topology for bidirectional operation

The main challenge for the VI structure is the forced bidirectional operation. It must operate in motoring or regenerative braking modes. Typically, VIs are built with a main and an additional winding, with mandatory decoupling between the two. The main winding corresponds to the power inductor and the auxiliary winding is connected to a current controlled DC-DC converter. This auxiliary converter must be small and a low-power to avoid any significant additional losses to the whole system.

Figure 3.3 depicts the schematic diagram of the studied VI. It is realized by two sets of windings, the main winding and the auxiliary winding wound into two magnetically decoupled magnetic cores. The two windings are wound on two toroidal ferrite cores, each made by stacking of two cores.

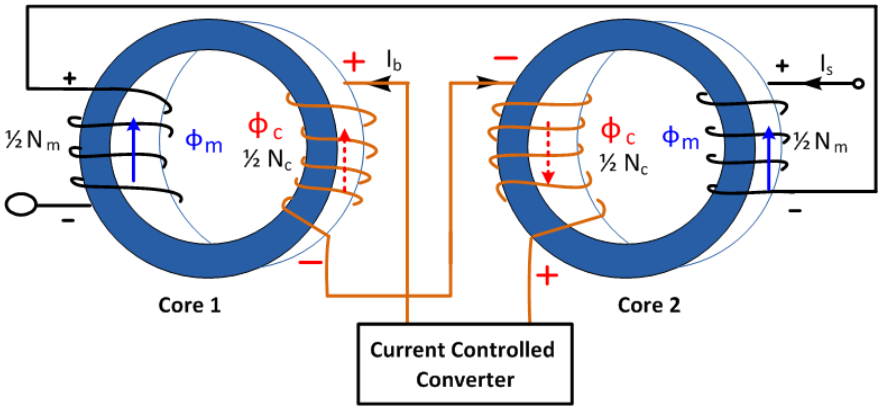

Figure 3.3: Schematic diagram of VI-Prototype with its Control Converter

Both the main winding and auxiliary winding number of turns are equally divided into the two toroidal cores. The main winding in the core 1 and in core 2 are electrically connected in series. Similarly, the auxiliary windings in the two cores are connected in series. However, to cancel the amount of reflected voltages from these windings to the main windings, they are wound in such way that the net induced voltage is nil. This accounts for the required decoupling action.

Figure 3.3 shows the directions of the fluxes: the red arrow represents the flux imposed by the current flowing in the auxiliary winding and the blue one represents the flux imposed by the main winding. In core 1, the magnetic flux from the main winding and the magnetic flux from the auxiliary winding partially cancel each other, whilst in core 2, the two fluxes add up. In core 1, the cancelation of the flux moves the operating point of the core to the linear/transition region while in core 2, the additive flux forces the magnetic core to operate in the saturation region. Nonetheless, this configuration has better saturation regulation and ripple current control in comparison to the same configuration with no control current in the auxiliary winding. Also, as the main windings are electrically connected in series, the total inductance will be the sum of each individual inductances. Therefore, with this approach the effective inductance can be regulated. It has to be noted that the auxiliary winding is idle during the levels of current less than the saturation current of the power inductor. However, for currents greater or equal to the saturation current the control current is injected in order to enable the partial saturation operation of the power inductor. In order to have minimum impact of the auxiliary winding on the overall efficiency of the bidirectional converter, the auxiliary winding number of

turns are made much higher than the main winding number of turns. Besides the gauge of the main winding is about 6.5 times larger than the auxiliary winding wire gauge. The specifications of the studied VI-prototype are detailed in Table 3.1.

Table 3.1: Specifications the VI- prototype

Ferrite core Toroid R 102 × 65.8 × 15.0 (mm) with Epoxy coating	
Core material	N87 from EPOCS
Main winding wire gauge	4.17mm^2
Bias winding gauge	0.65mm^2
Main winding number of turns	28
Auxiliary winding number of turns	360
Total Volume of VI	0.273dm^3

To exploit the merits of the VI in controlling the current ripple and improving the current handling capability of magnetic cores, the auxiliary winding current has to be precisely controlled. To do so, a mathematical relationship between the auxiliary winding and main winding currents is vital. As such, based on the open loop first studies, the relationship between the two currents is obtained using curve fitting. This is further presented in section IV and the curve that relates the auxiliary winding current and the main current is revealed in Figure 3.5.

3.3 System Description

In order to test the proposed solution, a bidirectional converter and a VI were designed and built. The converter was designed in such away; it is capable of sustaining load changes with stable dc-link operation. The VI was designed to easily operate in conditions correspondent to heavy loads, meaning it would saturate relatively fast. The overall schematic diagram of the system used in this study is depicted in Figure 3.1. The bidirectional converter is a C-Class DC chopper, which enables two-way flow of current, consisting of energy sources (such as batteries or supercapacitors), a variable inductor, two active switches (IGBTs) and a dc-link capacitor. The auxiliary converter is a buck-type used for controlling the current of the auxiliary winding to regulate the effective inductance of VI.

The energy storage system supplies power to the traction system, and the bidirectional converter acts as a boost converter to step-up the supply voltage to the dc-link voltage during normal operation and hard acceleration. Whilst, during regenerative braking it behaves as a step-down converter to charge the storage systems. The conventional saturating power inductor is replaced by a dc-current controlled VI. The dc-

current, in the auxiliary winding of the VI is used to regulate the effective inductance of the inductor passive component during higher current demands in hard acceleration and regenerative braking of EV.

Figure 3.1 also shows the required control layers to operate and test this solution. The main converter control layer consists of a dc-link controller and a current controller for the bidirectional DC-DC converter. The dc-link voltage controller is used to keep the dc-link voltage within the limit so that there is stable voltage to be delivered to the load and prevent current ripple propagation to the source. The auxiliary converter control layer consists of a current controller for auxiliary converter and a reference current estimator, which determines the reference current for the auxiliary winding control current.

3.3.1 Main Converter Control Design

The main converter is a C-Class DC chopper with bidirectional current flow capability. The specifications of the main winding converter are shown in Table 3.2.

Table 3.2: Main Converter Design Specifications

	Variable	Value	Unit
Nominal input voltage	V_s	12	V
Nominal output voltage	V_{dc}	24	V
Inductor current ripple	Δi_s	45%	
Rated inductor current	I_s	6	A
Output voltage ripple	Δv_{dc}	10%	
PWM switching frequency	f_{sw}	20	kHz

The average model of the converter can be derived from the dynamic equations of the converter in a complete switching period.

$$L_s \frac{di_s(t)}{dt} = v_s(t) - (1 - d_s(t))v_{dc}(t) \tag{3.2}$$

$$C_{dc} \frac{dv_{dc}(t)}{dt} = i'_s(t) - i_o(t) \tag{3.3}$$

where v_s , d_s , v_{dc} , i_s , i'_s , C_{dc}, and i_o are the source voltage, the duty cycle, the dc-link voltage, the source current, modulated source current, dc-link capacitor, and the load current respectively. The transfer functions of the plants can be obtained using Laplace transform.

$$i_s(s) = \frac{V_{dc}}{sL_s} d_s(s) + \frac{V_{s(s)} - V_{dc}(s)}{sL_s} \tag{3.4}$$

$$V_{dc}(s) = \frac{1}{sC_{dc}} i'_s(s) - \frac{1}{sC_{dc}} i_o(s) \tag{3.5}$$

The first terms in (3.4) and (3.5) influence the dynamics of the system and the second terms are disturbances. The controllers are designed for the transfer functions shown in (3.6) and (3.7). The inner current loop is required to have faster response, as such the bandwidth ($\omega_{nc} = 2\pi f_{sw}/40$) of the current controller is selected to be much higher than the bandwidth of the dc-link voltage controller ($\omega_{nv} = 2\pi f_{sw}/400$).

The reduced transfer functions of the bidirectional converter and the dc-link can be expressed as in (3.6) and (3.7) in respective order.

$$G\_I(s) = \frac{i_s(s)}{d_s(s)} = \frac{V_{dc}}{sL_s} \tag{3.6}$$

$$G\_V(s) = \frac{V_{dc}(s)}{i'_s(s)} = \frac{1}{sC_{dc}} \tag{3.7}$$

The above expressions show that the dynamics of the converter is influenced by the power inductor and the dc-link capacitor. Since the transfer functions are first order systems, the control can be easily achieved using PI controllers by relating the general second order system (3.8) with the closed loop of the plant. The gain parameters of controllers are calculated analytically using the procedures presented in [115]. The general second order system is shown in (3.8).

$$G_{so}(s) = \frac{{\omega^2}_n \left(\frac{s}{z} + 1\right)}{s^2 + 2\zeta\omega_n s + {\omega^2}_n} \tag{3.8}$$

where ω_n is the undamped natural frequency, ζ is the damping factor, and z is the zero. The design specification ζ is chosen as 0.707 and ω_n is selected in accordance to the speed of the controllers needed. The closed-loop transfer function of the current plant (Tcl_I) and the PI controller can be expressed as:

$$Tcl\_I = \frac{i_s(s)}{{i^*}_s(s)} = \frac{\frac{K_p^c}{L_s}\left(s + \frac{K_i^c}{K_p^c}\right)}{s^2 + \frac{K_p^c V_{dc}}{L_s} s + \frac{K_i^c V_{dc}}{L_s}} \tag{3.9}$$

K_p^c and K_i^c are the proportional and integral gains of the current controller (PI). Comparing expression (3.9) with the general second order system in (3-8). The parameters can be calculated by choosing the required natural frequency and damping ratio.

$$K_p^c = \frac{2\omega_{nc}\zeta L_s}{V_{dc}} \tag{3.10}$$

$$K_i^c = \frac{\omega^2{}_{nc} L_s}{V_{dc}} \tag{3.11}$$

Likewise, the closed-loop transfer function (Tcl_V) of the dc-link can be written as:

$$Tcl\_V = \frac{V_{dc}(s)}{V^*{}_{dc}(s)} = \frac{\frac{K_p^v}{C_{dc}}(s + \frac{K_i^v}{K_p^v})}{s^2 + \frac{K_p^v}{C_{dc}}s + \frac{K_i^v}{C_{dc}}} \tag{3.12}$$

Using the same approach, the PI gains for the voltage controller are calculated by (3.13) and (3.14).

$$K_p^v = 2\omega_{nv}\zeta C_{dc} \tag{3.13}$$

$$K_i^v = \omega^2{}_{nv} C_{dc} \tag{3.14}$$

By referring to the main converter control layer depicted in Figure 3.1, the reference current for the main winding is obtained from the dc-link controller. The dc-link controller input is the error signal obtained from the desired voltage reference and the actual dc-link voltage. The error signal is processed by the PI controller with gains designed in (3.13) and (3.14) to give the reference current across the power inductor. The current controller processes error signal obtained from the difference of the reference current and the actual measured current and accordingly provides control signals. This output is used as a reference signal to generate the PWM signals for controlling the power electronic switches of the bidirectional converter.

3.3.2 Auxiliary Converter Control Design

A buck converter is selected as an auxiliary converter for providing the controlled current for the VI. The specifications of the converter are presented in Table 3.3. In the actual implementation, the load is replaced by the auxiliary winding. The reduced average model of the buck converter without and with auxiliary winding as its load are depicted in Figure 3.4 (a) and (b), respectively.

Table 3.3: Auxiliary (Buck) Converter Design Specifications

	Variable	Value	Unit
Nominal Input Voltage	V_{in}	12	V
Nominal output voltage	V_o	3	V
Current ripple	Δi_b	5%	-
Voltage ripple	Δv_o	10%	-
PWM switching frequency	f_{sw}	20	kHz

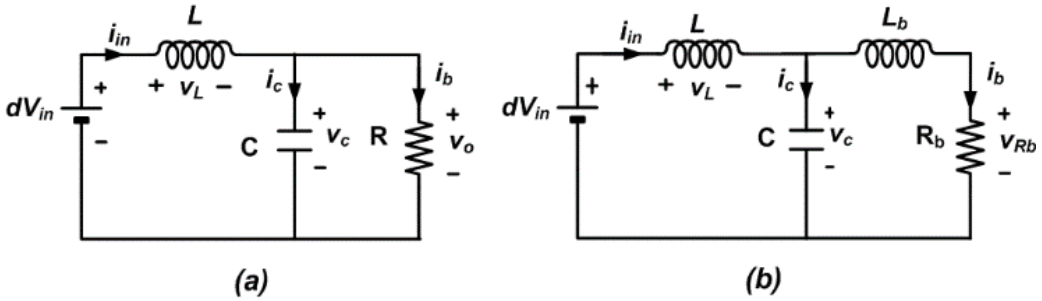

Figure 3.4: (a) Reduced average model of buck converter with Resistive load:(b) Reduced average model of buck converter with auxiliary winding as load

The equations of the reduced average model of the buck converter, which is shown in Figure 3.4 (a), can be written as:

$$L\frac{di_{in}(t)}{dt} = dV_{in}(t) - v_c(t) \tag{3.15}$$

$$C\frac{dv_c(t)}{dt} = i_{in}(t) - \frac{v_c(t)}{R} \tag{3.16}$$

Combining (3.15) and (3.16), then replacing $v_c = i_b R$, and taking the Laplace transform. The output current to the control transfer function can be written as (3.17).

$$\frac{i_b(s)}{d(s)} = \frac{V_{in}}{RLCs^2 + Ls + R} \tag{3.17}$$

When the load is replaced by the auxiliary winding circuit, which consists of an inductance and a series resistance, the above model will be changed into a more complex third order system as shown in (3.18).

$$\frac{i_b(s)}{d(s)} = \frac{V_{in}}{L_b LCs^3 + R_b LCs^2 + Ls + R_b} \tag{3.18}$$

However, the third pole is very far from the dominant poles hence the system can be reduced. The characteristics of the designed buck converter is highly influenced by the auxiliary winding. Consequently, the third order model of the system is approximated by a first order transfer function of the auxiliary winding circuit.

The conventional PI controller is selected and the design of the control parameters is performed using the procedures used previously. The closed-loop transfer function can be written as:

$$\frac{i_b(s)}{i^*_b(s)} = \frac{\frac{K_p^b}{L_s}(s + \frac{K_i^b}{K_p^b})}{s^2 + \frac{(R_b + K_p^b)}{L_b}s + \frac{K_i^b}{L_b}} \tag{3.19}$$

where K_p^b and K_i^b are the proportional and integral gain of the auxiliary winding current controller respectively. The superscript * is to indicate a reference (set) value of a signal. In this study, the controller is designed based on ζ (0.707) and ω_n is selected to be 1/20 times the switching frequency in rad/s to make it much faster than the main winding current controller.

By comparing the denominators of equations (3.19) and (3.8), the gain parameters of the controller are determined as in (3.20) and (3.21).

$$K_i^b = 2\omega_{nc}\zeta L_b - R_b \tag{3.20}$$

$$K_i^b = \omega^2_{nc} L_b \tag{3.21}$$

Referring to the auxiliary converter control layer in Figure 3.1, the reference current of the current controlled auxiliary converter is obtained from the control current estimator block. For practical implementation of the controllers in the microcontroller, Tustin approximation method is used for digital conversion.

3.3.3 Global Control Operation

As it is revealed in Figure 3.1 the control layer consists of the main converter control layer and the auxiliary converter control layer. The first consists of the dc-link controller and the current controller, while the second

one is composed of the reference current estimator block and the auxiliary current controller. The main winding reference current is obtained from the dc-link controller.

In the auxiliary converter control block, the auxiliary current estimator is determined from a series of tests. For several current levels in the main winding, the control current is varied in steps of 0.05 A until a minimum ripple current is noticed for each main current. Then the curve fitting approach is used to determine the control function (relationship) relating the auxiliary winding and main winding currents. This enables an automatic closed loop (integrated) control of the overall system. After obtaining the mathematical relationship between the two currents, the integrated closed loop system that consist of the closed loop of the main converter and the closed loop of the auxiliary converter with its current estimator block is implemented in a microcontroller. The curve, which shows the relationship between the two currents, is shown in Figure 3.5. As it is clearly shown, for currents less than 6.5 A, the auxiliary winding is idle, hence, the control current is zero. However, for currents greater than or equal to the saturation current, an appropriate control current is applied to the auxiliary winding in accordance to the curve shown in Figure 3.5.

3.4 Experimental Setup and Results

The experimental setup consists of a C-Class DC chopper IGBT topology (1200 V, 100 A) operating in continuous conduction mode powered by two batteries in parallel, a current controlled buck converter, power supplies, measuring instruments, RLC meter and C2000 launch pad Piccolo platform microcontroller. For interfacing the measurement signals to the microcontroller and the control signals to the IGBTs an interface PCB was manufactured. The conventional power inductor is replaced by the selected VI-prototype presented in section 3.2 B. The buck converter is built in a PCB mounting approach and its controller is implemented in the same microcontroller.

To emulate the dynamic behavior of the EV traction system, two batteries and a resistive load are used as a variable load. A 3.3 mF, 400 V capacitor is used as dc-link capacitor and a voltage sensor is used to measure its voltage. Two current sensors are also used for measuring the main winding current and the auxiliary winding current. As a small current variation in the auxiliary winding can influence the effective inductance of the main winding, a precision current sensor is selected. The experimental set up is shown in Figure 3.6.

The experiments in this section are focused on the global system in order to clearly understand the effects and improvements due to the introduction of the VI to the bidirectional converter. For that, its characteristic is studied both without and with the activation of the auxiliary winding. As such, the main winding current

is varied until the saturation current level is reached and beyond. As a result, it is found that operating the power inductor above the saturation limit leads to higher current ripples. This results in the heating of the switching devices and distortion in the current waveform, as expected by the theory. The experimental results for characterizing the ripple levels due to the variations of the main current are summarized in Table 3.4.

It can be clearly shown that the increase of current in the main winding results in more ripple. Increasing the duty cycle from 0.50 to 0.70 increases the peak-to-peak current ripple significantly. For instance, for D = 0.65 and D = 0.70, the ratio of peak-to-peak current ripple reaches 90.16% and 91.00% respectively. Such a high ripple results in more losses, affecting the efficiency and performance of power converters. This describes the typical behavior of such converters for applications with a wide range of load variations, if the power inductor in the converter is pushed to operate in the saturation region. After carefully analyzing the characteristics of the power inductor with the increase of current in the main winding, the auxiliary winding is activated, and a controlled current is injected to it. This current helps in regulating the effective inductance of the main winding by changing the permeability of the magnetic core.

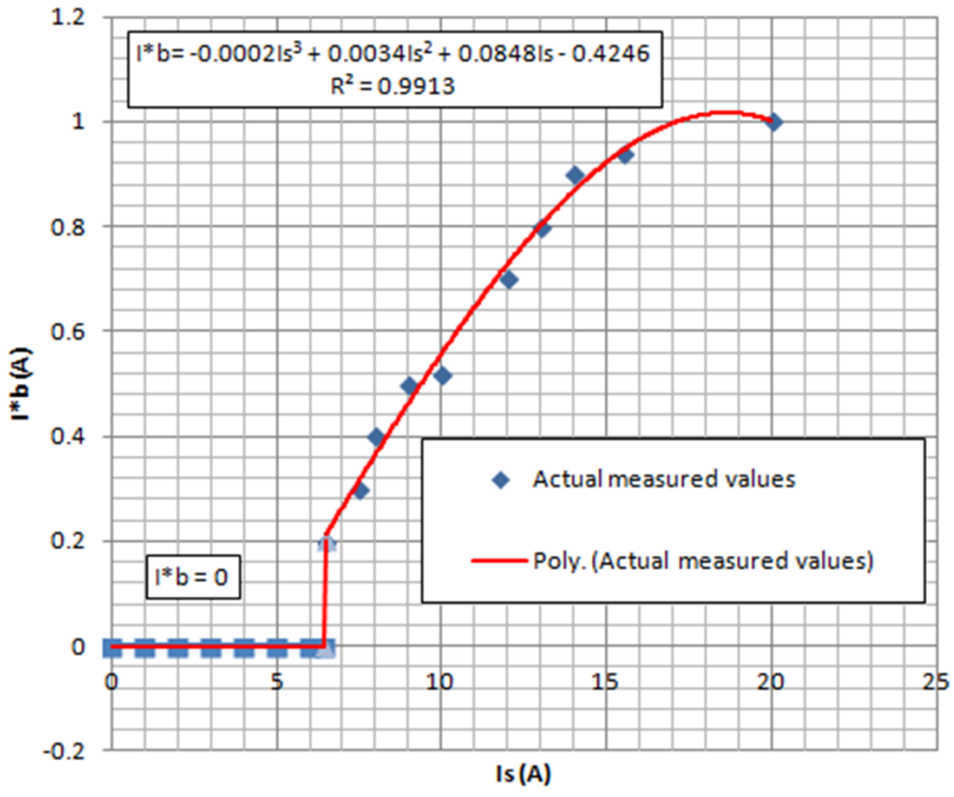

Figure 3.5: Auxiliary winding reference current and the main winding current relationship curve

For the last two cases in Table 3.4, a control current is applied in the auxiliary winding to quantify the amount of ripple improvements and the current handling capability of the power inductor. For D = 0.65, the amount of current ripple is 90.16%, when no control current is injected into the auxiliary winding. However, by injecting a control current of 0.75 A (Figure 3.7 (b)) and 1 A (Figure 3.7 (c)), the amount of current ripple can be reduced by 40.90 % and 38.20 % in respective order. It is important to note in this case; the current waveforms show that injecting a control current in the auxiliary winding not only reduce the amount of current ripple but also enhance the current handling capability of the power inductor.

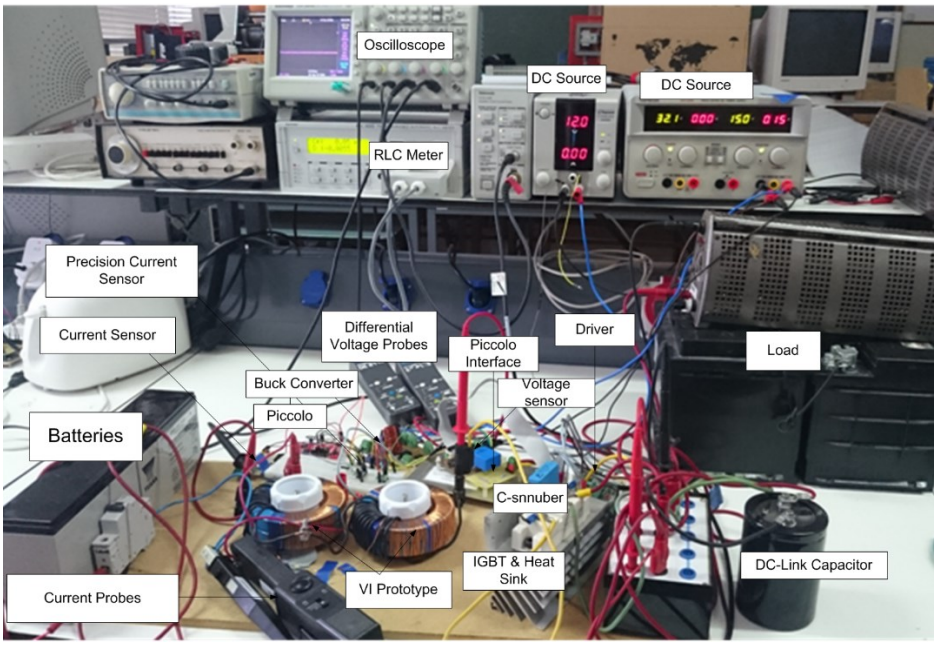

Figure 3.6: Experimental setup of VI-based converter test bench

In Figure 3.7, the average current is twice the rated current of the power inductor. If no control current is applied, the power inductor is forced to operate in saturation region. Nonetheless, with a control current, the power inductor can be pushed to operate in partial saturation, which results in the current ripple control and improving the current handling capability of the power inductor.

Table 3.4: Ripple Variations with the Increase of Current

Duty Cycle	$I_{s_{rms}}$ (A)	$I_{s_{avg}}$ (A)	Peak to Peak Ripple Δ_{i_s} (A)	Ripple (%)
0.50	3.94	3.77	1.6	42.44
0.52	3.96	3.94	1.76	44.67
0.58	6.3	6.24	3.6	57.69
0.60	7.79	7.7	4.8	62.34
0.62	8.81	8.25	6.8	82.42
0.63	9.39	9.22	8	86.77
0.64	11.5	11.3	9.8	86.73
0.65	12.8	12.2	11	90.16
0.70	17.78	17.2	15.65	91.00

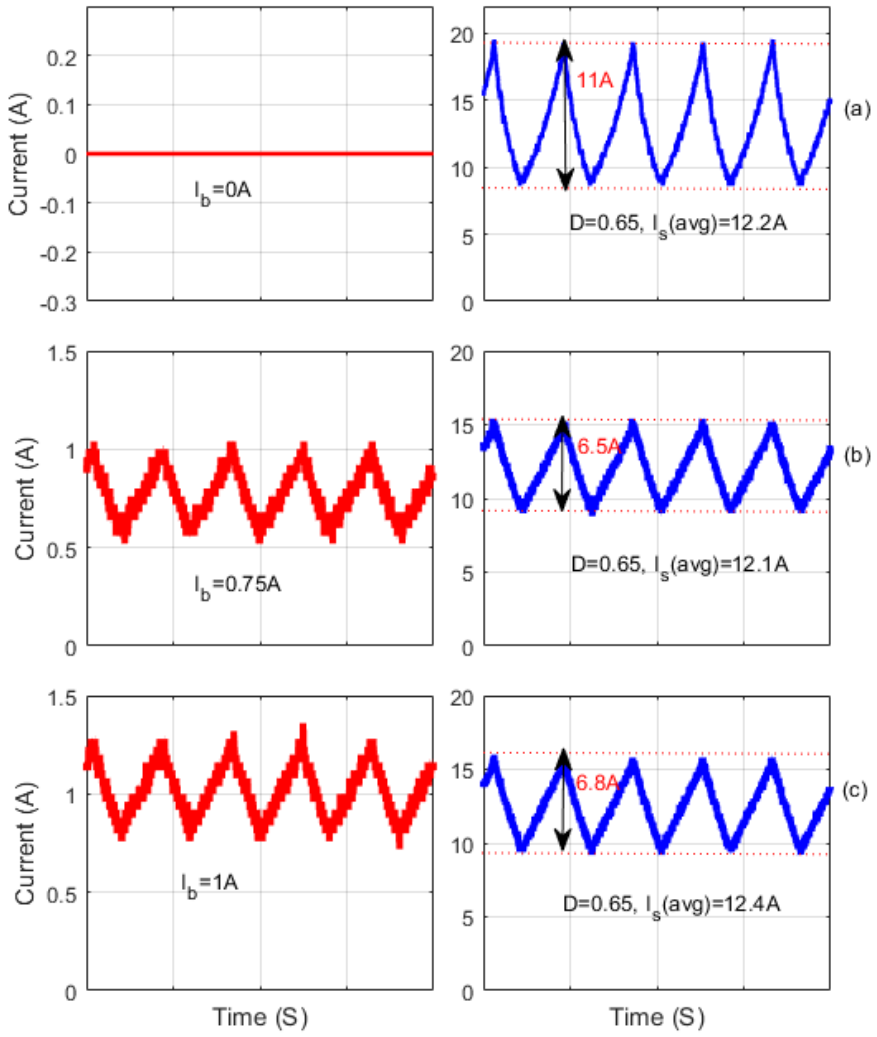

Figure 3.7: Experimental results for D = 0.65 with control current in the auxiliary winding

Similarly, as shown in Figure 3.8 (b) and (c), for the D = 0.70, a control current of 0.70 A and 0.85 A are applied and the current ripple in the main winding is reduced by 20% and 36% in respective order. In this case, the ripple current is reduced significantly, but as the level of current is much higher than the rated current of the power inductor, the power inductor operates in the saturation region. From the results shown in Figure 3.8, the VI can be used with about 2.9 times the rated current of the power inductor.

At these levels of current, the power inductor is saturated, but with the injection of a control current, its operating point can be forced to move from deep saturation to saturation region closer to the transition region. This leads to a significant current ripple reduction, resulting in the reduction of losses.

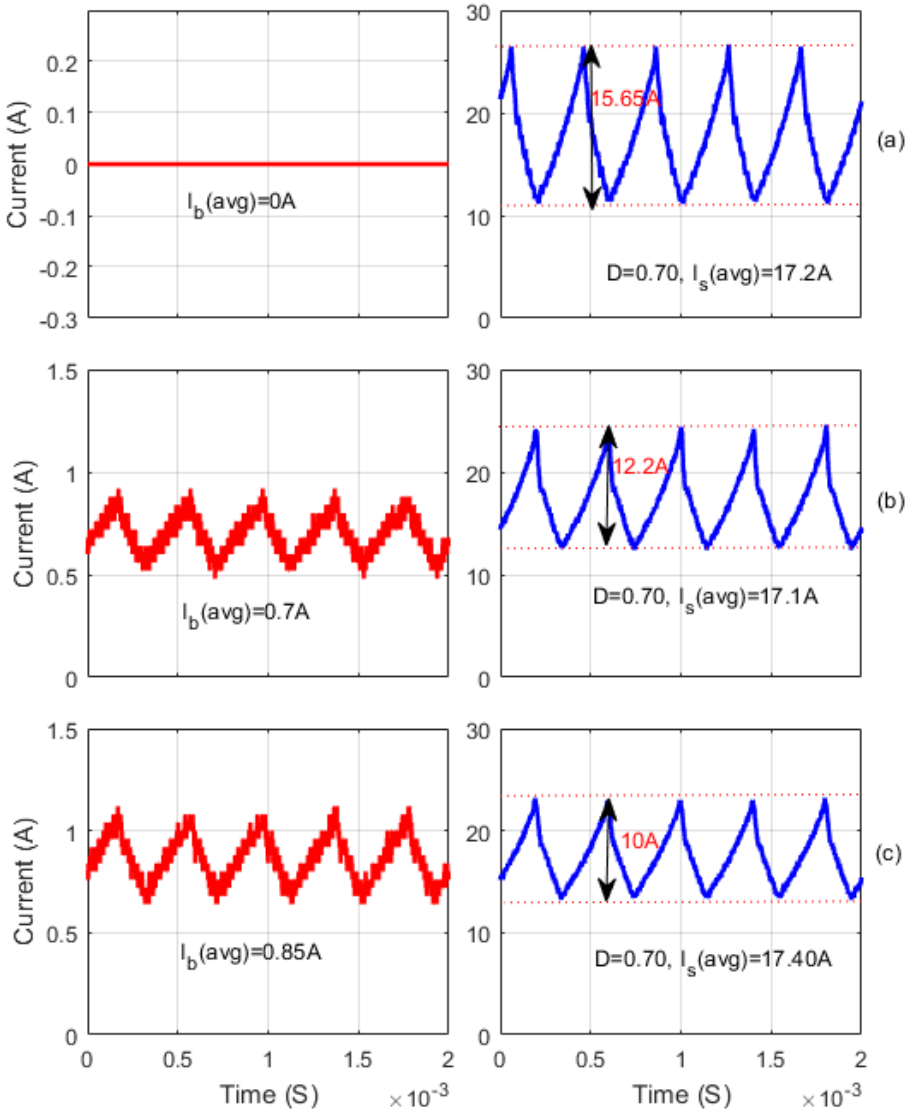

Figure 3.8: Experimental results for D = 0.70 with control current in the auxiliary winding.

The injected auxiliary winding current pre-bias the magnetic core and helps in cancelling part of the main flux in the main winding that enables the magnetic core to operate in partial saturation. This operation regulates the effective permeability of the magnetic cores resulting in adjusting the inductance of the power inductor. This helps in the ripple control and enhances the current handling capability of the power inductor.

Some of the experimental results of the integrated closed loop operation of the overall system (including now the auxiliary current level estimator) are presented in Figure 3.9. In each plot, the auxiliary winding current and main converter current is drawn in the left side and in the right side, respectively.

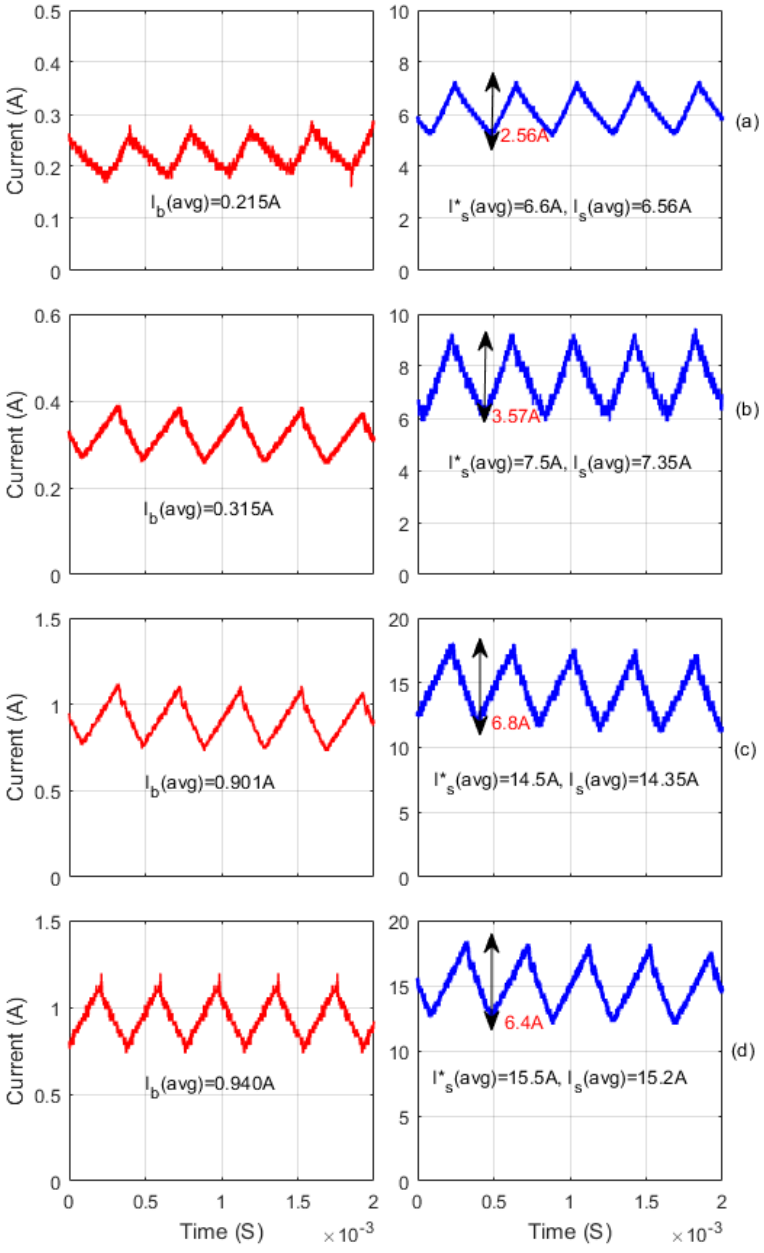

Figure 3.9: Closed Loop Results

As it can be clearly shown in Figure 4.9, there is very slight difference between the measured current and the reference current, this is mainly due to the noisy nature of the current sensor used.

It can be also shown that the closed loop system provides better control of the current ripples. In Figure 3.9 (d), the main winding current is 15.2 A, which is 2.53 times higher than the rated current of the inductor. At this level of current, with the help of the integrated control, a controlled auxiliary winding is applied and the current ripple is kept 42.1%, which is much better than the open loop result with less main current (12.2 A) in Figure 3.7. Furthermore, as it takes into considerations the current levels of the main winding, it provides precise regulation of the inductance and control of current ripples.

3.5 Conclusion

This paper presents the viability of VI based bidirectional DC-DC converter for applications with a wide range of load variation such as EV. The conventional power inductor in DC-DC converter is replaced by VI in order to have better ripple control, enhanced current handling capability and adaptive control of the saturation level of a power inductor. To achieve the aforementioned goals, a low-cost, and low-power biasing circuit is built and a mathematical relationship that relates the auxiliary winding current with the levels of the main winding current is developed. The validity of the proposed VI, the biasing circuit and the improved DC-DC converter are verified through experimental tests. From the experimental results, it can be deduced that, with a small auxiliary winding current, the current handling capacity of a power inductor can be significantly improved. For currents twice the rated current, the ripple current is reduced from 11 A to 6.5 A, which is 40.90 % reduction. Similarly, for currents 2.9 times larger than the rated current the current ripple is reduced from 15.65 A to 10 A (36.10 % decrease). It should be noted that for this level of current, the core is still in saturation, but the current ripple can still be reduced. Therefore, with the same core size the current handling capability is greatly improved, hence a remarkable step for core size miniaturization of magnetic components. The long-term plan of this work is to develop VI-based converters for EV applications and full-scale validation.

3.6 Acknowledgment

The authors would like to thank Mr. F. Machado for his help in the implementation of the experimental test bench.

Chapter 4 Characterization of variable inductors using finite element analysis

Original Title: Characterization of variable inductors using finite element analysis

Authors and affiliation:

- **Mebrahtom Woldelibanos Beraki**: PhD Student, Université de Sherbrooke, Faculté de génie, Département de génie électrique et de génie informatique
- **João P. Trovão** : Professor, Université de Sherbrooke, Faculté de génie, Département de génie électrique et de génie informatique
- **Marina S. Perdigão:** Professor, Instituto de Telecomunicações and Polytechnic Institute of Coimbra, 3030-290 Coimbra, Portugal

Date of Acceptance: July 6, 2019

State of acceptance: Published

Reference: Simulation Modelling Practice and Theory, DOI: 10.1016/j.simpat.2019.101952

Summary

Content: This paper uses Finite Element Analysis tool MagNet software to characterize the VI in order to verify its feasibility for DC-DC converters with wide range of load variations. The inductance characterization, the losses and improvements in the saturation level are used to quantify the capability of the VI. The characterization and analysis presented in this paper is essential for researchers and designers to integrate the VI in converters and useful in choosing suitable VI configurations for their application. Moreover, the theoretical aspects presented in this paper will be vital for development of analytical ways for the characterization of such kind of devices. The inductance characterization obtained from FEM simulations agree with the experimental values with a mean squared error of 1.6%. Furthermore, for a current of more than twice the rated current, the differential inductance is increased by 56 times with control current in the auxiliary winding. This reveals the potential significance of VI for enhancing the current handling capability and core utilization leading to core size reduction in power electronic converters.

Results: The linkage flux (λ-i_s) curves, the differential inductances as function of the main and auxiliary winding currents, the inductance characterization curves (L-i_s), the power losses and flux distributions are extracted from FEM simulations to reveal the characteristics of VI and its significance. The simulation results validate the capability of the VI and will be useful in the design and selection of more suitable VI for power converters in traction applications. Moreover, the λ-i_s characterization curves are essential for deducing a control strategy for obtaining the auxiliary winding current as a function of the main winding current to implement a closed loop control scheme for the VI based converter topologies that is presented in Chapter 7.

Contribution to the thesis: The main contribution of this article to the thesis, is to provide a detailed characterization of VI and reveal the significance of VI in improving the current handling capability. The results obtained in this article are essential for selecting suitable VI topologies, design of VI and deducing a control strategy for estimating the auxiliary winding currents as function of the main winding currents. This article supplemented the work presented in Chapter 3 and will be essential for the next chapters.

Abstract

The variable inductor (VI) uses a small DC current to regulate the permeability of magnetic cores. Nonetheless, this magnetic device is composed of magnetic cores and multiple windings, which leads to a more complex geometry. Its magnetic properties variations and non-linear behavior complicate its modelling, analysis and its characterization. This paper uses Finite Element Analysis tool MagNet software to characterize the VI in order to verify its feasibility for DC-DC converters with wide range of load variations. The inductance characterization, the losses and improvements in the saturation level are used to quantify the capability of the VI. The characterization and analysis presented in this paper will be a good base for researchers and designers to integrate the VI in converters and help them in choosing suitable VI configurations for their application. Moreover, the theoretical aspects presented in this paper will be essential for development of analytical ways for the characterization of such kind of devices. The inductance characterization obtained from FEM simulations agree with the experimental values with a mean squared error of 1.6%. Furthermore, for a current of more than twice the rated current, the differential inductance is increased by 56 times with control current in the auxiliary winding. This reveals the potential significance of VI in improving the current handling capability and core utilization leading to core size reduction in power electronic converters.

Keywords

DC-DC converter, linkage flux, magnetic core, saturation, variable inductor

4.1 Introduction

Magnetic components, particularly power inductors, are vital components in power electronic converters (PECs) [116], [117]. However, they are bulky and dominate the size, weight, volume and power density of PECs [118], [119]. Hence, they are a critical bottleneck in the miniaturization of PECs in several applications such as in traction applications [120]. This is mainly due to the saturation constraint of the magnetic core and conductors wound around the magnetic core [106].. One way to deal with the saturation limited power inductor is to replace it with a current controlled variable inductor (VI). The VI is a magnetic device that uses a small control current to regulate the permeability of a magnetic core and provides wider flexibility in controlling the magnetic properties of the magnetic material [73]. This feature of the VI makes it suitable for improving the current handling capability of magnetic core materials leading to the improvement in core utilization and core size reduction. This attribute of this device makes it suitable for DC-DC converts with wide range of load variations. As the size of the DC-DC converters is dominated by the power inductor. Replacing the classical power inductors with VI for such converters will be essential in their miniaturization.

The variable inductor is a very powerful and promising device that can have considerable practical applications. This device has been effectively used in power control of resonant filters, in lamp driver applications, in LED lamp drivers, inductive power transfer [121] for maximum power tracking (MPPT) in PV systems [81], electric lighting systems [82], [83], VAR compensation in electrical power system networks [122], and electric vehicles [16]. Furthermore, it has worth recording applications in resonant AC and DC-DC converters [85], power flow control and fault current limiting [86], harmonic control and voltage regulations [71].

Nonetheless, this device is composed of magnetic cores, multiple windings, with an interaction of magnetic and electrical parameters. Furthermore, it has a complex geometry, diverse magnetic properties, and non-linear behavior. These make the VI more complex to model, characterize, analyze its performance and understand its operation. There are several methods to model the non-linear inductance of classical power inductors [123], [124], [125], [126], which reveal the non-linear variation of the inductance in different operating conditions. These methods are suitable for single winding inductors. Unlike the classical power inductors, the VI is composed of multiple windings and magnetic core with an interaction of different currents. The interaction of different currents leads to parametric coupling leading to higher voltage induction in the auxiliary winding, which can lead to the damage of the auxiliary windings. Hence, a comprehensive way of characterizing and analyzing the device taking into consideration the interaction of the two currents

is essential for integrating it to power electronic converters. Furthermore, simplified closed-form equations to present its operation and the voltage induced due to the interactions of the main winding and auxiliary winding currents will be essential in selecting suitable VI configurations.

The reluctance network based SPICE modelling, magnetic reluctance equivalent circuit (MEC) and the Finite Element Method (FEM) analysis are the most commonly used methods for the analysis and understanding of the complex electromagnetic phenomena of such kind of devices [127], [128], [129]. The reluctance-based SPICE modelling is faster and provides a reasonable result with less accuracy compared to FEM. A systematic SPICE modeling of this device, which reveals the interaction of the electrical and magnetic properties based on the reluctance equivalent circuit is illustrated in [127]. The models developed using SPICE provide a deeper insight in the operation of the magnetic device, nonetheless, the characterization of the VI are presented only as function of the auxiliary winding currents and no information is provided about the losses in such models. Similarly, the MEC modeling is based on reluctance network, it offers faster simulations, and is very useful for optimizing system performances, but such models might have convergence issues when saturation operation of magnetic devices are under consideration [129]. Furthermore, there are no commercial software packages for this modeling approach [130]. Both the reluctance network-based SPICE modeling and MEC are limited if detailed studies such as switching effects, materials non-linearity, saturation effects and detailed characterization of magnetic devices and losses are needed.

On the other hand, FEM is a powerful tool which has been proved to be effective in modeling of several magnetic devices such as transformers, inductors and motors [128],[131], [132]. It offers better accuracy but requires considerable time in modelling and simulation of such magnetic devices. It is essential to extract useful parameters to understand the operation, performance and integration the magnetic devices to system applications. Furthermore, it provides flexibility in changing magnetic and electrical parameters, making the design and selection of magnetic devices such as the VI easier. Considering, its accuracy, its capability to deal with intricate magnetic structures and physical significance, the FEM analysis is used to verify the significance of the magnetic device (VI) for enhancing the current handling capability of magnetic cores for applications with wide range of load variations.

The FEM simulation of the classical power inductors, coupled inductors and planner inductors is presented in [133], [134], [135], [136]. Nonetheless, FEM simulation of VI is presented only in [137], [138]. Both authors use an E-type core, where there is both magnetic and electrical coupling between the two groups of windings. Furthermore, both authors focused on the flux distribution, inductance variation as a function of the auxiliary winding current and the saturation regions identification. Nonetheless, the detailed

characterization of the VI that includes the variation of its parameters as function of the main and auxiliary currents, the losses and the impact of auxiliary winding induced voltage due to currents in the main winding are not yet addressed in literature. All these effects and characterizations are essential for the integration of the device in power electronic converters.

The main objective of this paper is to provide the detailed modeling, analysis and characterization of a decoupled double toroidal core small-scale VI prototype taking into consideration the parametric coupling of its currents. This approach is fundamental to extract essential parameters to study its feasibility in enhancing the current handling capability of magnetic cores in power electronic converters. It is used for the characterization of a decoupled double toroidal-based VI and it can be adopted to other VI configurations. Furthermore, the VI configuration with the auxiliary windings connected in such a way to cancel out the voltage induced on the auxiliary winding due to the main winding current is considered suitable; nonetheless, a detailed study on why this configuration is suitable is still not addressed. This paper also includes the detailed mathematical expressions to illustrate the phenomena and analyze its impact using FEA simulations. The linkage flux (λ-i_s) curves, the differential inductances as function of the main and auxiliary winding currents, the inductance characterization curves (L-i_s), the power losses and flux distributions are extracted from FEM simulations to reveal the characteristics of VI and its significance. For extracting the L-i_s curve, the finite difference approximation method is used in order to consider the saturation region operation of the power inductor. The simulation results validate the capability of the VI for applications with wide range of load variations and is helpful in the design and selection of more suitable VI for power converters in traction applications. Moreover, the λ-i_s characterization curves are essential for deducing a control strategy for obtaining the auxiliary winding current as a function of the main winding current to implement a closed loop control scheme for the VI based converter topology.

Section 4.2 provides an overview of the study system. The detailed analytical expressions of the parametric coupling of two possible VI configuration are illustrated in section 4.3. The FEM modeling and the parameters used in the FEM simulation are explained in section 4.4. Section V provides the simulation results and the analysis of the results. The conclusions and future directions are discussed in the last section.

4.2 Study System Description

The studied VI is used in a reduced-scale bidirectional DC-DC traction converter, as shown in Figure 4.1, and highlighted in green, it replaces the conventional inductor. VI is composed of two groups of windings, the main windings and the auxiliary windings, and magnetically decoupled two toroidal cores.

The auxiliary windings use a small current to control the saturation level of the magnetic core by canceling part of the magnetic flux in the main winding. It is important to note that auxiliary winding is idle in normal operation; it is only activated when the power inductor is pushed to operate at currents higher than its saturation limit. In this situation, the DC flux injected in the auxiliary winding will force it to operate in partial saturation. Hence, the same inductor can be used with higher currents enabling the magnetic core to be used at its fullest potential.

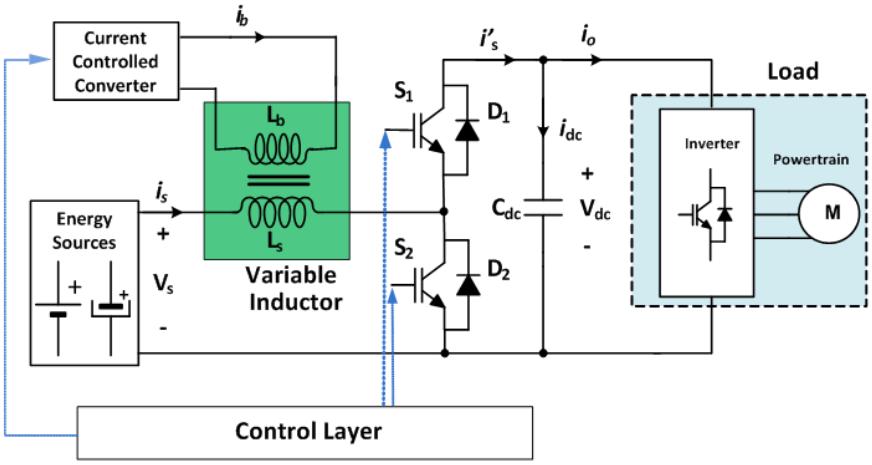

Figure 4.1: A variable inductor in a traction DC-DC converter

The detailed modeling of the overall system in relation to the control and the significance of VI in ripple control for such kind of converters has been studied in[139]. The main windings of each core are connected in series with one another. Similarly, the auxiliary windings are also connected in series, but the windings are wound in such a way the net induced voltage in the auxiliary winding due to the main winding current is canceled. As revealed in Figure 4.2, the VI is realized by two magnetically decoupled cores. The use of two decoupled magnetic cores helps in reducing the magnetic coupling between the same windings and reduce the parametric coupling between the main winding and auxiliary winding [77]. Due to this effect, a huge voltage will be induced in the auxiliary winding due to the variation of the main winding current; this may damage the auxiliary winding circuit. To avoid this issue we use a double core decoupled VI topology.

The number of turns in the auxiliary windings are made much higher than that of the main winding; in order to have smaller control currents in the auxiliary winding. Having higher number of turns helps in increasing the control flux with smaller control current.

4.3 Variable Inductor operation and voltage induced in the auxiliary winding

Before presenting the simulation and characterization of the VI, it is vital to introduce the analytical and theoretical aspects of the VI. As it is revealed in Figure 4.2, the magnetic properties of the magnetic material can be regulated using the two configurations Figure 4.2 (a) and (b). In the first case (Figure 4.2 (a)), the magnetic fields cancel out in core 1 but they add up in the core 2. Whilst in Figure 4.2 (b), the magnetic fields cancel each other in both cores. To understand the significance and the overall performance of the power inductor, both configurations are studied in terms of voltage induced in the auxiliary winding due to the main winding current.

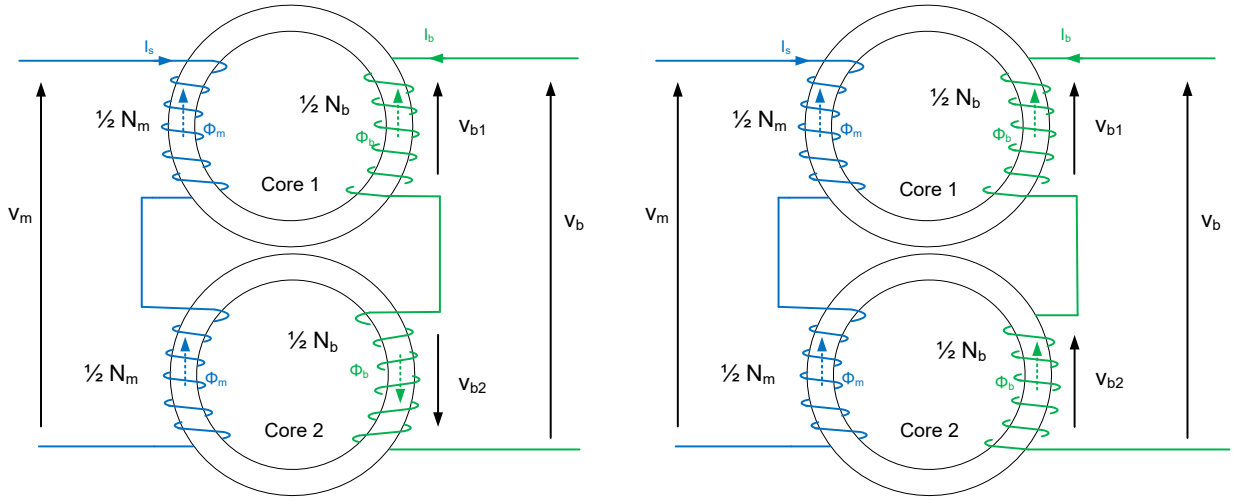

Figure 4.2: Two variable inductor configurations considered in this study (a) auxiliary winding voltage cancelling (b) auxiliary winding voltage adding

From Faraday's law of electromagnetic induction, a changing magnetic flux across a conductor induces an electromotive force. Mathematically,

$$v(t) = N \frac{d\phi(t)}{dt} \tag{4.1}$$

where N is the number of turns and $\phi(t)$ is a magnetic flux. Furthermore the $\phi(t)$ can be expressed as:

$$\phi(t) = \oint B \ dA = BA \tag{4.2}$$

where B is the magnetic flux density, dA is an increment of surface area and A is the cross-sectional area of the magnetic core. In the VI prototype, the main winding number of turns (N_m), as well as auxiliary winding number of turns (N_b) are split into two equal parts. Subsequently, the voltage equations of the main winding and the auxiliary winding of VI in Figure 4.2 (a) can be written as (4.3) and (4.4) respectively.

$$V_m = \frac{A_c N_m}{2} \frac{dB_1}{dt} + \frac{A_c N_m}{2} \frac{dB_2}{dt} \tag{4.3}$$

$$V_b = \frac{A_c N_b}{2} \frac{dB_1}{dt} - \frac{A_c N_b}{2} \frac{dB_2}{dt} \tag{4.4}$$

where V_m, V_b, A_c, B_1, B_2 are the voltage induced in the main winding, the voltage induced in the auxiliary winding, the cross-sectional area of the core, the magnetic field density in core 1 and the magnetic field density in core 2 respectively. The magnetic field intensity as a function of both the main winding and auxiliary winding parameters can be written as:

$$H_1 = \frac{N_m i_s - N_b i_b}{2l} \tag{4.5}$$

$$H_2 = \frac{N_m i_s + N_b i_b}{2l} \tag{4.6}$$

where H_1, H_2, i_s, i_b and l are the magnetic field intensity of core 1 and core 2, the main winding current, the auxiliary winding current and the mean length of the magnetic core respectively. In magnetic materials, the magnetic flux density and the magnetic field intensity are related by the permeability of the material (μ) as:

$$B = \mu H \tag{4.7}$$

Hence, B_1 and B_2 can be expressed as functions of the main winding and the auxiliary winding currents as:

$$B_1 = \mu_1 \left(\frac{N_m i_s - N_b i_b}{2l}\right) \tag{4.8}$$

$$B_2 = \mu_2 \left(\frac{N_m i_s + N_b i_b}{2l}\right) \tag{4.9}$$

where μ_1 and μ_2 are the permeability of core 1 and core 2 respectively. They are variable and depend on the operating point on the B-H curve. Substituting (4.8) and (4.9) in (4.3) and (4.4), the voltage induced in the main winding can be expressed as:

$$V_m = \frac{N_m A_c}{4l}\frac{d}{dt}\left[\, \mu_1 \left(N_m i_s - N_b i_b\right) + \mu_1 (N_m i_s + N_b i_b) \,\right] \tag{4.10}$$

It can be further expressed as in (4-11):

$$V_m = \frac{N_m A_c}{4l}\left[\left(N_m i_s - N_b i_b\right)\frac{d\mu_1}{dt} + \mu_1 N_m \frac{di_s}{dt} - \mu_1 N_b \frac{di_b}{dt} + \left(N_m i_s + N_b i_b\right)\frac{d\mu_2}{dt} + \mu_2 N_m \frac{di_s}{dt} + \mu_2 N_b \frac{di_b}{dt}\right] \tag{4.11}$$

As a constant control current is demanded in the auxiliary winding circuit and core 2 is forced to saturation, the terms with $(di_b)/dt$ and $(d\mu_2)/dt$ will vanish in (4.11). Hence, the voltage equation of the main winding will be simplified to (4.12):

$$V_m = \frac{N_m A_c}{4l}\left[\left(N_m i_s - N_b i_b\right)\frac{d\mu_1}{dt} + N_m(\mu_1 + \mu_2)\frac{di_s}{dt} \right] \tag{4.12}$$

It is clearly shown in (4.12) the main winding voltage heavily depends upon the main winding parameters. The term $(N_m i_s - N_b i_b)$ reveals that there is an effect due to the auxiliary winding as well. Nonetheless, the magnitude of the contribution from the term $(N_m i_s - N_b i_b)$ is small as will be illustrated by FEM simulations in section 4.5.2.

Similarly, the voltage across the auxiliary winding will be:

$$V_b = \frac{N_b A_c}{4l}\Big[(N_m i_s - N_b i_b)\frac{d\mu_1}{dt} + \mu_1 N_m \frac{di_s}{dt} - \mu_1 N_b \frac{di_b}{dt} + (N_m i_s + N_b i_b)\frac{d\mu_2}{dt} + \mu_2 N_m \frac{di_s}{dt} + \mu_2 N_b \frac{di_b}{dt} \Big] \quad (4.13)$$

$$V_b = \frac{N_b A_c}{4l}\Big[(N_m i_s - N_b i_b)\frac{d\mu_1}{dt} + N_m(\mu_1 - \mu_2)\frac{di_s}{dt} \Big] \quad (4.14)$$

For the second case (Figure 4.2 (b)), the (+) sign in (4.9) is changed by (-) and the expressions for V_m and V_b will be changed. In this case, μ_1 and μ_2 will be the same. Hence, both the main winding voltage and the auxiliary winding voltage can be expressed as in (4.15) and (4.16) respectively.

$$V_m = \frac{N_m A_c}{4l}\Big[2(N_m i_s - N_b i_b)\frac{d\mu_1}{dt} + 2N_m \mu_1 \frac{di_s}{dt} \Big] \quad (4.15)$$

As clearly, shown in (4.15), the voltage induced in main winding is dependent on both, the main winding and auxiliary winding currents. Compared to (4.12) the effect of the auxiliary winding voltage is double in this situation.

Similarly, the voltage induced in the auxiliary winding will be as a function of both the main winding and auxiliary winding parameters as illustrated in (4.16).

$$V_b = \frac{N_b A_c}{4l}\Big[2(N_m i_s - N_b i_b)\frac{d\mu_1}{dt} + 2N_m \mu_1 \frac{di_s}{dt} \Big] \quad (4.16)$$

Comparing (4.14) and (4.16) it can be revealed that, the first configuration provides less voltage induced in the auxiliary winding due to the variation in the main winding current, hence, a deeper study of this configuration is illustrated in section 4.5. After introducing the voltage expressions, it is vital to reveal the analytical principles of operation and mathematical laws, which govern its operation. The operation of the VI topology shown in Figure 4.2 (a) can be illustrated with Ampere's law. The flux intensity as a function of both the main winding and auxiliary winding parameters expressed in (4.5) and (4.6). Furthermore, the magnetic flux density as a function of magnetic field intensity and the permeability is shown in (4.7).

The total flux of a magnetic coil multiplied by the number of turns gives the flux linkage (λ).

$$\lambda = N_m \oint BdA = N_m BA \tag{4.17}$$

Replacing B in (4.17) by (4.7) the flux linkage (λ) can be written as:

$$\lambda = N_m \mu HA \tag{4.18}$$

Rewriting the magnetic flux linkage in terms of the main current and auxiliary current, the flux linkage in core 1 and core 2 can be rewritten as:

$$\lambda_1 = N_m \mu_1 A \left(\frac{N_m i_s - N_b i_b}{2l}\right) \tag{4.19}$$

$$\lambda_2 = N_m \mu_2 A \left(\frac{N_m i_s + N_b i_b}{2l}\right) \tag{4.20}$$

From the flux linkages in (4.19) and (4.20), the apparent (absolute) inductances L_1 and L_2 of each the main windings can be calculated as shown in (4.21) and (4.22).

$$L_1 = \frac{\lambda_1}{i_s} \tag{4.21}$$

$$L_2 = \frac{\lambda_2}{i_s} \tag{4.22}$$

As the two windings are electrically connected, the total apparent inductance of the main winding will be the sum of the two inductances calculated in (4.21) and (4.22).

In power converters, the differential (incremental) inductance (L_{dif}) is more important when the saturation of the material is taken into consideration as discussed in [140]. In order to estimate the differential inductance, the current should be perturbed at an operating point to compute the change of flux and finite difference approximation methods can be used to estimate the inductance of the power inductor.

$$L_{dif} = \frac{d\lambda}{di_s} = \frac{\lambda(i_s) - \lambda(i_s - \Delta i_s)}{\Delta i_s} \tag{4.23}$$

where Δi_s is a sufficiently small positive number, and i_s is the current level at which the inductance value is required to be calculated. From (4.19) to (4.23) it can be shown that both the apparent and differential inductances depend on the flux linkage, which is also a function of both the main winding and the auxiliary winding currents, the geometry of the core material and permeability.

4.4 Finite Element Modeling of Variable Inductor

In the modelling of the studied VI configuration, the 3D geometrical model is built in the MagNet Infolytica software, and the materials characteristics are defined and assigned for each component of the power inductor. The dimensions and parameters of the VI are shown in Table 4.1 and the magnetic core material used is ferrite N87 from EPCOS [141].

Table 4.1 :Specifications of the studied variable inductor prototype

Ferrite core Toroid R 102 × 65.8 × 15.0 (mm) with Epoxy coating	
Core material	N87 from EPCOS
Main winding wire gauge	4.17mm^2
Auxiliary winding gauge	0.65mm^2
Main winding number of turns	28
Auxiliary winding number of turns	360

The VI prototype, the 3D geometry and meshes, and the anhysteretic B-H characteristics curve of the studied VI prototype are shown in Figure 4.3. As it is revealed in Figure 4.3. (c) the curve is obtained by sketching the centerline of the B-H loop of the manufacturer`s datasheet. As the core materials used is gapless, the B-H curve obtained from the B-H loop is used for studying the characteristics of the device.

Following the modelling phase, the materials properties are defined, and the boundary conditions are assigned. Meshing and solver parameters are defined after performing sensitivity analysis in the results window heuristically and they are provided in the Appendix (Table 4.3).

After defining the meshes, time step and solver parameters, the model is simulated, and 3D simulation is used to solve Maxwell’s equations to determine the magnetic fields distribution, energy, linkage flux, and losses. Constant DC current in the auxiliary winding and piecewise linear current in the main winding are used as excitation currents to simulate, characterize, and analyze the VI prototype.

(a)

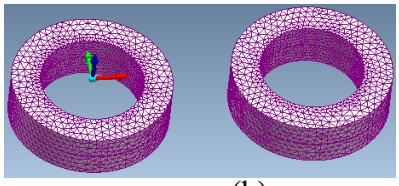

(b)

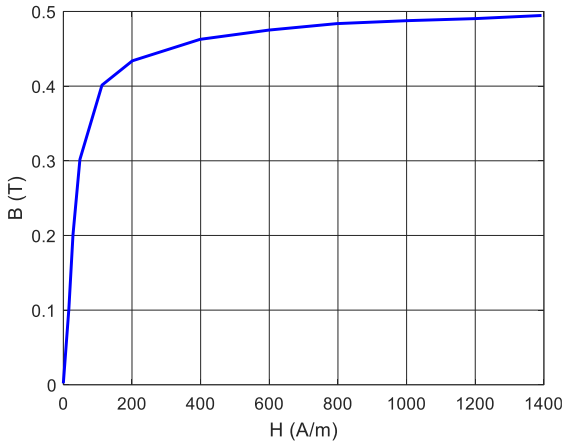

(c)

Figure 4.3: Selected Core Material (a) decoupled double core VI prototype (b) 3D Geometry and the FEM meshes of the magnetically decoupled double toroidal cores (c) the magnetization (B-H) curve of the selected magnetic core material

In the post simulation processing phase, parameters of interest such as the flux distribution, linkage flux and power losses are extracted and analyzed. Both the stored energy and linkage flux are vital quantities in order to study the variations of inductance as a function of both the main winding and auxiliary winding currents. Estimating the inductance characterization curve using the linkage flux provides better results and accuracy [142]; hence it is used in the inductance characterization of the VI prototype. Since the power inductor is forced to operate in saturation, both (4.21) and (4.22) are not suitable to estimate the inductance of the power inductor. To consider the saturation effects in the characterization of the VI, the finite difference approximation method shown in (4.23) is used to estimate the differential inductance of the power inductor.

4.5 Results and Analysis

4.5.1 Losses in the VI

In the decoupled VI prototype, the losses generated in the power inductor are the magnetic core losses and the winding losses. The calculation of the core losses is not straightforward, hence there are several empirical methods based on the Steinmetz Equation (SE) to estimate the core losses in power inductors. The classical SE method is suitable for sinusoidal waveforms [116]. Nonetheless, in power electronic converters the waveforms are non-sinusoidal hence; several methods are developed such as the modified MSE methods, [143], [144], the generalized SE (GSE) methods [143] ,[145], improved GSE (iGSE) method [146], and improved-improved GSE (IIGSE) are proposed in order to account the non-sinusoidal nature of the waveforms in power electronic converters. The detailed comparison of these methods is provided in [116].

In the estimation of the core losses, we use the modified Steinmetz's formula presented in [147]. This method is simple to use and its formulation considers the non-linearity during saturation operation. Furthermore, it is more reliable as its results can easily verified with the commercially available MagNet simulation software.

In the VI prototype, the core losses are estimated using FEA simulation. The estimation of the core losses needs the losses curve data to be inserted in the material editor in (W/kg) with respect to the peak flux variation (T) at various frequencies from the datasheet of the material. With the help of the losses data input, the core losses (the hysteresis and anomalous losses and the eddy current losses) are determined from the simulation using Steinmetz's formula presented in [147], as shown in (4.24).

$$P_{crL} = K_h f_{sw}^{\alpha} \Delta B^{\beta} + K_e (f_{sw} \Delta B)^2 \tag{4.24}$$

where P_{crL} is the power loss in W/kg, K_h, K_e, α, β are constants, f_{sw} is the switching frequency (Hz), and ΔB is the maximum change of magnetic flux density. The constants K_h, K_e, α, and β are determined by MagNet using the input data of the core material losses for different frequencies and change of magnetic flux density. ΔB is related to the current ripple and parameters of the power inductor as shown in (4.25).

$$\Delta B = \frac{L \Delta i_{spk}}{N A_c} \tag{4.25}$$

where L, N, and A_c are the inductance, the number of turns and the effective area of the magnetic core respectively.

Similarly, the winding losses, which correspond to the power losses due to the conductivity of the conductor material [147]. These losses are estimated taking into consideration of the skin effect at the operating frequency easily using the FEM simulation. Alike the magnetic core losses the winding losses are also influenced by amount of current ripple in the power inductor as shown with the help of analytical equations. Defining a current ripple factor (r) as the ratio of peak-to-peak current (Δi_{spk}) to the average inductor current (I_s) as:

$$r = \frac{\Delta i_{spk}}{I_s} \tag{4.26}$$

The rms current (I_{rms}) across the power inductor in a DC-DC converter can be expressed as:

$$I_{rms} = I_s \sqrt{1 + \frac{r^2}{12}} \tag{4.27}$$

For a winding resistance of a power inductor (R_L) which depends up on the skin and proximity effect [148], the winding losses (P_{cL}) of a power inductor is given by:

$$P_{cL} = I_{srms}^2 R_L \tag{4.28}$$

As it can be shown in the above equations, both the copper and core losses are affected by the current ripple [149]. By controlling the current ripple using the auxiliary winding current, the main winding losses can be reduced. Figure 4-4 shows the impact of the control current in the losses of the power inductor and the losses in the auxiliary winding. Two operating currents (I_s=12 A and I_s=16 A) are selected and the control current is varied to study its impact on the global losses of the power inductor. From Figure 4-4 (a) and (b), it can be revealed that by applying a control current and regulating the current ripple the main winding losses can be reduced by 6 % for 12 A and 4 % for 16 A. The losses reduced in the main winding will offset the losses that can be introduced by the auxiliary winding circuit. Hence, the VI provides the capability of the improving the core utilization keeping the performance.

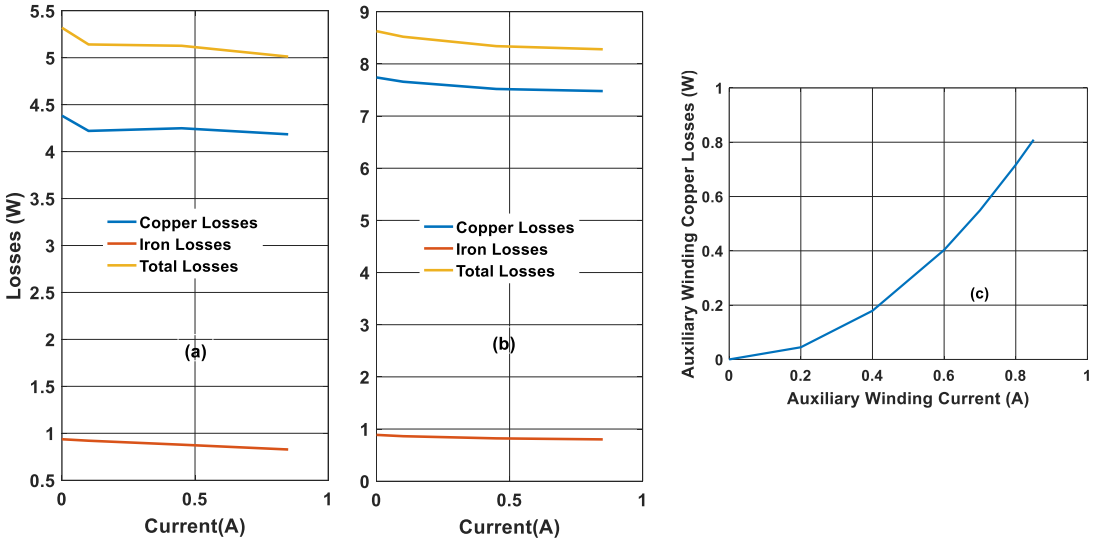

Figure 4.4: Losses as a function of the control current for both cores and considering: (a) (I_s=12 A; (b) I_s=16 A) and (c) auxiliary winding copper losses

4.5.2 Impact of voltage induced in the auxiliary winding

In order to study the impact of the voltage induced in the auxiliary winding due to current in the main winding, a typical inductor current shown in Figure 4.5 is applied to the main winding for the two-configurations shown in Figure 4.2 (a) and (b). The applied current is a typical inductor current with an average DC value of 12 A. With the excitation current applied to the main winding, the voltage induced in the auxiliary windings due to the main winding current of each configuration are shown in Figure 4.6 (a) and (b).

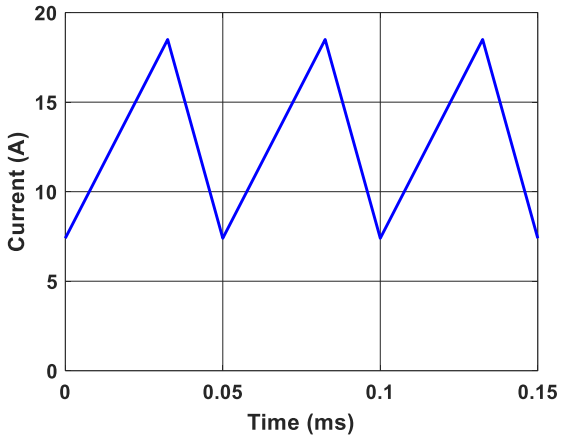

Figure 4.5: Main winding inductor current i_s

From the simulations undertaken in MagNet for the configuration shown in Figure 4.2 (a), the voltages induced in auxiliary winding of core 1 (denoted by V1) and in core 2 (denoted by V2) are nearly equal to each other but in opposing direction as revealed in Figure 4. 6 (a). Consequently, the net voltage that appears across the auxiliary winding is small. Hence, this configuration is adopted, and its detailed simulation studies are illustrated in this work. Figure 4. 6 (b) shows the voltage induced in the auxiliary winding due to the main winding current for the configuration shown in Figure 4.2 (b). In this case, the auxiliary windings are connected in such a way to cancel part of the main winding flux in respective cores. The net auxiliary winding voltage is the sum of the voltages induced in the first and second auxiliary windings. The net magnetic flux cancelation in the magnetic cores helps in delaying the saturation of the magnetic core. Nonetheless, if the net voltage induced in the auxiliary windings is high enough it may damage the auxiliary winding circuit and affect the performance of the power inductor.

To illustrate the impact of the voltage induced in the auxiliary winding because of current in the main winding, the power losses density of the two configurations is studied. The power losses density of the core and winding losses are defined as the ratio of losses to the volume of the magnetic material and the volume

of the conducting material respectively. It is expressed in W/m^3. The power losses density of the voltage addition configuration and the voltage cancelation configuration are shown in Figure 4.7 and Figure 4.8 in respective order. In each figure, the power losses density without and with a control current in the auxiliary winding are revealed in the first and the second columns respectively. Furthermore, the losses density of the average total losses, average eddy current losses and average hysteresis losses are presented in the first, second and third rows in respective order. For the two configurations, a main current (I_s) of 12 A (twice the rated current of the power inductor) is used as an excitation current, and two levels of ripple factors $r = 0.9$ for the situation of no control current in the auxiliary winding and $r = 0.4$ with a control current of (I_b) = 0.6 A in the auxiliary winding are considered. For both situations, the power losses density studies are conducted through simulations and the results are revealed in Figure 4.7 and Figure 4.8.

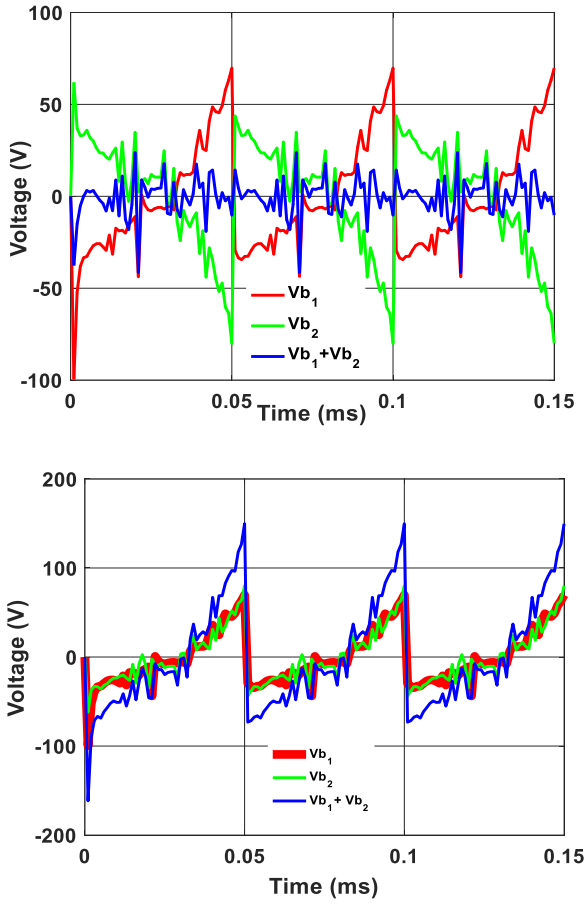

(a)

(b)

Figure 4.6: (a) Voltage reflection in auxiliary winding voltage cancellation configuration (Figure 4.2. (a)), (b) Voltage reflection in auxiliary winding voltage addition configuration (Figure 4.2. (b))

Figure 4.7 shows the power losses density (W/m^3) of the VI where the voltages in the auxiliary winding add up and flux lines produced from the auxiliary winding are cancelling part of the main winding flux in both cores. Column (i) reveals the power losses density when there is no control current applied in the auxiliary winding, whilst column (ii) provides the losses distribution with a control current of 0.6 A in the auxiliary winding. As it can be noted in the first row (Figure 4.7 (a)), the total averaged losses density is much higher when there is no control current applied in the auxiliary winding.

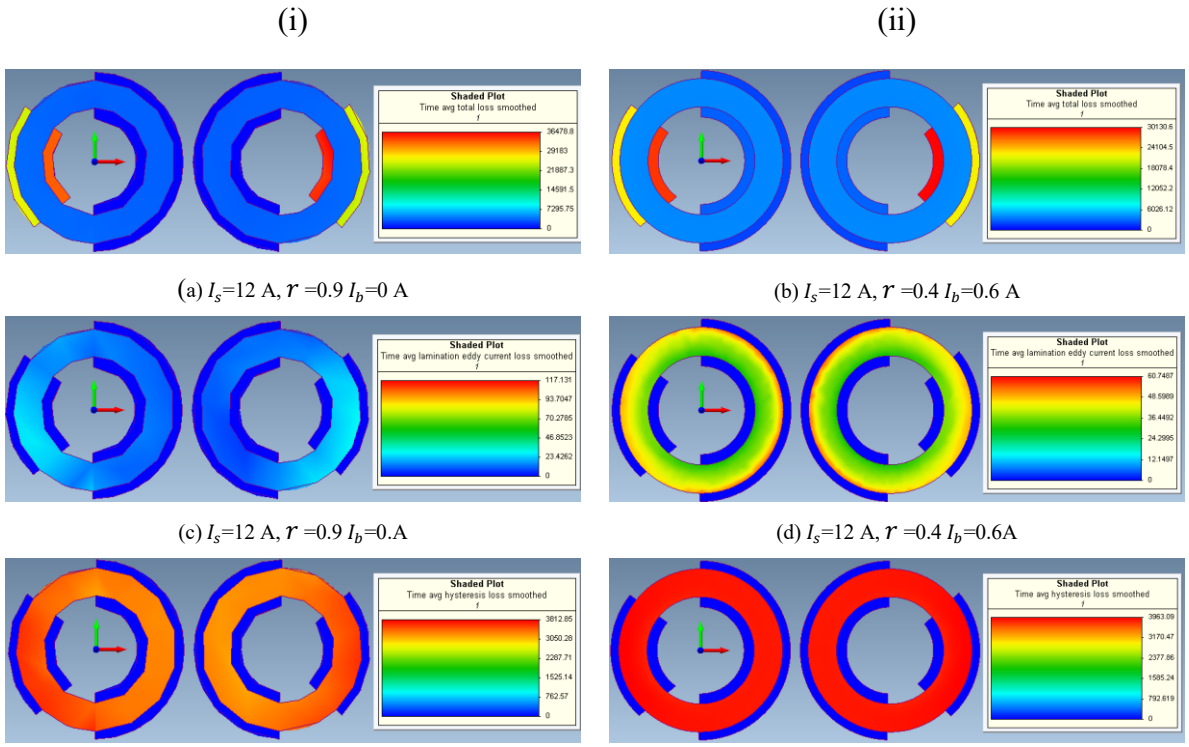

(a) I_s=12 A, r =0.9 I_b=0 A

(b) I_s=12 A, r =0.4 I_b=0.6 A

(c) I_s=12 A, r =0.9 I_b=0.A

(d) I_s=12 A, r =0.4 I_b=0.6A

(e) I_s=12 A, r =0.9 I_b=0 A

(f) I_s=12 A, r =0.4 I_b=0.6 A

Figure 4.7: Power losses density (W/m^3) for voltage addition connection of the auxiliary windings

Considering Figure 4.7 (a) and Figure 4.7 (b) the maximum total power losses density is reduced from 36478.8 W/m3 to 30130.6 W/m3 which makes the former about 17 % higher compared to the maximum total averaged losses to the condition where an auxiliary winding current of 0.6 A is applied in the auxiliary winding. This is mainly due to the reduction of the peak-to-peak current ripple in the power inductor. The higher voltage induced in the auxiliary winding due to the variation of current in the main winding in this type of configuration affects the hysteresis losses power density in the power inductor and this is clearly shown in the third row of Figure 4.7. Comparing Figure 4.7 (e) and (f) the maximum hysteresis loss density is 3812.85 W/m^3 with no auxiliary winding current and 3963.09 W/m^3 when an auxiliary winding current is

applied. In this situation, the hysteresis losses power density is higher by 4 % with a control current, mainly due to the voltage induced in the auxiliary winding due to the main winding currents.

Similarly, Figure 4.8 reveals the power losses density of the studied power inductor saturated at twice the rated current with no control current (column (i)) and with a control current of 0.6 A (column (ii)) for the situation where the magnetic core is working in partial saturation with voltage cancelation. The first row reveals the total losses density, the second shows the eddy current losses density and the hysteresis losses density are presented in the third row. Comparing Figure 4.8. (a) and (b), it can be shown that the total average losses density is smaller in the situation when a control current is applied in the auxiliary winding. Similarly, the eddy current losses density is smaller when a control current is applied in the auxiliary winding.

(i) (ii)

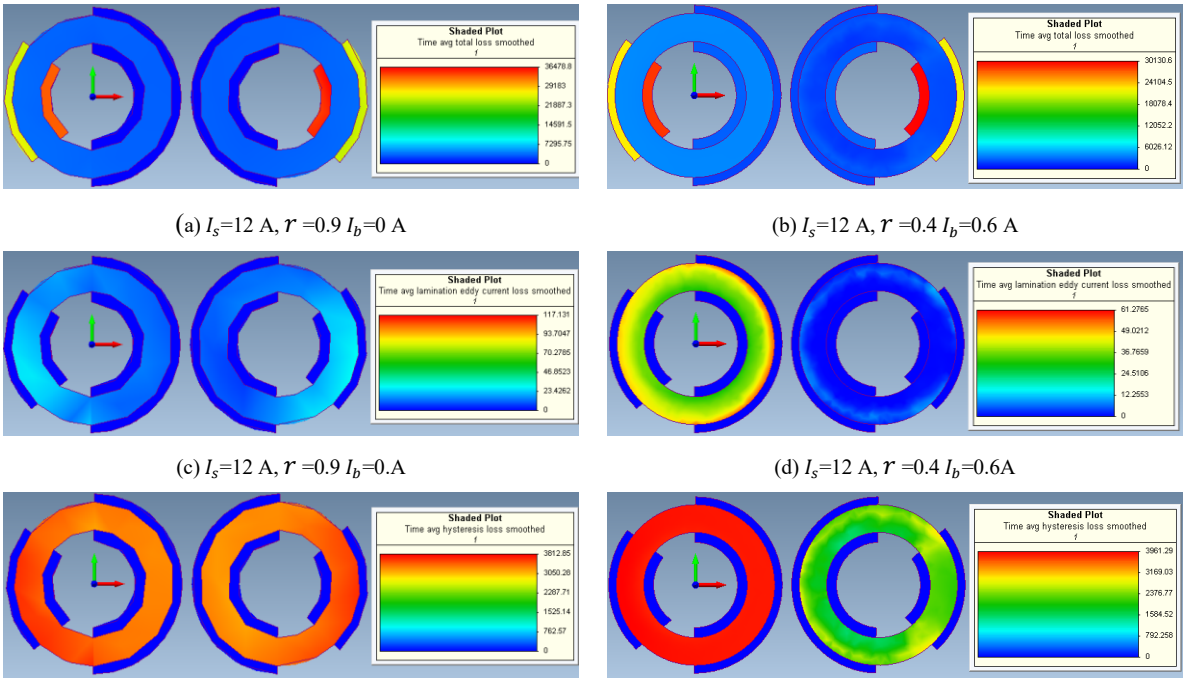

(a) I_s=12 A, r =0.9 I_b=0 A (b) I_s=12 A, r =0.4 I_b=0.6 A

(c) I_s=12 A, r =0.9 I_b=0.A (d) I_s=12 A, r =0.4 I_b=0.6A

(e) I_s=12 A, r =0.9 I_b=0 A (f) I_s=12 A, r =0.4 I_b=0.6 A

Figure 4.8: Power losses density (W/m^3) for voltage cancelation connection of the auxiliary windings

In the third row, it is indicated that the maximum of averaged hysteresis losses density is greater in one of the cores in the case where a control current is applied. Nonetheless, it is important to see the overall effect of the two cores. The loss density in the third row of the left column is the same in both cores, however, in the right one, one of the core's losses density are much smaller than the other. Considering the total effect of

the two cores, it can be deduced that the hysteresis losses density is smaller in this situation. Hence, it can be inferred that with proper control currents and partial saturation operation of the power inductor, the power losses density of the power inductor can be reduced.

Furthermore, the two situations are illustrated with the linkage flux as a function of both the main winding current and the control current are shown in Figure 4.9 (a) and (b). As it can be clearly shown in Figure 4.9 (a), one of the cores is saturated with a control current, whilst the other core's saturation can be extended to higher currents. Subsequently, the net inductance of the main winding will be the sum of the saturated core inductance and unsaturated core inductance. For the same auxiliary winding currents, by arranging the auxiliary windings in series in such a way to cancel part of the main winding flux, the saturation of both cores can be extended as shown in Figure 4.9 (b). Both linkage fluxes are identical to each other in each coil and their saturation is significantly enhanced. It should be noted that for an auxiliary winding current of 0.6 A, the magnetic cores are shown to be saturated on the opposite side of the B-H curve for small currents in the main winding.

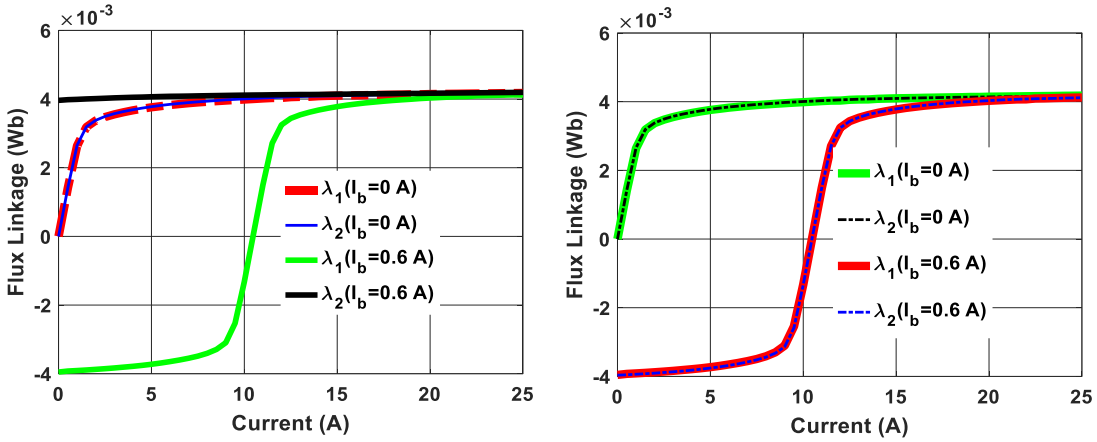

Figure 4.9 Linkage flux vs Main winding current: (a) configuration Figure 4.2 (a) and (b) configuration Figure 4.2 (b)

This is mainly due to magnitude of the magnetic flux from the auxiliary winding is much higher than that of the main winding flux and leads to the saturation of the magnetic core. This is an important finding, which mandates the selection of proper current levels for each amount of main winding currents in order to have an effective operation of this device.

The flux distribution of the two cores for the two auxiliary winding arrangements in three different conditions are shown in Figure 4.10. In Figure 4.10 (a), no auxiliary winding current is applied, as the 12 A is higher

than the rated current of the power inductor (6 A), the core is deeply saturated. For the same main winding current, when an auxiliary winding current of 0.6 A is applied (for case Figure 4.2(a) arrangement of the auxiliary windings), core 1 is unsaturated but core 2 is saturated as shown in Figure 4.10 (b). As the two main windings are electrically connected in series but magnetically decoupled the net inductance will be the sum of both inductances. On the other hand, if the auxiliary windings are connected in series (in an additive manner to each other), but in opposing direction to the main windings, the saturation of both cores is regulated as shown in Figure 4.9 (c); both cores are shown to be unsaturated.

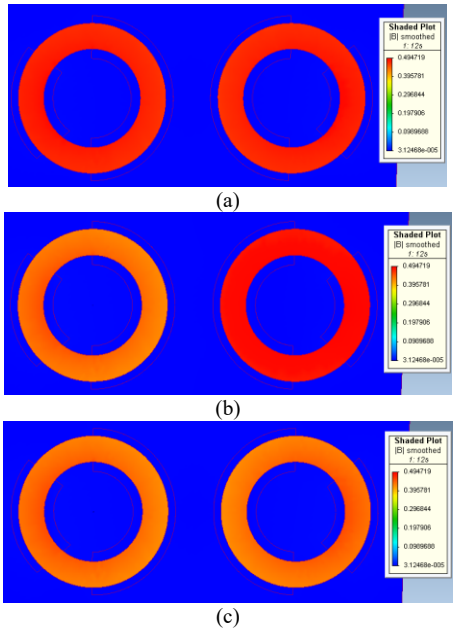

Figure 4.10: Flux distribution of studied VI (a) I_s=12 A, I_b=0 A (b) I_s=12 A, I_b=0.6 A control voltages cancelling Figure 4.2 (a); (c) I_s=12 A, I_b=0.6 A, control voltages adding Figure 4.2 (b)

4.5.3 Characterization of the Variable Inductor

In order to analyze and characterize the modelled VI topology, the linear region and the saturation region operation are studied by changing the main winding current. In addition, the inductance value of each operating point is obtained from the flux linkage simulation results using (4.23).

After studying the characteristics of the VI with no control current in the auxiliary winding, different control currents are applied. This helps to study the impact of the control current on the magnetic properties of the magnetic material. Then, the linkage flux is used for the characterization of the VI. Figure 4.11 reveals the λ-i_s curve for different control currents in the auxiliary winding. It has to be noted that the λ-i_s curves are for core 1. As core 2 is saturated due to the addition of dc flux, the λ-i_s curves of it are not included.

The λ-i_s curves are obtained by applying a ramp current in the main winding and the auxiliary winding current is varied. With the increase of current in the auxiliary winding, it can be shown that the saturation of the power inductor is delayed, i.e. the core starts to saturate at higher main winding currents as we increase the auxiliary winding current. This is mainly due to the partial cancelation of the main winding magnetic flux, which reduces the saturation effect of the magnetic core. Furthermore, it can also be shown that, if the main winding current is small, higher control currents can lead to the saturation of the magnetic core in the opposite direction. For smaller currents in the main winding smaller auxiliary winding currents are enough to cancel out the fluxes in order to enable partial saturation operation. Nonetheless, for currents much larger than the saturation current of the main winding, it is necessary that the magnetomotive force (MMF) of the auxiliary winding is sufficient to reduce part of the main MMF. Therefore, by applying appropriate auxiliary winding currents, the current handling capability of the power inductor can be regulated. The aforementioned concepts can be summarized with the differential inductance.

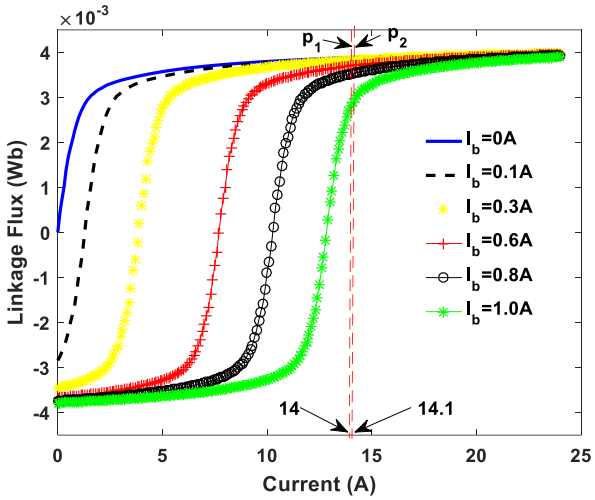

Figure 4.11: Linkage flux as a function of the main winding current for different control currents (core 1)

Considering two operating currents (14 A and 14.1 A) in each of the curves shown in Figure 4.11, the flux linkages for the selected points of operation are shown in Table 4.2. For different levels of auxiliary winding current, the differential inductance of each curve is calculated using (4.23). In the first blue curve, there is no control current applied, as a result there is very small variation in both the change of linkage flux and the differential inductance between the two selected operating points. This indicates that the magnetic core is saturated in the selected points of operation. Nonetheless, as we increase the control current, it can be shown from Table 4.2, both the change in linkage flux and the differential inductance tend to increase. In the curve with 1 A control current, the differential inductance is 56 times higher than the differential inductance of the

curve with no control current in the auxiliary winding. This is mainly due to the partial cancelation of the main winding flux that results in the enhancement of the saturation level by delaying the saturation of the magnetic core. Overall, from the last two columns of Table 4.2, it can be inferred that, this approach can be very helpful in increasing the saturation current limit of power inductors, which is very suitable for traction DC-DC converters to overcome the larger inductors demand to meet the needs of wide range of load variations.

Table 4.2 Parameters for calculating the differential inductance.

$i_b(A)$	$\lambda_{p1}(Wb)$ (i_s=14A)	$\lambda_{p2}(Wb)$ (i_s=14.1A)	$\Delta\lambda(\mu Wb)$	$L_{dif}(\mu H)$
0	0.003888	0.00389	1.42	14.2
0.1	0.00387	0.003872	2.15	21.5
0.3	0.003824	0.003827	2.59	25.9
0.6	0.003701	0.003707	5.44	54.4
0.8	0.003521	0.003532	10.12	101.2
1.0	0.00281	0.00289	79.68	796.8

In the simulations, the auxiliary winding current is applied for all levels of the main winding current in order to understand its impact on the operation of the power inductor. For small main winding currents, applying larger auxiliary winding currents could lead to the saturation of the magnetic core in the opposite direction as shown in Figure 4.11. This information could be very helpful in the development of control strategy of VI-based converters and design of the VI. In the practical implementation of this device, the auxiliary winding should be idle for currents less than the saturation current. For currents greater than the saturation current, the auxiliary winding should be activated to regulate the effective inductance of the magnetic core.

The MagNet simulation software results shown in Figure 4.12 illustrate the distribution of magnetic flux density for different main and auxiliary winding currents. The first two figures (a) and (b) show that the magnetic cores are operating in the linear region and this is clearly revealed from the flux distribution in the magnetic cores. Further increasing the main winding current leads to the saturation of the magnetic cores. For the cases of (c) and (e), as there is no control current applied, both cores are shown to be saturated. For a main current of 19 A, the magnetic cores are deeply saturated, hence, higher control current is needed in order to enable it to operate in the partial saturation mode. However, in (d) and (f) a control current is applied, and it can be shown that the first cores are operating in the linear region and the second cores are forced to operate in saturation. This leads to the partial saturation operation of the power inductor. This operation helps in reducing the voltage induced in the auxiliary winding due to the main winding current. In the linear region,

there is higher flux variation, but in the saturation region, the variation of flux is minimal due to the alignment of the magnetic dipoles in the direction of the applied field.

From Figure 4.12, it can be shown that increasing the control current can enhance the current handling capability of power inductors and delays the saturation of one of the magnetic cores. Nevertheless, higher currents in the auxiliary winding can contribute to the increase of the global losses. Therefore, the auxiliary winding should be designed to handle smaller currents and the control current needs to be kept smaller in proportion to the main winding current.

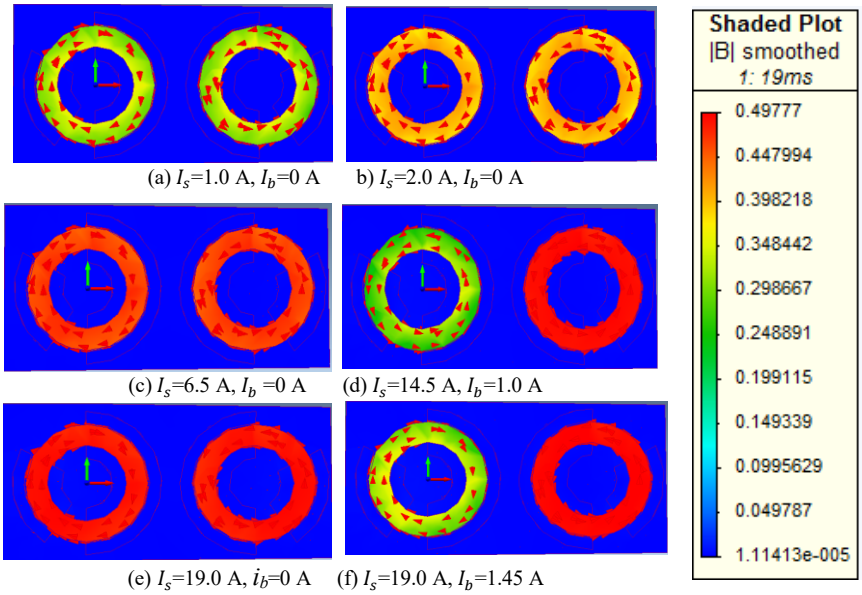

Figure 4.12: Flux distributions without and with control current in the auxiliary winding

4.5.4 Experimental Validation of the inductance characterization curve

To validate the L-i_s profile of the VI prototype, the experimental set up shown in Figure 4.13 is used. The detailed explanation of each component in the setup, the VI based converter, the variations of current ripple and enhancements in current handling capability the VI are provided in [139]. In order to obtain the L-i_s curve, the inductor current and input voltage are measured by varying the duty cycle. Using these values, the inductance of the power inductor is determined using (4.29).

$$L_{dif} = \frac{\Delta\lambda}{\Delta i_s} = \frac{DV_s}{f_{sw}\Delta i_s} \tag{4.29}$$

where D is the duty cycle, V_s is the source voltage, f_{sw} is the switching frequency (Hz) and Δi_s is the peak to peak inductor ripple current.

Similarly, the L-i_s curve of the power inductor are also estimated using (4.23) from the linkage fluxes obtained from FEM simulations for the same levels of current that are used in the experimental studies. Except at lower currents, the inductance obtained from the simulation and experimental results match to each other with a mean squared error of 1.6 %, which validates the accuracy of the FEM model of the VI prototype.

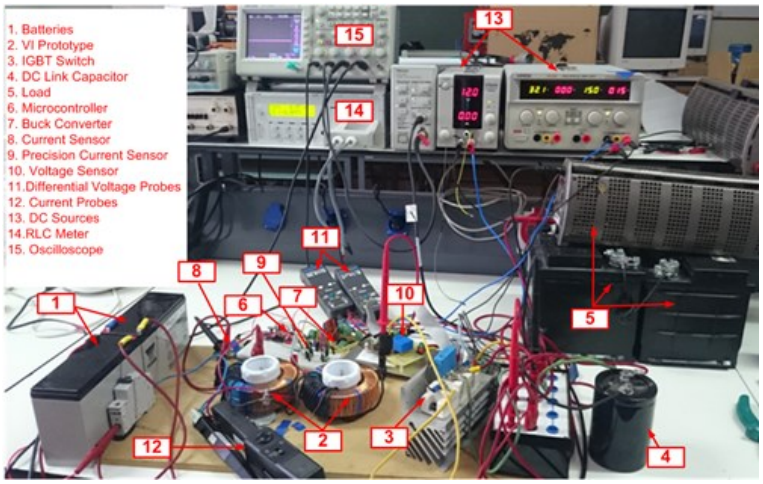

Figure 4.13 :Experimental setup of VI-based converter test bench

Finally, the inductance characterization curve as a function of main winding current of the simulated VI-prototype and the experimental studies of the same VI studied in [139] are presented in Figure 4-14. The L-i_s curve shows the typical characteristic of power inductor, the inductance is falls with the increase of the main winding current as no auxiliary winding is applied.

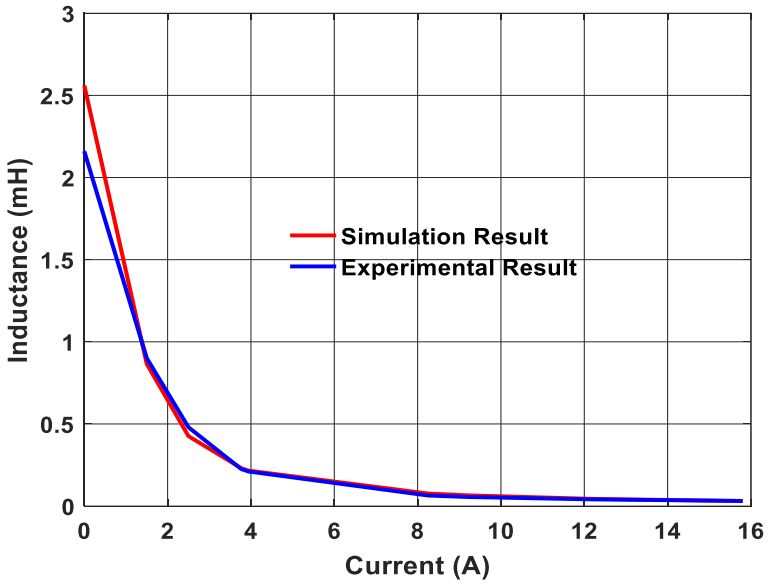

Figure 4.14 :Large signal characterization of both simulation and experimental results

4.6 Conclusion

The variable inductor (VI) uses a small DC current to regulate the effective permeability of magnetic cores and extend the saturation limit of power inductors. To investigate its suitability for applications with wide range of load variations, we have used FEM simulations to characterize and analyze a decoupled double toroidal small-scale VI prototype. The flux distribution, $\lambda - i_s$ characterization curve, the differential inductance and the power losses are studied to provide the viability of the VI for applications with wide range of power applications. From the $\lambda - i_s$ characterization curve, it can be deduced that by applying small control current in the auxiliary winding of the VI, the saturation of the magnetic core is delayed resulting in the enhancement of the current handling capability of the magnetic core. For a current of more than twice the rated current, the differential inductance is increased by 56 times with control current in the auxiliary winding. This reveals the significance of VI in improving the current handling capability and extending the saturation level of magnetic cores, thereby can help in improving the core utilization and core size reduction in power electronic converters. With the help of these results, the future trends will focus on development of control strategies for relating the auxiliary winding current as a function of the main winding current and design of the VI for traction applications. Furthermore, the $L - i_s$ curve and the $\lambda - i_s$ curves will be essential for development of analytical models that can be easily integrated in circuit simulation software for control scheme development.

4.7 Acknowledgements

This work was supported in part by Grant 950-230672 from Canada Research Chairs Program, in part by Grant RGPIN-2017-05924 from the Natural Sciences and Engineering Research Council of Canada, in part by Arbour Foundation Scholarship, and by projects UID/MULTI/00308/2019 and by the European Regional Development Fund through the COMPETE 2020 Program and FCT – Portuguese Foundation for Science and Technology within projects ESGRIDS (POCI-01-0145-FEDER-016434) and MAnAGER (POCI-01-0145-FEDER-028040).

4.8 Appendix

Table 4.3: Parameters used in the FEM simulation – MagNet software

Meshing		
Component	Maximum element size (mm)	Curvature refinement angle
Conductor	2	5
Core	2	5
Solver Options		
Material		Non linear
Max. number of newton iterations		20
Polynomial order		2
System frequency (kHz)		20
Solving method		Newton-Raphson
Newton tolerance (%)		1
CG tolerance (%)		0.01

Chapter 5 Design of Variable Inductor for Powertrain DC-DC Converter

Original Title: Design of Variable Inductor for Powertrain DC-DC Converters

Authors Affiliation:

- **Mebrahtom Woldelibanos Beraki**: PhD Student, Université de Sherbrooke, Faculté de génie, Département de génie électrique et de génie informatique
- **João P. Trovão** : Professor, Université de Sherbrooke, Faculté de génie, Département de génie électrique et de génie informatique
- **Marina S. Perdigão:** Professor, Instituto de Telecomunicações and Polytechnic Institute of Coimbra, 3030-290 Coimbra, Portugal

Date of Acceptance: April 2, 2019

State of acceptance: Published

Reference: 2019 IEEE ISIE - 28th International Symposium on Industrial Electronics (ISIE), DOI: 10.1109/ISIE.2019.8781250

Summary

Content: This article provides a design procedure of VI taking into consideration of the nature and requirements of a three-wheel recreational electric vehicle. Unlike the classical methods, the design procedure is based on the RMS current rather than the peak current. The proposed design procedure is evaluated with FEM simulations. In comparison to the peak current design, the RMS based design and the use of VI resulted in 46% volume reduction.

Results: The results reveal a significant reduction in the weight of power inductor. The proposed design procedure helps in reducing the oversizing of power inductors, resulting in reducing their size and enhancing the core utilization and is validated by FEM simulations.

Contribution to the thesis: The VI is composed of multiple windings and uses a small current to regulate the magnetic properties of the magnetic core. Its design especially for high power electrified converters is not yet addressed and it is one of the goals of this thesis. The RMS current based design approach presented in this paper is used to design a VI for a DC-DC converter for a three-wheel recreational vehicle and the results are essential for Chapter 7.

Abstract

Variable Inductor (VI) uses a small control current to modulate the permeability of a magnetic core and regulate its characteristics. This makes it suitable for applications with a stringent space limitation and a wide range of load variations. Nonetheless, this device is composed of multiple windings and several quantities can be used. Hence, its design is a demanding task and it is even much more complex in case of electric vehicles (EV) converters. This paper provides a systematic design procedure of VI taking into consideration of the nature and requirements of a three-wheel recreational electric vehicle. A VI is designed for a 33 kW nominal and 82 kW peak bidirectional DC-DC converter. Unlike the classical methods, the design procedure is based on the RMS current rather than the peak current. The designed VI is evaluated with FEM simulations. In comparison to the peak current design, the RMS based design and the use of VI resulted in 46% volume reduction.

Keywords

DC-DC converter, Design procedure, electric vehicles, sustainable transportation, variable inductor

5.1 Introduction

Electric vehicles (EVs) and Hybrid Electric Vehicles (HEVs) have a tremendous potential in reducing our dependence on fossil fuels and reducing greenhouse gas emissions [150]. In EVs and HEVs, power electronic converters are critically needed to interface energy sources and process the power. Connecting the energy storage systems directly to the inverter and using a DC-DC converter before the inverter are two commonly used configurations.

Directly connecting the energy storage systems, to the inverter makes the DC-link bus prone to a wider range of voltage variations. This result in current ripple in the energy sources such as batteries, which compromises their lifetime and affect negatively the performance of the motor. One suitable solution to address these issues and improve the performance of EV power train is to use bidirectional DC-DC converter between the energy storage systems and the DC-link as revealed in Figure 5.1. The traction path consists of energy storage system, a bidirectional DC-DC converter (green), an inverter and an electrical motor. The traction DC-DC converter enable stable DC-link regulation, enhance the main energy storage system life time, and extends the motor speed range and improve the efficiency of the electric drive [151]. The DC-DC converter should increase the overall system performance without sacrificing the size and weight of the overall system. Therefore, its components should be selected to meet this target. The power inductor is one of the heaviest and largest components, and it constitutes much of the cost, losses and volume of the bidirectional DC-DC converter [119]. This is mainly due to the size of magnetic core and number conductors. Hence, it is a critical bottleneck in the miniaturization of EV converters [120]. Subsequently, there is a continuous pursuit in reducing its size, weight and improving its power density.

Often the power inductor is selected for maximal input current, in case of boost-based converters. This design will satisfy all the operating modes of the converter. Nonetheless, the power inductor will be forced to operate in peak current levels for shorter time, thus it will be underused most of the time. This results in an overdesign of the magnetic core leading to bulky inductors resulting in larger power converters [152]. Hereby, reducing the space for energy storage systems, which limits the driving range of EVs. To address the oversizing of the inductor for EV converters and enhance its core utilization, the conventional inductor is replaced by variable inductor (VI) and an RMS current based design is adopted for its sizing. As proposed in [153], the VI uses an auxiliary winding in order to regulate the magnetic properties of the core. The proposed approach is demonstrated with a half-bridge bidirectional converter for a three-wheel sports vehicle [154].

Due to its feature of regulating the magnetic properties of magnetic cores, the VI is gaining popularity in a wide range of power electronics converters applications [155], [71]. Its modeling and analysis using PSPICE simulations is well addressed in literature [127]. Furthermore, several iterative conventional inductor design procedures are presented in [156] and [157]. Nonetheless, the design of the VI especially for high power EV converters applications is not yet addressed. As such, this paper provides the design procedures of the VI for power train DC-DC converter. Unlike the classical methods, the design procedure is based on the RMS current rather than the peak current and the magnetic properties of the core material are regulated using a small DC -current.

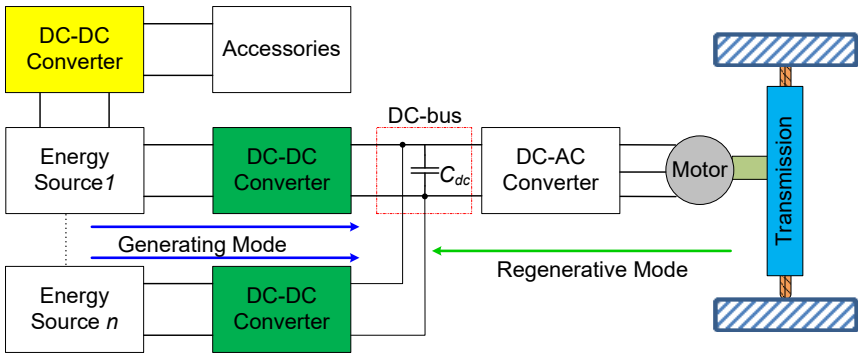

Figure 5.1: Schematic diagram of electric drive components

This paper is organized into five sections. Section 5.1 provides a brief introduction. Section 5.2 presents the detailed design procedures of the VI for a bidirectional DC-DC converter. To illustrate the design procedures and the significance of the VI, a case study of a half-bridge bidirectional DC-DC is included in section 5.3. The FEM simulation of the large-scale VI prototype is provided in section 5.4. The conclusions and the future directions are presented in the last section.

5.2 Variable Inductor Design Procedure

The design of a VI includes the selection of the magnetic core dimensions, the main and auxiliary winding number of turns and the amount of magnetomotive force to change saturation characteristics of the magnetic core. The main winding can be selected based on the conventional inductor design procedures considering the RMS current instead of the peak current. The auxiliary winding should be selected based on the level of magnetomotive force (MMF) needed to counteract the main winding flux. The proposed design procedure is composed of eight steps and the step-by-step design guidelines are presented in this section and summarized

in Figure 5.2. The area product method is used due to its simplicity and the availability of the area product from the sellers.

Step 1: Calculation of circuit parameters and inductance.

These parameters are deduced from the electrical specifications and assumptions considered for the selected converter topology. The inductance value is calculated as in (5.1).

$$L_s = \frac{V_{s\_min} D_{max} T_s}{\Delta i_s} \tag{5.1}$$

where L_s is the inductance of the power inductor, V_{s_min} is the minimum source voltage, D_{max} is the maximum duty cycle (the ratio of the on time to the switching period), T_s is the switching period, and Δi_s is the targeted current ripple.

Step 2: Main winding design**:**

It consists of 12 steps and each of them are presented below.

Step 2.1: Calculation of energy storage capacity (E_s).

The peak current is used for the calculation of the energy storage capacity requirement of power inductors customarily [158]. In case of traction applications, the power inductor is embarked with currents less than the peak current for most of its operation time. Selecting the power inductor for peak current leads to the oversizing of the power inductor [152]. Hence, the RMS current is used in the energy storage capacity calculation to address the oversizing of the component and the core current handling capability will be enhanced with the current in the auxiliary winding.

$$E_s = \frac{1}{2} L_s I_{RMS}^2 \tag{5.2}$$

where L and I_{RMS} are the inductance calculated in (5.1) and the I_{rms} is the RMS current.

Step 2.2: Selecting a type of magnetic core material.

The choice of core requires an examination of a number of variables including loss density, saturation flux density, and permeability characteristics as a function of temperature and frequency, and the mechanical strength of the material, range of frequency of operation, volume and cost. Furthermore, there are wide array

of magnetic cores to consider when selecting the magnetic material [159]. All these make the optimal choice of magnetic material intricate. For the target application, lighter weight and smaller volume are stringent requirements; therefore, materials with high saturation flux density, controllable permeability, lower losses, low cost and wider operating temperature are needed [120]. Furthermore, factors such as the material strength and its resistance to shock and vibrations must be taken into account.

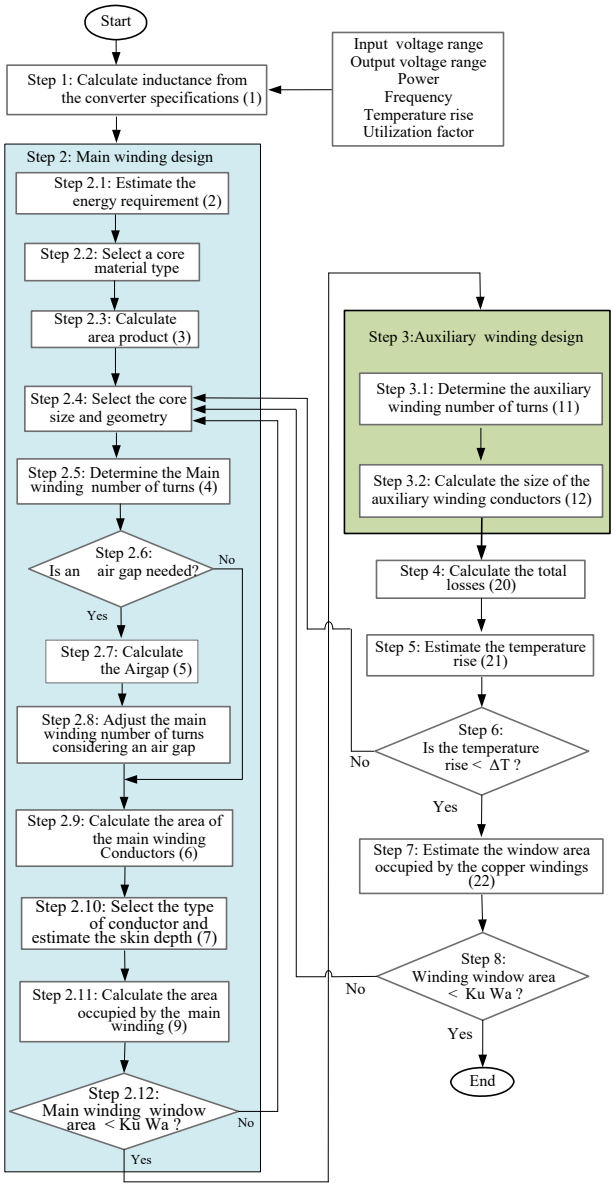

Figure 5.2: VI design procedure

Step 2.3: Calculate the desired area product (A_{pdes}).

Following the estimation of the energy that could be stored in the power inductor and the selection of the type of magnetic material, the area product is calculated by:

$$A_{pdes} = \frac{2E_s}{JB_{max}K_u} \tag{5.3}$$

where J, B_{max} and K_u are the current density, the maximum flux density and the window utilization factor in respective order. The value of current density can be chosen in the range of $2\,\mathrm{A/mm^2}$ to $5\,\mathrm{A/mm^2}$. The value of B_{max} depends upon the type of the core material selected and it should be selected to be less than the worst case saturation flux density B_{sat} of the material to ensure the safe operation of the power inductor. Usually $B_{max} = 0.8\,B_{sat}$ provides a good margin and can be a good design specification. The window utilization factor (K_u) value selection is dependent on the type of conductors used [160].

Step 2.4: Selecting the magnetic core size and geometry.

The core area must support the flux and the window area must accommodate the current. Using the calculated A_{pdes} select the smallest higher value from the area product data of magnetic core materials.

Step 2.5: Calculate the number of turns of the main power inductor (N_m). From the selected core material size and geometry, the effective area (A_c) of the magnetic core material is obtained from the datasheet of the selected material and with this information, the number of turns of the main winding can be calculated as in (5.4).

$$N_m = \frac{L_s I_{RMS}}{B_{max}A_c} \tag{5.4}$$

Step 2.6: Check the requirement of an air gap

In the cases where the inductor is needed to store high energy and core with discrete air gap such as ferrite, nanocrystalline, amorphous and silicon steel material is selected, an air gap is vital. If distributed core material is selected, no air gap is needed jump to ***Step 2.9***.

Step 2.7: The calculation of the air gap (l_g).

The air gap affects the permeability of the magnetic material leading to the change in the reluctance of the magnetic core [161]. Furthermore, its length affects losses due to leakage flux in the air gap. The length of the air gap is calculated using:

$$l_g = \frac{\mu N_m^2 A_c}{L_s} \tag{5.5}$$

Step 2.8: Recalculate the main winding number of turns taking into consideration of the air gap.

Step 2.9: Calculate copper cross-sectional area (A_{mcu}).

With the selected value of current density (J) in ***Step 2.4***, and the specified or calculated RMS current (I_{RMS}) of the power inductor, the cross-sectional area of the copper can be estimated as in (5.6).

$$A_{mcu} = \frac{I_{RMS}}{J} \tag{5.6}$$

Step 2.10: Type of conductor selection.

Depending on the switching frequency, and other specifications, a round wire, foil or litz wire can be selected. If lower losses, smaller volume are considered as a key design requirement, the litz wires and foil windings are good candidates [162]. However, if cost is the main constraint round and rectangular cores are suitable ones [162], [50]. For higher switching frequencies, it is important to consider the effect of the skin effect in this stage of the design. In such situations, the skin depth (δ) in mm can be calculated using the formula [163] and its simplified form in (5.7).

$$\delta = \frac{66.2}{\sqrt{F_{sw}}} \tag{5.7}$$

To meet the copper area calculated in (6) a number of parallel wires (N_p) should be used and the number can be obtained from (8).

$$N_p = \frac{A_{mcu}}{A_{\mathrm{AWG\#\,x}}} \tag{5.8}$$

where $A_{\mathrm{AWG\#\,x}}$ is the selected size of the conductor.

Step 2.11: Calculate the area occupied by the main winding (W_{am}). The area occupied by the main winding can be determined by multiplying the number of main winding turns and the area of the winding wire area.

$$W_{am} = A_{mcu} N_m \tag{5.9}$$

Step 2.12: Check the area occupied by the main winding conductors. The effective window area (W_{a_eff}) can be calculated as:

$$W_{a\_eff} = K_u W_a \tag{5.10}$$

where W_a is the window area of the core. If W_{am} is greater than, W_{a_eff} then go back to ***Step 2.4*** and select a larger core size. However, if the area is smaller, then proceed to ***Step 3***.

Step 3**:** Auxiliary winding design**.**

The auxiliary winding is designed in such a way to keep the magnetic core away from the saturation for currents higher than its rated values and to avoid saturation of the core.

Step 3.1: Estimate the number of turns of auxiliary winding.

The number of turns of the auxiliary winding are usually determined through numerical solutions or experimentation [15]. The auxiliary winding should be selected in order to cancel part of the main winding MMF to force the core to operate in the partial saturation operation. In doing so, the auxiliary winding number of turns should be higher than the main winding turns and its current should be much smaller than the main winding current [15]. With these considerations, a suitable value of control current can be selected and the auxiliary winding number of turns (N_b) can be estimated as:

$$N_b = \frac{N_m I_m}{I_b} \tag{5.11}$$

where N_m , I_m and I_b are the main winding number of turns, the main winding current and the auxiliary winding current respectively.

Step 3.2: Calculate the size of the auxiliary winding conductors.

The diameter of the control winding wires (d_{dc}) can also be calculated as:

$$d_{dc} = \sqrt{\frac{4I_{b_{RMS}}}{\pi J}} \tag{5.12}$$

where $I_{b_{RMS}}$ is the auxiliary winding RMS current.

Step 4: Calculate the power inductor losses.

Both copper losses (main and auxiliary windings), core and the air gap losses (if an air gap is present) should be calculated. Using the number of turns calculated in (5.4) and (5.11), the resistivity of copper and the mean length turn (MLT), the resistance of the two windings can be calculated as in (5.13) and (5.14).

$$R_{Lm} = \frac{\rho N_m MLT_m}{A_{mcu}} \tag{5.13}$$

where R_{Lm} is the resistance of the main winding and MLT_m is the mean length of a single turn of the main winding. Similarly, the auxiliary winding resistance can be calculated from auxiliary winding number of turns (N_b) and the mean length (MLT_b) of the auxiliary winding as:

$$R_{Lb} = \frac{\rho N_b MLT_b}{A_{bcu}} \tag{5.14}$$

From the calculated resistance of both windings and the currents, the copper losses of the inductor winding are calculated as:

$$P_{copper} = R_{Lm} I_{RMS}^2 + R_{Lb} I_{bRMS}^2 \tag{5.15}$$

The core losses are calculated using empirical formulas obtained from the data sheet or from empirical formulas in literature [164]. The general Steinmetz equation (SE) for calculating the core losses is shown:

$$P_{core} = K \Delta B_{max}^{x} \mathrm{F}_{sw}^{y} M_{core} \tag{5.16}$$

where M_{core} is the mass of the core material, the parameters K, x and y are parameters that can be obtained from the datasheet or fitted measurement data [165]. The value of the maximum flux swing (ΔB_{max}) in this case can be calculated using the expression shown below:

$$\Delta B_{max} = \frac{L_s \Delta I}{2 N_m A} \tag{5.17}$$

Depending on the core material used the core losses can be estimated using the empirical formulas presented in [166], [167], [168]. For the case of DC-DC converters, the Improved Steinmetz equation (ISE) which considers the flux waveform coefficient (FWC), duty cycle and SE parameters as presented in [116] can be used to estimate the core losses in the power inductor.

$$P_{core} = K_{ns} K \Delta B_{max}^{x} \mathrm{F}_{sw}^{y} M_{core} \quad (5.18)$$

where K_{ns} is the factor to consider the non-sinusoidal nature of the waveform. If an air gap is considered in the power inductor, the air gap losses can be calculated using (19) as presented in [120]:

$$P_g = K_{gp} E l_g F_{sw} K \Delta B_{max}^{x} \quad (5.19)$$

where $K_{gp} = 0.0775$ is the gap loss coefficient and $E = 0.952$ is the strip width [166] and the value of $K = 0.388$ is used for single cut C-cores with two coils [169]. After calculating the three losses (5.15), (5.18) and (5.19), the total losses in the power inductor can be calculated as:

$$P_{L\_Total} = P_{copper} + P_{core} + P_g \quad (5.20)$$

Step 5: Estimating the temperature rise of the power inductor.

The thermal specification is one of the main design considerations of a magnetic component and it is vital for the design of thermal management. From the losses calculated above, the temperature rise (ΔT) can be calculated as [166]:

$$\Delta T = 6.81 \left(\frac{P_{L\_Total}}{A_{S\_area}} \right)^{0.833} \quad (5.21)$$

where ΔT is the temperature rise, P_{L_Total} is the total power losses (W) and A_{S_area} the total surface area in (m^2).

***Step 6*:** Check the temperature rise.

If the ΔT is less than or equal to the temperature rise of the design specifications (the temperature rise is often considered in the range of 30 to 50°C [170]), the selected power inductor is a suitable choice. However, if the temperature rise is high, the design steps should be repeated from ***Step 2.4***.

Step 7: Calculate the actual window utilization factor (K_{ua}).

To verify the feasibility of the adopted design, considering the window area, (W_a) , the window utilization factor can be calculated by:

$$K_{ua} = \frac{N_m A_{cu} + N_b A_{cub}}{W_a} \tag{5.22}$$

***Step 8*:** Check the window area

If the winding window area is less than or equal to the window area, the selected core material is a good choice. If not, the process should be repeated from **Step 2.4** until the design specifications are met

5.3 Design of VI for a Bidirectional DC-DC Converter

In order to illustrate the design procedure presented in section II, a bidirectional DC-DC converter with specifications presented in Table 5.1 is considered.

Table 5.1 Specifications and calculated values

Specifications		
Parameter	Symbol	Value
Input voltage range (V)	V_s	40-85
Nominal input voltage (V)	V_{s_nom}	48
Output voltage range (V)	V_o	90-120
Nominal output voltage (V)	V_{o_nom}	96
Current ripple*	ΔI	30%
Voltage ripple	ΔV	2%
Nominal power (kW)	P_{nom}	33
Peak power (kW)	P_{max}	82
PWM switching frequency (kHz)	F_{sw}	20
Calculated Parameters		
Inductance (μH)	4.57	
DC-Link Capacitor (mF)	4.2	
Duty Cycle Range (%)	6 - 67	

* Selected within a range that minimize the inductor size and maximize the flexibility of the auxiliary winding current control.

For the application under consideration, several magnetic materials, such as ferrite, powdered core materials, amorphous and nanocrystalline can be considered. Ferrite cores are prone to saturation and operate at lower magnetic flux density, which mandates large cores, and their brittle nature limits their application for high power EV converters [171]. Powdered alloy cores has stable DC bias characteristics, better temperature stability, higher Curie temperature and they are cost effective [172]. However, they have higher core losses, and low relative permeability, which requires a greater number of turns to meet the inductance value requirement. Nanocrystalline core materials can result in smaller and efficient inductors, nonetheless, they

are expensive and they have limited shapes and sizes [173]. On the other hand, amorphous cores have smaller size, good temperature and DC bias characteristics, low core losses and high saturation flux density. The cost of such materials is also much cheaper than nanocrystalline materials and there are larger available cores, no customized design is needed for high power applications. Based on these considerations, we choose amorphous core material for the design of large-scale power inductor for the target application. Using the design procedures, the desired VI and a classical power inductor are designed, and amorphous cores are selected due to their suitability for the target application. The summary of the design results is presented in Table 5.2. From the design results, it can be shown that, the VI can be used for reducing the size of power inductors for applications with wide range of load variations. Using VI and the design procedure, the mass of the power inductor can be reduced by 46% in comparison to the classical inductor designed using the peak current.

Table 5.2 Comparison of Design Results

Parameters	Classical	VI
Energy (J)	13.503	2.177
Calculated Area Product (cm^4)	1639.360	264.265
Core Material	AMCC664	AMCC630
Saturation flux density (T)	1.56	1.56
Current density (A/mm^2)	3.3	3.3
Effective Core Area (mm^2)	2300	1430
Mass of the Core Material (kg)	10.77	7.34
Area product of the core material	1913.6	972.4
Main winding Number of Turns	4	2
Auxiliary Winding Number of turns		390
Length of Air gap (mm)	2.3	1.6
Main winding cross-sectional area (mm^2)	296	296
Auxiliary winding area (mm^2)		0.82
Total Losses	226.60	121.78
Volume of core (mm^3)	1470850	509080
Mass of core (kg)	10.77	7.34
Total volume (mm^3)	2113900.94	1193015.98
Total mass (kg)	16.519	8.903
Summary of results		
Volume reduction due to VI	44%	
Mass reduction due to VI	46%	

5.4 FEM Simulation of VI for a Bidirectional DC-DC Converter

To verify the design procedure, Amorphous (Metglas AMCC630) is simulated in MagNet infolytica software. The 3-D core model of the VI and the B-H curve of the simulated materials is revealed in Figure 5.3.

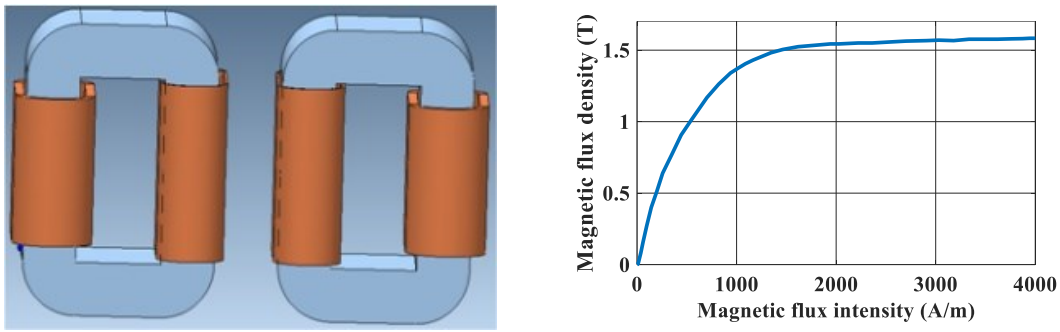

(a) (b)

Figure 5.3: (a) 3D Core model (b)B-H Curve of Amorphous Magnetic Core

The power inductor is designed for RMS current (972.22 A) and it is forced to operate up to 2.6 times the RMS value (2500 A). This current is even higher than the peak calculated current. The magnetic field density distribution of the core material for different levels of currents is revealed in Figure 5.4. With the increase of current, it is shown that, the B-field increases until the core saturates. Figure 5.4 (i) shows the case of applied current less than the saturation current (400A) and Figure 5.4 (ii) reveals the core is saturated for a current of 1600A. After applying a control current in the auxiliary winding, it can be shown in Figure 5.4. (iii) and (iv) one of the cores of the VI is forced to operate away from the saturation, leading to its operation in the in partial saturation. The partial saturation of the core changes the permeability of the core leading to the change of its inductance.

The inductance of a power inductor is affected by the relative permeability of the magnetic material, as such, the relative permeability curve both as function of the main winding current and auxiliary winding currents is revealed in Figure 5.5. The permeability of the material for different levels of current is extracted from the FEM simulations for main winding currents (I_m) ranging from 0-2500A. The blue curve reveals the relative permeability of the core when no control current is applied in the auxiliary winding and the green curve shows the relative permeability when a control current of 4A is applied in the auxiliary winding. For higher levels of main winding current, it is shown that the relative permeability can be enhanced by applying an auxiliary winding current. For a current level of 2000A, it is revealed that by applying an auxiliary winding

current of 4A, the relative permeability can be enhanced by 45%. Furthermore, in Figure 5.5, at 1500A, the percentage of permeability increase is less than 45%, but with an appropriate current in the auxiliary winding the core permeability can be kept improved to about 45%.

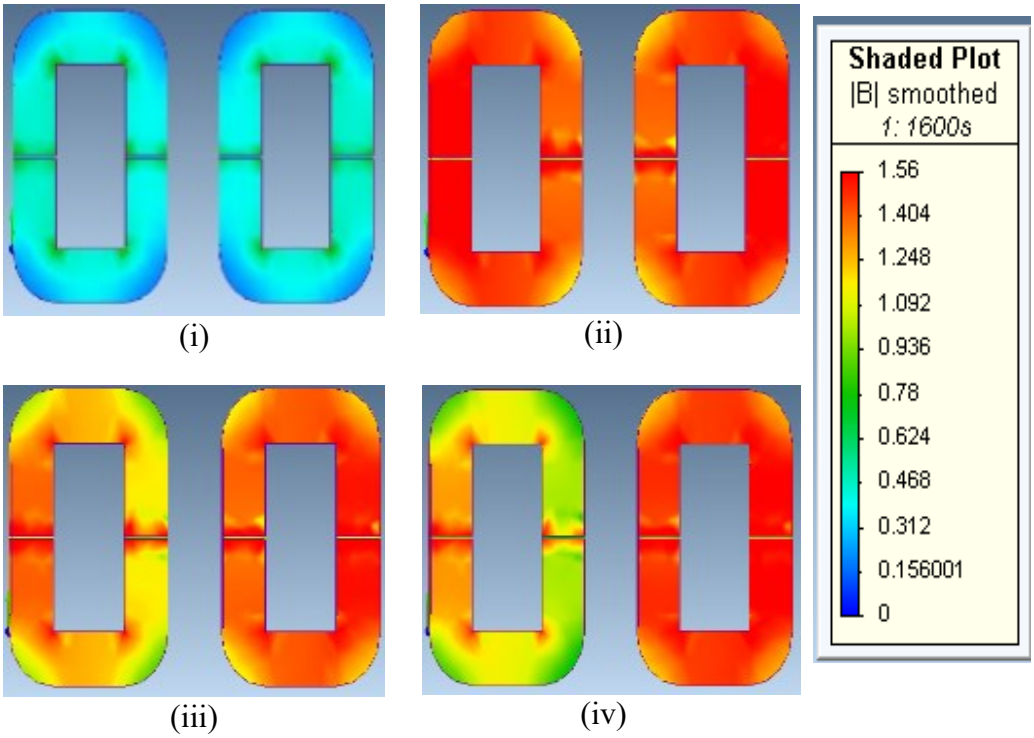

Figure 5.4: Flux density distribution (i) I_m=400A, I_b=0A; (ii) I_b=1600A, I_b=0A; (iii) I_m=1600A, I_b=2A, (v) I_m=1600 A, I_b=4A.

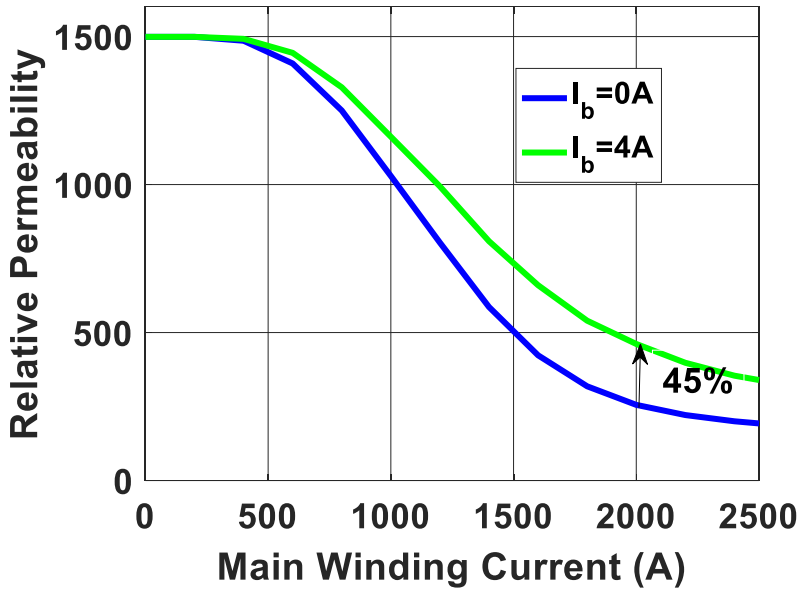

Figure 5.5: Relative permeability vs main winding current

5.5 Conclusion

This paper presents the design of VI for a half-bridge bidirectional DC-DC converter for traction application. In order to reduce the oversizing of power inductors, the RMS current is used instead of the peak current. With the proposed design procedure, it is possible to reduce the size and weight of power inductors for traction applications leading to the overall converter size reduction. The design procedure is illustrated with a VI designed for a bidirectional DC-DC converter. The design results reveal a mass reduction of 46 % when Metglas magnetic core is used. Furthermore, the FEM simulations reveal that, with help of control current in the auxiliary winding, it is possible to change the permeability leading to the change of inductance. The future directions will focus on the experimental validation of the design procedure and implementation of the VI in DC-DC converters for traction applications.

5.6 Acknowledgment

This work was supported in part by Grant 950-230672 from Canada Research Chairs Program, in part by Grant RGPIN-2017-05924 from the Natural Sciences and Engineering Research Council of Canada, in part by Arbour Foundation Scholarship, and by projects UID/MULTI/00308/2019 and by the European Regional Development Fund through the COMPETE 2020 Program and FCT – Portuguese Foundation for Science and Technology within projects ESGRIDS (POCI-01-0145-FEDER-016434) and MAnAGER (POCI-01-0145-FEDER-028040).

Chapter 6 Comprehensive Comparison and Selection of Magnetic Materials for Powertrain DC-DC Converters

Original Title: Comprehensive Comparison and Selection of Magnetic Materials for Powertrain DC-DC Converters

Authors Affiliation:

- **Mebrahtom Woldelibanos Beraki**: PhD Student, Université de Sherbrooke, Faculté de génie, Département de génie électrique et de génie informatique
- **João P. Trovão** : Professor, Université de Sherbrooke, Faculté de génie, Département de génie électrique et de génie informatique
- **Marina S. Perdigão:** Professor, Instituto de Telecomunicações and Polytechnic Institute of Coimbra, 3030-290 Coimbra, Portugal

Date of Acceptance: December 2, 2019

State of acceptance: Published

Reference: IET Electrical Systems in Transportation, DOI: 10.1049/iet-est.2019.0113

Summary

Content: In the design of power inductors, the selection of suitable magnetic core materials is a crucial step. This article provides, a systematic method for selecting suitable magnetic core materials for powertrain DC-DC converters. The weighted property method is used to systematically select and rank the suitability of magnetic core materials, and a multi-attribute decision making analytical hierarchy processes is used to calculate the relative weight of different properties. Based on the peculiar requirements of powertrain DC-DC converters, the most suitable magnetic core materials are identified and ranked with the help of the cobweb chart and the weighted property method.

Results: Using the weighted property method (WPM) and the multi-attribute decision making analytical hierarchy process, the suitability of magnetic core materials for powertrain DC-DC converters is provided. Based on performance factors, the ranking of five groups of magnetic core materials is provided.

Contribution to the thesis: Although, magnetic core materials are critical bottleneck in the miniaturization of powertrain DC-DC converters, their proper selection provides an opportunity in reducing their size and volume. The comprehensive comparison and the method provided in this article is essential for the ranking and selection of suitable materials. As one of the important steps in the design and selection of power inductors, this article is a complement of chapter 5. Furthermore, this article will be essential reference and a guide for designers and will help them to select suitable magnetic core materials at ease.

Abstract

In power powertrain DC-DC converters, the selection of suitable magnetic core materials is a critical design consideration. It ensures weight and volume reduction and performance enhancement of such types of converters. This paper provides a comprehensive comparison of magnetic core materials and a simplified cobweb chart that aids in the initial selection of magnetic core materials for powertrain DC-DC converters. The weighted property method is used to systematically select and rank the suitability of magnetic core materials, and a multi attribute decision making analytical hierarchy processes is used to calculate the relative weight of different properties. Based on the peculiar requirements of powertrain DC-DC converters, the most suitable magnetic core materials are identified and ranked with the help of the cobweb chart and the weighted property method. This paper aims at providing a quick reference for designers to ease the selection a suitable magnetic core material for powertrain DC-DC converters.

6.1 Introduction

The selection of magnetic core materials is crucial step in the design of power electronic converters. An appropriate selection of such components ensures smaller and efficient DC-DC converters. This is particularly important in powertrain DC-DC converters, as the size, weight, cost and performance of such converters is dominated by magnetic components [174], [175]. This makes the magnetic components critical bottleneck in the miniaturization of powertrain DC-DC converters. Although they are limiting factors, their proper selection provides an important opportunity in improving the performance, and reducing the size and weight of such type of converters. Figure 6.1 shows a typical schematic diagram of electric drive components. Such configuration is commonly used by automotive manufacturers [120]. The DC-DC converters highlighted in yellow are dominated by bulky magnetic components.

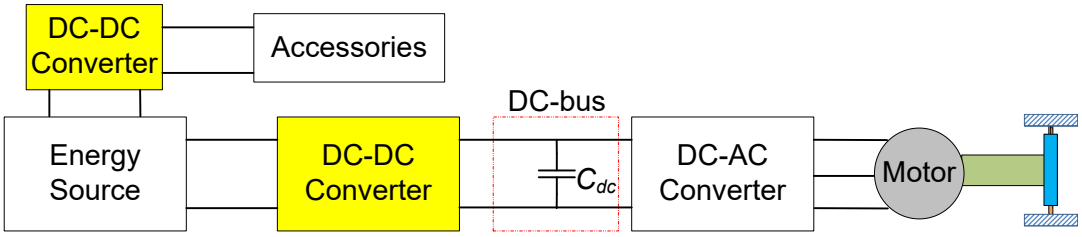

Figure 6.1: Schematic diagram of electric drive components

Some practically implemented DC-DC converters, the range of frequency of application, the range of voltages and the core material used in each converter are summarized in Table 6.1. In Table 6.1, it is shown that different magnetic core materials such as amorphous metals, alloy powdered cores, ferrite, nanocrystalline, powdered iron, soft composite magnetic (SMC) materials, and silicon steel are used in the range of 0.5-200 kHz frequencies. Furthermore, power levels ranging from 2.1kW small prototypes to 150kW are reported. The voltage levels of the energy sources lie in the range of 120-580V, whilst the DC-link voltage levels are in the range of 200-800V.

The performance of powertrain DC-DC converters is mainly decided by the type and properties of the magnetic core material. Hence, the selection of its core material and its geometry are vital [176]. For such applications, the core materials are required to have lighter weight, smaller size, lower losses, low cost, high saturation flux density, wider operating temperature, better thermal stability, low acoustic noise, higher reliability, and sound stability across a range of loads at the operating frequency [120], [176], [159], [177], [178]. Furthermore, they should have good tensile strength to withstand harsh environmental conditions, vibrations and shock in different environments [178]. To meet these different requirements, designers are

required to examine several parameters such as loss density, saturation flux density, and permeability characteristics as a function of temperature and frequency. Moreover, magnetostricition, coercivity, market availability, the mechanical strength of the material, range of frequency of operation, volume and cost are essential parameters needed to be considered [179]. All these conflicting requirements and the presence of numerous alternative magnetic core materials make the optimal choice of magnetic material intricate and a real design challenge [120], [159]. The motivation of this paper is based on the aforementioned challenge and its main objective is to provide a comprehensive comparison of the magnetic materials for powertrain DC-DC converters and to provide a systematic approach for initial selection and ranking of magnetic core materials.

Table 6-1: Sample of Powertrain Converters, Range of operation parameters and core materials used

Converter	Input range Voltage (V)	Output range Voltage (V)	Frequency (kHz)	Core material used	Power Levels (kW)
Interleaved [180]	200-450	200-700	70	Powdered core (High Flux)	50(peak)
THS-III	200	500	20	Powdered core	20
Toyota Prius THS-II	201.6	500	15	JNEX-non oriented steel sheets of iron and silicon	30
[181]	26	84	50	PC40 EC90	1
[182]	-	-	15-30	Metglas 2605SA1, 10JNHF600, Megaflux 60	2.5
[183]	-	-	170	Ferrite (3F3)	2.1
[109]	200	400	15	Ferrite and Permalloy dust	100 (Peak)
[184]	240	400	23	Ferrite (EE80 3C94)	50
[185]	200-300	400-800		Powdered iron	
[186]			10	26 kool mu E form, nanocrystalline (Finement)	15
[187]	200	400	62.5	Nanocrystalline	56
[188]	120	300	200	Ferrite (3C96) from Ferroxcube	20 (peak)
[189]	300	420	50	Nanocrystalline (foil winding)	30 (peak)
[190]	300	420	50	Amorphous core (Copper foil)	60
[191]	120-166	300-500	200		20 (peak)
[192], [193]	200-350	650-800	18-60	Nanocrystalline (Finement Ft-3M)	50
[194]			25	Nanocrystalline (Finement FT-3M, HTX-002)	150 (peak)
Interleaved [195]	200	400	500-1000	Ferrites (3F3,3F4 and N49)	50 (peak)
Composite boost converter [196]	200-300	800	20	Metglass AMCC 050	30

The comparison of several magnetic core materials is provided in [120], [186], [178], [39], [197]. The comparison of four magnetic materials namely Mega-Flux, JNEX-Core, amorphous and ferrite cores for a buck-boost inductor for HEVs is provided in [178]. The silicon steel (6.5 % Si-Fe) has been used as a core of power inductors for EV applications [185]. Nonetheless, this core material needs discrete air gap, which may affect the losses due to EMI and induction heating due to astray flux [198]. Similarly, other magnetic cores such as ferrite, amorphous alloy and nanocrystalline have the same issues. Furthermore, amorphous and nanocrystalline materials are presented as better candidates for high power coupled inductors due to low core losses and high saturation flux density [120], [199].

In literature several magnetic materials selection charts are used and some performance metrics are also reported in [200], [119]. A simplified method based on the selection matrix that considers the permeability, flux density and relative cost is presented in [201]. This selection matrix is useful in the initial screening of magnetic core materials, but it does not provide a comprehensive decision capability as it is limited to only three parameters. In [200], a material comparison chart which includes materials thermal conductivity and saturation flux density is proposed. Nonetheless, it does not consider the cost, temperature stability, and mass factor, which are essential parameters.

After the comparison of groups of magnetic core materials, this paper provides a simple cobweb graph and weighted property method for selecting and ranking the suitability of magnetic cores for powertrain DC-DC converters. Furthermore, analytical hierarchy process is used to determine the relative weighting of properties. The proposed chart considers several parameters and it can be extended further if more additional properties are desired.

This paper is organized into four sections. Section 6.1 introduces the motivation and the significance of magnetic core and its selection. The detailed comparison of magnetic core materials and available geometrical shapes are discussed in section 6.2 Section 6.3 presents the graphical tool and a systematic approach for the initial selection and ranking the suitability of alternative magnetic core materials for powertrain DC-DC converters. The conclusions and the future directions are presented in the last section.

6.2 Magnetic materials

The selection of magnetic core material is the key step in the design and selection of power inductors. There are several magnetic materials with different properties. The comparison different magnetic core materials is provided in this section.

6.2.1 Ferrite Cores

Ferrites are ceramic materials made of metal oxides. These cores have higher resistivity and lower core losses [202]. Furthermore, they have lower coercive force resulting in smaller hysteresis loses. Hence, they are suitable for high frequency applications. Furthermore, these materials have higher permeability and they do not change much with the increase of frequency between 10-100MHz [203], [204]. Ferrite cores are widely used due to their widespread availability, low cost and lower losses at higher frequencies. These core materials are suitable for applications for frequencies up to 1MHz, but with higher frequencies, the core losses increase leading to the design and selection challenge [205]. These cores exist in many different shapes and their density is smaller than other magnetic materials. Ferrite materials such as R, K, P and F with relative permeability 2300, 1500, 2500 and 3000 in respective order are suitable for power inductors used in high power applications. These materials are still popular due to their high resistivity which results in lower eddy current losses [206]. Nonetheless, they have sharp permeability roll off, low tensile strength, poor thermal stability, and low Curie temperature[207],. Furthermore, They have discrete air gap that leads to gap losses and skin effects, and lower B_{sat} that leads to bulky cores for higher power applications [208]. Hence, their suitability for high powertrain DC-DC converters is compromised [178].

6.2.2 Powdered Core Materials

Powdered magnetic core materials are distributed air gap with soft saturation characteristics. Based on their composition, manufacturing process and their characteristics they can be classified as alloyed powdered cores, powdered iron and soft magnetic composites (SMC). The details about each powdered core materials are presented in this section.

6.2.2.1 Alloy Powdered Cores

The alloy powdered cores are produced from the powder of various materials by the coagulation with an epoxy resin. They consist of small particles of pure iron and/or metal alloys, coated with a thin insulating layer and pressed at high pressure [159]. They have high $\boldsymbol{B_{sat}}$ (1-1.6T) but lower relative permeability (15 to 550) [209]. There are ample shapes and materials. The Molypermalloy (MPP), High Flux, Kool Mμ®,

XFlux®, the 75 series, and Kool Mμ® MAX are common powdered core materials. MPP provides the lowest core losses and the best temperature stability but it is the most expensive compared to other powdered core materials due to high Nickel content. High flux offers the best DC bias characteristics, with high $\boldsymbol{B_{sat}}$ and is suitable for high power applications. Kool Mμ material offers low losses and can be obtained at lower prices. In general, these magnetic cores have low relative permeability, and higher losses in comparison to ferrites, nanocrystalline and amorphous metals [120]. MPP Powder core has a better inductance independency to dc magnetization and the lowest core loss among other powder cores such as Kool-Mμ, High-Flux, and Mega-Flux. However, MPP cores have lower saturation flux density compared to the other powdered cores [210].

These magnetic materials have more stable temperature coefficient, lower flux leakage, low magnetostriction, high DC bias capability, slow roll off, increased resistivity, excellent inductance stability and lower cost [170], [172], [211], [212]. Furthermore, they have higher resistivity, low hysteresis and eddy current losses and excellent inductance stability under both DC and AC conditions. They are highly efficient for high power and small volume designs [213] and they have smaller losses compared to powdered iron and silicon steel cores. Besides, these materials have distributed air gap that results in soft saturation and reduces the flux leakage and fringing issues. Due to the aforementioned features, powdered cores are suitable for powertrain DC-DC converters. Nevertheless, their higher core losses, limit their application in very high frequency applications [209].

6.2.2.2 Iron Powdered Cores

Powdered iron cores are made nearly 100% iron. The iron particles are insulated from each other. Mixed with binder (such as phenolic or epoxy) and pressed into the final core shape. They exist in two basic materials. The Carbonyl (0-55 permeability) and Hydrogen reduced iron (up to 100 permeability). The first types of cores are useful for RF applications and the latter are useful for power applications. They have similar DC bias characteristics as alloy-powdered cores and higher core losses compared to alloy powdered cores leading to highest temperature rise. These cores can exist as Toroidal cores and E cores. These cores shapes are used to construct high power and high current inductors and filters due to their low permeability and strong stability. Powdered iron cores are the most cost effective and have an inherent distributed gap but they are prone to temperature rise problems leading to thermal aging [210], which limits their suitability for high power powertrain DC-DC converters.

6.2.2.3 Soft Magnetic Composite (SMC)

These types of core materials are made from iron particles insulated from each other by a thin organic or inorganic film [214]. The iron resin powder is flexible to be formed in different shapes. Furthermore, the insulation between iron particles increases the electrical resistivity resulting in the reduction of eddy current losses. These core materials have lower values of permeability compared to other laminated materials and they have distributed air gap hence they are suitable for power inductors. Furthermore, such magnetic materials have high power density and can be customized to desired shapes hence they are suitable for electrical motors [215]. Nonetheless, their suitability for powertrain converter is compromised due to their higher losses and weaker mechanical strength [185].

6.2.3 Amorphous Metal Cores

Amorphous metals are amorphous magnetic alloys or metallic glasses produced by rapid cooling of magnetic alloys consisting of iron (Fe), Nickel (Ni) and/or Cobalt (Co) with one or more elements such as Boron, Phosphorus, Silicon and sometimes Carbon [204]. Amorphous alloys are produced as thin ribbons mainly available as toroidal cores; U-cores and blocks cores [216]. They have high permeability, high B_{sat}, lower coercivity, high Curie temperature, high resistivity, low losses, and smaller physical size [202], [217], [209]. They are much stronger and more resistant to corrosion than nanocrystalline [218], [219]. They are also stable with soft roll off characteristic and they do not corrode in many highly corrosive environments (sea water, acids) [218]. However, these magnetic materials are expensive and their B_{sat} is affected by temperature. Furthermore, they exist in limited shapes and have limited operating temperature. Due to their reduced losses, high resistivity, high permeability, good frequency characteristics, high magnetostriction [220], high B_{sat} and smaller size, these cores are suitable for powertrain converters [219]. These types of cores offer twice thermal conductivity as ferrites [221].

6.2.4 Nanocrystalline Cores

Nanocrystalline material is a two-phase structure consisting of an ultra-fine grain phase embedded in an amorphous minority phase [216]. They are known for their high B_{sat}, high permeability, lower losses at high frequency, wide range of temperature and high Curie temperature [216], [209]. Furthermore, they have lower core losses, lower resistivity, no magnetostricition and audio noise, increased stability and durability [218]. They have high magnetization comparable to amorphous alloys and have good thermal stability [222]. Hence they are suitable for high power applications, for common mode chokes, medium-high frequency

transformers and EMI due to their smaller size, high permeability and high B_{sat} [223], [224], [225]. These types of cores can provide low volume, weight and losses. The major demerit of these types of cores are their exorbitant cost, limited shapes availability and their fragile nature [120], [226], [227]. These compromise their application in powertrain DC-DC converters.

6.2.5 Laminated Iron Alloy Cores

These types of cores are manufactured in the form of strips less than 2 mm thick stacked together to form a magnetic core [159]. These materials have the highest B_{sat}, high Curie temperature, high permeability, and they are the lowest cost cores and exist in many shapes. Nonetheless, these materials have the highest losses and they are quite inefficient at high frequency. Moreover, they have faster saturation rate. They are suitable for low frequency applications up to 20 kHz [203], [228]. They are suitable for electric machines [229], but their application to powertrain DC-DC converters is compromised by their higher losses and faster saturation rate.

6.2.6 Summary of comparison

The summary of the comparison of magnetic materials and their properties are presented in Table 6.2. The relative permeability and saturation flux density are important parameters in characterization of magnetic materials. The relationship between the relative permeability and the saturation flux density of several magnetic material is provided in Figure 6.2. As is revealed in Figure 6.2, ferrite cores have the lowest B_{sat} compared to other magnetic materials and silicon steel has the highest one. Materials with high relative permeability and high Bsat result in smaller inductors. The first allows the use of lower number of turns and the latter leads to smaller size.

Five classes of magnetic materials are presented, and several parameters are considered to provide designers a broader perspective to choose suitable magnetic materials. For each material class, a couple of magnetic cores are included as shown in Figure 6.3 and Figure 6.5. The core loss density is also an important parameter to compare different magnetic materials. A summary of the comparison of core losses density of magnetic materials is revealed in Figure 6.3. The core losses density is calculated at a switching frequency of $20kHz$ and maximum value of change of flux $0.2\ T$. Furthermore, core losses density is calculated for the range of $20kHz$ -$100kHz$, in order to observe the trends of the core materials in the specified range of frequency at the same value of flux density. The results are summarized in the last part of Table 6.2.

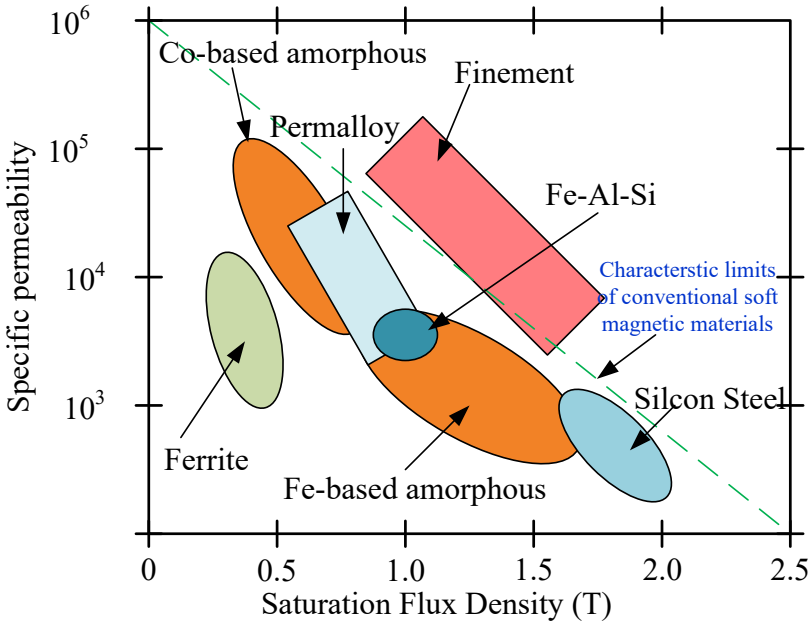

Figure 6.2: Relationship between specific permeability and saturation flux density of soft magnetic materials (adapted from [216],[230].

Silicon steel-based materials have the highest core loss density and the nanocrystalline materials have the smallest core loss density for the frequencies less than 30 kHz. Above 30 kHz, the core loss density of nanocrystalline starts to increase higher than Ferrite. This reveals that Ferrite based cores provide lower core losses at higher frequencies. Both amorphous and powdered cores have higher loss density than ferrite and nanocrystalline; nonetheless, compared to the silicon steel-based magnetic core materials these types of cores are better.

Considering different parameters, powdered core materials are superior for powertrain DC-DC converters due to their suitable DC bias characteristics, distributed air gap and high B_{sat}. Furthermore, the availability of plenty powdered core materials, shapes, sizes, slow saturation and their mechanical strength makes them the most suitable magnetic core materials for powertrain DC-DC converters. Amorphous and nanocrystalline are also good candidates with prominent features including low core losses, and smaller volume, but their cost is relatively expensive. Ferrite could be attractive at high frequency due to their lower core losses, yet their bulky size limits their application in high power and space limited applications such as powertrain DC-DC converters.

Table 6.2: Comparison of magnetic materials [120], [178], [209], [217], [220] , [226] , [231], [232], [233], [234], [235], [236], [237], [238], [239]

Magnetic Material Class	Ferrites	Alloy Powdered Core	Amorphous Metals	Nanocrystalline	Silicon Steel
Materials	3C92, 3C93, 3C94, 3C95, 3C96, 3C97	MPP, High Flux, Sendust, Megaflux,	26005SA1, 26005S3A, 2714A, Metglas® Magnetic Alloy 2605S3A	Vitroperm500F, Finement FT-3M, Finement® F3CC, Finement® F3BC Series, Block Core, Nanoperm	Permalloy, Supermalloy,10JNHF600,10JNEX900, 20JNHF1300 Silicon iron alloys, nickel iron alloys
Bsat (T)	0.25-0.53	0.5-1.6	0.57-1.56	1-1.25	0.82-2
Relative permeability	750-20000	4-550	10000-150000	500-100000	2000-35000
Curie temperature (℃)	220-300	450-770	225-415	570-600	460-750
Operating temperature (℃)	120-140	-55-200	90-150	-50-150	150
Density (g/cm^3)	4.6-4.8	6.8-8.2	7.18-7.7	7.2-7.3	7.49-8.76
Air gap type	Discrete	Distributed	Discrete	Discrete	Discrete
Relative cost	Cost-effective	Expensive	More expensive	Most expensive	Cheap
Core losses	Low	Moderate	Lower	Lowest	Highest
DC bias characteristics	Poor	Best	Better	Good	Good
Temperature stability	Poor	Best	Good	Better	Good
Magnetostriction (ppm)	0 - 1	near zero	20-40	0.1	0.1
Resistivity (μΩ-m)	5 x10^6	104	1-1.40	0.8-1.3	0.60-0.8
Frequency range (kHz)	10-5000	1000	300	100	1-20
Coercivity Force (A/m)	8	0.6-4	2.4-4	0.8-1.2	40
Mechanical strength	Very brittle	Good	Strong	Brittle	Good
Availability of shapes	Many	Many	Limited	Limited	Many
Manufacturers	Ferroxcube, Magnetics, TDK, FDK, Fair-Rite, National, Magnetics	Micrometals, Magnetics, Chang Sung Corp,Arnold Magnttics Ferroxcube	Hitachi metals, Metglass,Toshiba,AMOBEADS® SPIKE KILLER® FINEMET®	Vacuumschelze GmbH,Hitachi metals, IMPHY Metglass, Toshiba AMOBEADS® SPIKE KILLER® FINEMET®	JFE
Calculated core losses density (mW/cm3) for sample materials					
Frequency (kHz)	3C92	Kool Mu 60	C-core	Finemet FT-3H	10JNHF600
10	12.435	64.194	72.098	5.311	197.494
20	31.047	164.776	205.341	22.769	554.738
30	53.022	286.008	378.769	53.350	1014.995
40	77.513	422.955	584.832	97.612	1558.198
50	104.063	572.917	819.154	155.960	2172.795
60	132.378	734.139	1078.771	228.714	2851.010
70	162.251	905.370	1361.504	316.142	3587.149
80	193.524	1085.664	1665.662	418.470	4376.808
90	226.077	1274.274	1989.881	535.902	5216.446
100	259.811	1470.594	2333.033	668.615	6103.141

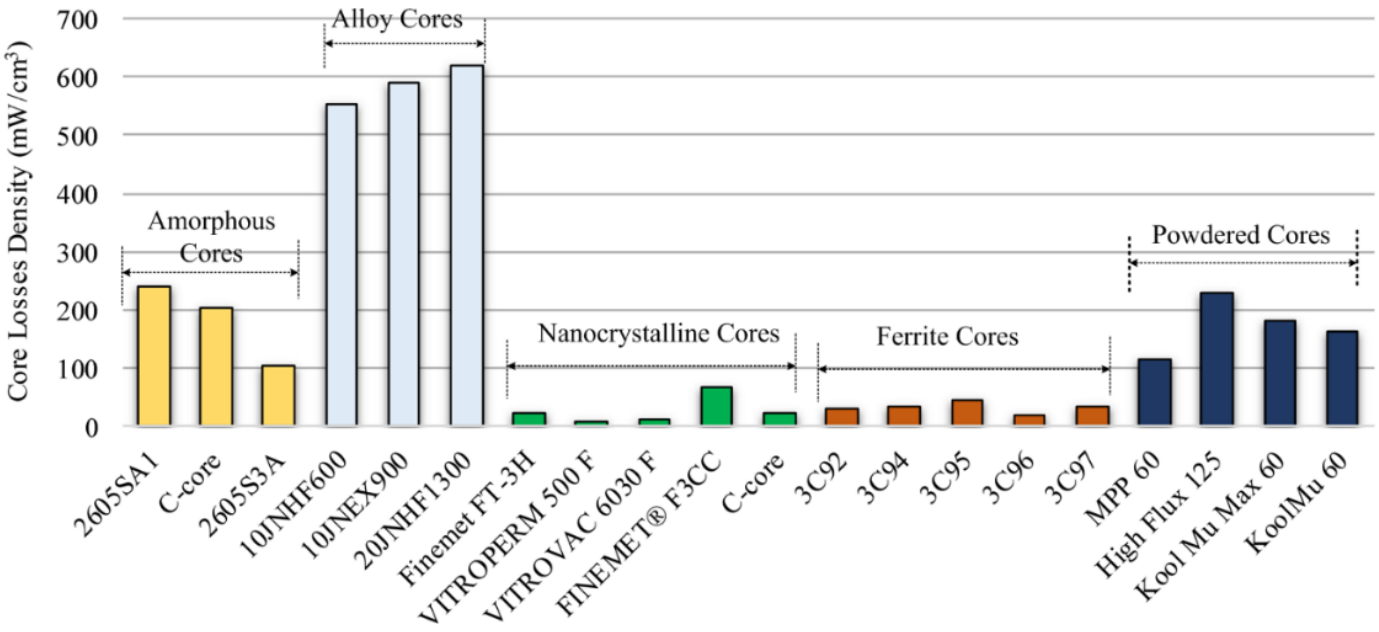

Figure 6.3: Core losses density comparison of magnetic core materials

6.2.7 Core Shapes

The core shape and geometry affect the performance of power inductors. There are variety of magnetic core shapes and sizes. A designer can choose a suitable geometric shape to meet the requirements of the target application. Several shapes are studied and their comparison presenting the merits and demerits of each and their suitability are presented in Table 6.3.

Table 6.3: Comparison of magnetic cores shapes [240], [172],[241] , [242], [243], [244].

Shapes	Features
Toroid	The magnetic flux is contained inside the core Cheaper due to a cut down in bobbin cost and can exist in many sizes No need for shielding and reduced leakage flux problem Excellent DC bias characteristics, good temperature stability and small magnetostricition coefficient Suitable for high current power inductor They produce minimal external fields, external losses and electromagnetic interference problems [244]. Suitable for high power density converters. Winding is fairly demanding and has poor ventilation.
C	Small component size and easy to wind coils Low losses at high frequency They have sharp corners, which can cut winding insulations when large conductors are placed. This may lead to failure.
E-E	Cheap, easy to building and simple bobbin structure. The most popular cores in power circuits and exist in many sizes Usually gapped to avoid saturation, have good temperature stability and low core loss at high frequency More Stray flux and severe EMI problems
EER	Good temperature stability and Excellent DC bias characteristics No magnetic flux leakage Large energy storage capacity and suitable for high current inductors
E-I	Usually gapped to avoid saturation They are less expensive than pot cores Cheap, easy to build and simple bobbin structure
EQ	No magnetic flux leakage Excellent DC bias characteristics and good temperature stability Smaller dimensions for large currents Large energy storage capacity Suitable for small dimension DC-DC converters
ER	No magnetic flux leakage Excellent DC bias characteristics, Good temperature stability Large energy storage capacity Suitable for small dimension DC-DC converters
EC	Similar to E but the centre core is round Have higher effective area which is suitable for high power applications Easy to wind and are compact
ETD	Similar to E but the centre core is round Have higher effective area which is suitable for high power applications
Pot Core	Better shielding and reduced flux noise compared to E-E and E-I. Easier to manufacture than the toroid Suitable for low power applications More expensive than E-E and E-I Poor ventilation and EMI problems
PQ cores	Mainly for high power application Compared to other cores having similar sizes and shapes, they have the largest windows areas Heat dissipation is fairly good
U	Large energy storage capacity Good temperature stability and no magnetic flux leakage Low core loss at high frequencies Sharp corners may cut winding insulation
Washer	Low core loss at high frequencies leading to high efficiency and minimum magnetic flux leakage Excellent DC bias characteristics, temperature stability and large energy storage capacity Suitable for low power applications

6.3 Selection of magnetic cores

6.3.1 Cobweb chart

After presenting the comparison of magnetic materials, a simple cobweb chart (Figure 6.3) that can be used for the selection of magnetic core materials is explained in this section. To make it a more comprehensive selection tool, several parameters such as the permeability, flux density, frequency of operation, DC bias characteristics, operating temperature, Curie temperature, relative cost and shape availability are considered. In addition, the mass factor and core losses density are calculated using representative materials and they are included with the other parameters in the cobweb chart. The energy storage capability of a magnetic core can be calculated from the geometry of the core as well as the magnetic material properties.

$$E_s = \frac{A_c\, l_c B_{max}^2}{2\mu} \tag{6.1}$$

where A_c, l_c, B_{max} and μ are the cross sectional area of the core, the effective mean length of the core, the maximum flux density and the permeability of the magnetic material respectively. The term $A_c l_c$ is the volume of the magnetic core. The volume of a magnetic core is proportional to the amount of energy that it can store, and it can be expressed as in (6.2).

$$V_{core} = \frac{2\mu E_s}{B_{max}^2} \tag{6.2}$$

In (2) it is shown that the volume of the magnetic core is proportional to core material permeability (μ) but inversely proportional to the square of B_{max}. Hence, high B_{sat} magnetic materials are suitable for smaller volume inductors. The energy can be determined from the current specification and value of the inductor. The values of B_{max} and μ are unknown parameters, which can be obtained from the datasheet of the selected magnetic material.

The mass of the magnetic core material can be expressed as the product of its volume and its density (ρ), mathematically:

$$Mass = \frac{2\rho\mu E_s}{B_{max}^2} \tag{6.3}$$

From (6-3) the mass factor (γ) can be defined as:

$$\gamma = \frac{2\mu\rho}{B_{max}^2} \tag{6.4}$$

Depending on the core material used the core losses can be estimated using the empirical formulas presented in [166], [167],[245]. The core losses density is another factor that can be used for comparisons of magnetic materials. The core losses density is often expressed using Steinmetz equation (SE). In case of DC-DC converters, the modified Steinmetz formula, which introduces flux waveform coefficient, duty cycle and the SE parameters is used to estimate the core losses [120], [167], [116].

$$P_{core} = K_{ns} K \Delta B_{max}^{x} F_{sw}^{y} M_{core} \tag{6.5}$$

The parameters K, x and y can be obtained from the datasheet or curve fitted measurement data and K_{ns} is the factor to consider the non-sinusoidal nature of the waveform. The maximum value of change of flux (ΔB_{max}) can be expressed as the function of the input voltage of the converter (V_s), the duty cycle (D), the number of turns (N) of the power inductor, the effective cross sectional area (A) of the core and the switching frequency as shown in (6.6) [246].

$$\Delta B_{max} = \frac{V_s D}{2NAf_{sw}} \tag{6.6}$$

The cobweb graph can be used as a simplified initial guide for picking a suitable magnetic material for specific application. Furthermore, it can be used as a comparison tool for methods used for ranking the suitability of magnetic materials. The parameters displayed are in per unit considering the highest parameter in each category. For instance, considering the permeability axis, the magnetic material with the highest permeability is used to normalize the other materials as shown in Table 6.4. Similarly, the same procedure is followed for other properties in the cobweb chart.

The materials and parameters that are used for the per unit conversion are presented in Table 6.4 and more details are included in Appendix.

Table 6.4: Materials and values used for normalization of the values in the cobweb graph

Parameter	Material with the highest parameter	Normalizing Value
Flux density	Silicon steel	2 T
Frequency	Ferrite	5000000 Hz
Permeability	Amorphous Metals	0.1885 H/m
Mass factor	Ferrite	128.84 s^2/m^2
DC bias characteristics	Powdered core	Best
Operating temperature	Powdered core	200^0C
Curie temperature	Powdered core	770^0C
Cost	Nanocrystalline	Very expensive
Core losses density	Silicon steel	$554.74mW/mm^3$
Availability of shapes	Ferrite	Ample shapes

The parameters such as DC bias characteristics, temperature stability, relative cost, shapes availability, and mechanical strength are illustrated with qualitative information in the comparison Table 6.2. In such situations, the Linkert scale is used to converter them into numerical values [247]. Both the 5-point (1 for the worst and 5 for the best) and 4-point (1 for the worst and 4 for the best) scales are used depending on the levels of comparison considered in the parameter. Then these values are normalized by the highest values in each scale and the results are presented in the range of 0-1in the cobweb chart.

Figure 6.3 reveals the normalized values of different parameters and properties of magnetic core materials. This cobweb chart can be used to select a suitable magnetic material by evaluating the parameters of interest under consideration. Furthermore, if more parameters are needed, it can be extended.

A quick initial selection of suitable materials can achieve from the cobweb chart. For powertrain DC-DC converters to meet the aforementioned requirements, silicon steel cores will provide smaller size inductors, but they are the loosest. Nanocrystalline cores provide smallest losses leading to efficient inductors, but they are expensive and their mechanical strength is weaker compared to powdered cores, silicon steel and amorphous cores. Similarly, ferrite cores have

smaller losses compared to powdered cores, amorphous and silicon steel, nonetheless, their size is much larger as shown in the mass factor axis. From the visual comparison of different properties in the cobweb graph, the powdered cores provide a better compromise compared to the other core materials.

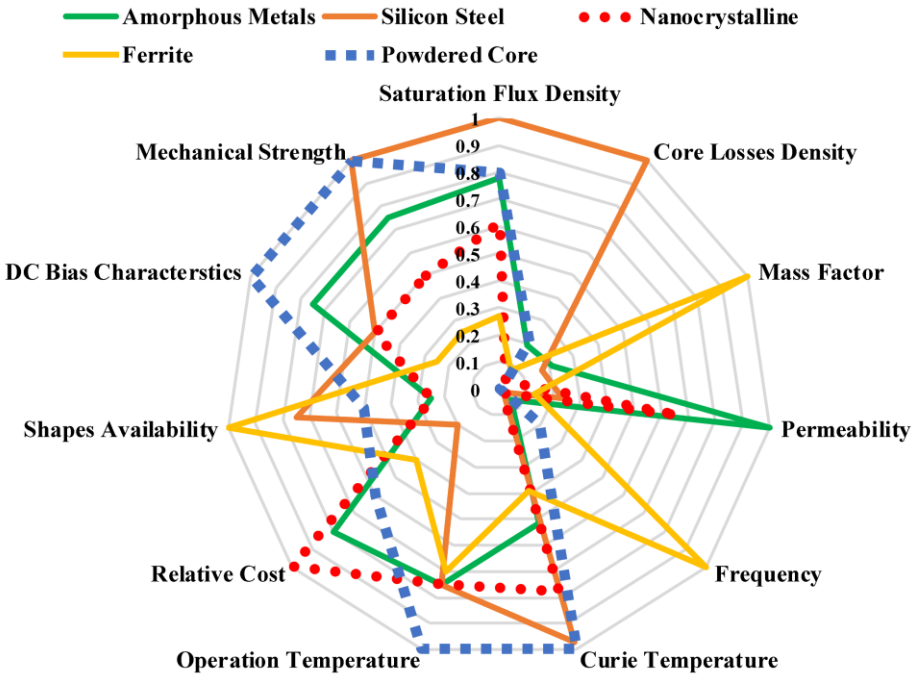

Figure 6.4 Comparison of magnetic core materials using cobweb chart

Magnetic cores for powertrain DC-DC converters, require multiple functional requirements. To deal with this, we use the weighted property method (WPM) [248] to rank the suitability of the magnetic core materials. The normalized parameters in the cobweb chart are used as the scaling factors based on their importance. For the properties such as DC bias characteristics and *Bsat*, where high (maximum) value is important, the scaling factor can be estimated as in (6.7).

$$\beta = \frac{Numerical\ value\ of\ property}{Maximum\ value\ in\ the\ \ graph} * 100 \tag{6.7}$$

Similarly, the properties such as mass factor, losses density and relative cost, where low values are desired, the scaling factor are estimated as in (6.8).

$$\beta = \frac{Lowest\ value\ in\ the\ \ graph}{Numerical\ value\ of\ property} * 100 \tag{6.8}$$

In powertrain DC-DC converters, the size, efficiency, mechanical strength and ability to work over a wide temperature range and cost are paramount requirements. To meet these, it is vital to assign the relative weight of parameters and properties to rank the suitability of magnetic core materials using the WPM. To this end, a multi attribute decision making analytical hierarchy process (AHP) [249] is used to calculate the weighting factor of the considered parameters. Nine selected properties are rated in a pairwise comparison and their relative weight is calculated accordingly as shown in Table 6.5.

Table 6-5: Parameters and Weighting Factors

Parameter	Weighting factor (α_i)
Saturation Flux Density	9.06
Core Losses Density	12.61
Frequency	11.25
Permeability	9.81
Operation Temperature	12.97
Relative Cost	13.66
Shapes Availability	8.31
DC Bias Characteristics	10.06
Mechanical Strength	12.27
Total	100.00

In the AHP method the coherence and consistency of the pair wise comparison and the relative weighing factors is verified by the consistency ratio (CR). CR ratios less than 10% reveal the consistency of the judgments is acceptable, otherwise, the pairwise comparisons should be improved further [250]. After the determination of the weighting factors, the CR is calculated, and it is found to be 7.86%. Hence, the pairwise comparison and the relative weights are coherent and can be used to determine the performance index of the selected properties to rank the suitability of the alternative magnetic core materials for the desired target application. The properties such as cost, temperature range of operation, mechanical strength and losses density are assigned higher relative weights revealing their critical importance for the target application.

The performance index is calculated as in (6.9):

$$\gamma = \sum_{i=1}^{n} \beta_i \, \alpha_i \tag{6.9}$$

where i is summed over all the relevant properties.

The performance index of the magnetic cores is determined and the results for each class of magnetic cores for the considered magnetic core material are shown in Table 6.6. The alternative with highest performance index is considered the most suitable, accordingly the rank is given to each alternative material as shown in Table 6.6. As shown in Table 6.6, powdered core materials are deemed to be the most suitable for target application followed by amorphous, nanocrystalline, silicon steel and ferrite core materials respectively.

Table 6.6: Performance index and ranking of candidate materials

Materials	Performance Index	Ranking
Amorphous Metals	54.02	2
Ferrite	50.00	5
Nanocrystalline	53.35	3
Powdered Core	58.22	1
Silicon Steel	52.49	4

6.3.2 Case Study

To demonstrate the proposed method for the selection of suitable magnetic cores, the area of product of different magnetic core materials is used for a boost inductor with specifications shown in Table 6.7.

The area product relates both the electrical and magnetic parameters with the core geometry and size [152]. Furthermore, volume and weight of the core of the magnetic materials are related to the area product [251]. Hence, we use this parameter to compare the different magnetic cores from each category of magnetic material presented in the cobweb graph. The area product of a magnetic core is estimated as in (6.10).

$$A_{pdes} = \frac{2E_s}{JB_{max}K_u} \tag{6.10}$$

where E_s, J, B_{max} and K_u are the energy storage capacity of the power inductor, the current density, the maximum flux density and the window utilization factor respectively. Assuming $J = 3.3\,\mathrm{A/mm^2}$, and $K_u = 0.4$ the same for all the materials under consideration, and $B_{max} = 0.8\,B_{sat}$ for each material, the area product of each core material is calculated. In order to have a fair comparison we normalize the area product each magnetic core material with the minimum area product obtained for 15JNHF950 ($1278.7\ \mathrm{cm^4}$) and the resulting comparison are shown in Figure 6-5. As shown in Figure 6-4, alloy cores provide smaller core inductors due to their high *Bsat* followed by powdered cores, amorphous, nanocrystalline and ferrite cores. Ferrite cores will be about more than three times bigger compared to alloyed cores and about twice larger compared to powdered and amorphous cores. Nanocrystalline cores are about half smaller than ferrite cores. Compared to the loss density in Figure 6.3, alloyed cores have higher losses in comparison to other magnetic cores, hence they will compromise the high efficiency requirement of powertrain DC-DC converters.

Table 6.7: Specifications of the Case Converter

Parameter	Symbol	Value
Input voltage range (V)	V_s	40-85
Nominal input voltage (V)	V_{s_nom}	48
Output voltage range (V)	V_o	90-120
Nominal output voltage (V)	V_{o_nom}	96
Current ripple	ΔI	30%
Voltage ripple	ΔV	2%
Nominal power (kW)	P_{nom}	33
Peak power (kW)	P_{max}	82
Switching frequency (kHz)	F_{sw}	20
Inductance (μH)	4.57	
DC-Link Capacitor (mF)	4.2	
Duty Cycle Range (%)	6 - 67	
Energy in the inductor (J)	13.50	

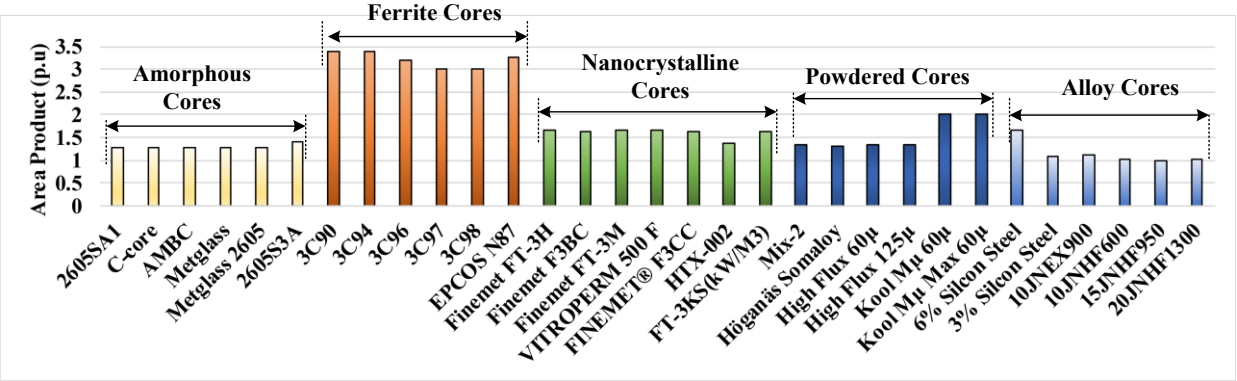

Figure 6.5: Normalized area product comparison of magnetic core materials

6.4 Conclusion

This paper presents the comprehensive comparison and selection of magnetic core materials for power train DC-DC converters. The application requires multiple functional requirements, hence selection and ranking of the suitability of available magnetic core materials is essential. To this end, we use the cobweb graph and the weighted property method to select and rank the suitability of different magnetic core materials. The cobweb chart is useful for the initial selection suitable candidates based on the compromise of the desired properties of the target application. For considered application, smaller mass, low losses, good DC bias characteristics, thermal stability, high power density and cost are critical design requirements. To meet these requirements, powdered core materials, amorphous, nanocrystalline, ferrites and silicon steel cores are compared. Accordingly, their suitability is ranked based on the performance index obtained from the weighted property method for the relative weighting factors determined using the AHP approach. Considering nine properties, the powdered cores are ranked as the most suitable materials due to their high *Bsat*, better thermal stability, stable DC bias characteristics and their mechanical strength. Both amorphous and nanocrystalline have high *Bsat*, and good temperature and DC bias characteristics. Hence, could result in smaller and efficient inductors, but their cost is much higher than powdered cores. Hence, they are ranked next to powdered core materials. The proposed cobweb chart and the presented approach can be a vital tool for optimal design process of magnetic

core materials for powertrain DC-DC converters in particular and power electronic converters in general.

6.5 Acknowledgment

This work was supported in part by Grant 950-230672 from Canada Research Chairs Program, in part by Grant RGPIN-2017-05924 from the Natural Sciences and Engineering Research Council of Canada, in part by Arbour Foundation Scholarship, and by projects UID/MULTI/00308/2019 and by the European Regional Development Fund through the COMPETE 2020 Program and FCT – Portuguese Foundation for Science and Technology within projects ESGRIDS (POCI-01-0145-FEDER-016434) and MAnAGER (POCI-01-0145-FEDER-028040).

6.6 Appendix

In order to have a common axis value, the parameters are expressed in per unit values. The parameters in the cobweb chart are scaled by the maximum value of the material with the highest parameter in the specific property. The properties of the materials presented in the chart are flux density, frequency permeability, mass factor, DC bias characteristics, operating temperature, Curie temperature, cost, core losses density and availability of shapes. For each axis shown in the chart. The per unit conversion of some of the parameters is performed as in Table 6.8.

Table 6.8: Per unit Conversion of Parameters

Parameter	Formula
Flux density	$\frac{Bsat\ \ of\ the\ magnetic\ material}{2\ T}$
Frequency	$\frac{Frequency\ of\ the\ magnetic\ material}{5000000\ Hz}$
Permeability	$\frac{Permeability\ \ of\ the\ magnetic\ material}{0.1885\ \ H/m}$
Mass factor	$\frac{Mass\ factor\ of\ the\ magnetic\ material}{128.840\ \ s^2/m^2}$
Core losses density	$\frac{Core\ losses\ density\ of\ the\ \ material}{554.737\ \ mW/mm^3}$
Operating temperature	$\frac{Operating\ temperature\ of\ the\ \ material}{200^0C}$
Curie temperature	$\frac{Curie\ temperature\ of\ the\ \ material}{770^0C}$

Table 6.9: Linkert scale for properties presented in qualitative information

Relative Cost	5-point Scale	
Cheap	1	
Cost effective	2	
Expensive	3	
More expensive	4	
Most expensive	5	
DC Bias and temperature stability	Mechanical strength	4-point scale
Poor	Very brittle	1
Good	Brittle	2
Better	Good	3
Best	Strong	4

Chapter 7 Performance Enhancement of Powertrain DC-DC Converters Using Variable Inductor

Original Title: Performance Enhancement of Powertrain DC-DC Converters Using Variable Inductor

Authors Affiliation:

- **Mebrahtom Woldelibanos Beraki**: PhD Student, Université de Sherbrooke, Faculté de génie, Département de génie électrique et de génie informatique
- **João P. Trovão** : Professor, Université de Sherbrooke, Faculté de génie, Département de génie électrique et de génie informatique
- **Marina S. Perdigão:** Professor, Instituto de Telecomunicações and Polytechnic Institute of Coimbra, 3030-290 Coimbra, Portugal

Under review: IET Electrical Systems in Transportation

Summary

Content: This paper presents the performance enhancement of large-scale powertrain DC-DC converter. A simple strategy is proposed in order to dynamically vary the magnetic property of the core in order to regulate its saturation level. To simplify the design of the controllers of the large-scale converter affine parameterization is used. The suitability of the proposed approach for improving the performance of powertrain DC-DC converters and reducing the switching stress and energy storage system variations are evaluated through simulations. The evaluations reveal significant improvements in efficiency, reducing the switching stress and battery current variation and current ripple control.

Results: The integration of the VI in largescale powertrain DC-DC converter, its control and the proposed strategy for improving the performance are evaluated through simulations. The results reveal significant improvements in the aging index of energy storage systems (6.73% in the battery current coefficient of variation) and switching stress parameter (17.87% reduction). Furthermore, a worth recording up to 13.70% efficiency improvements are noted.

Contribution to the thesis: For system level integration and smooth functionality of the VI in powertrain DC-DC converters, a strategy and closed loop system control are vital. This Chapter uses the procedures used in Chapter 4, and the VI designed using the RMS in Chapter 5 and the material selected based on the procedures presented in Chapter 6, to provide a comprehensive evaluation of the VI based converter and verifies the significance of the current controlled magnetic device for large-scale electrified vehicles applications. This Chapter summaries the main procedures and concepts developed in this thesis and provides in-depth analysis of the performance enhancement of large-scale VI based powertrain DC-DC converters.

Abstract

This paper provides the performance enhancement of powertrain DC-DC converter using a current controlled magnetic device, the variable inductor (VI). The VI is composed of two group of windings where the auxiliary winding is used to regulate the permeability of the magnetic core in order to control its saturation level over a wide range of load variations. An appropriate level of auxiliary winding current is needed to regulate its saturation level and to avoid post-saturation operation of the power inductor. To this end, a simple and dynamic strategy is proposed to estimate the auxiliary winding currents of VI. Furthermore, affine parameterization approach is used to ease the design of the control loop parameters of the powertrain DC-DC converter. The proposed strategy enables the continuous regulation of the magnetic property of the power inductor core and contributes to the performance enhancement of the powertrain DC-DC converter. The proposed approach is validated using simulation studies of a large-scale VI- based powertrain DC-DC converter. The simulation results reveal the significance of the magnetic control for enhancing the performance efficiency of the converter up to 13.70% and reducing the stress on switching devices by 17.87%. Furthermore, the energy source current variation is reduced by 6.73% and control the current ripple across the power inductor.

7.1 Introduction

The global climate change challenge require an immediate attention and vital steps are needed to reduce greenhouse gas (GHG) emissions and energy consumption [252]. Electrifying the transportation sector, harnessing renewable energy technology and enhancing the energy efficiency are key solutions to reduce climate change crisis. Due to its heavy reliance on fossil fuels, the transportation sector is one of the major contributors of CO_2 emissions. Development of electrified vehicles (EVs) and hybrid electric vehicles (HEVs) is one of the fundamental solutions to address this problem [253]. EVs and HEVs can improve the efficiency and reduce our reliance on fossil fuels, fuel consumption and GHG emissions. In the context, the power electronic circuits are key in EVs and HEVs, and they are used for controlling the energy conversion and interfacing the energy storage systems (ESSs). Their size and characteristics affect the driving performance and reliability. Subsequently, these circuits are required to have smaller size, high power density, and high efficiency [254]. This is particularly important in traction applications to meet stringent space limitation. Furthermore, the high power requirement, low voltage and variable range cause high currents which affects the electric and thermal stresses in both active and passive components [255].

The size, cost and performance of powertrain DC-DC converters is dominated by the magnetic components [116], [19]. The presence of bulky power inductors influences the overall size of EVs and limits space for ESS. Furthermore, if it is forced to operate at higher currents the input current ripple will be high and can cause undesirable electromagnetic interference, mechanical vibrations, losses and affects the lifetime of the ESS [256].

To reduce the size of the magnetic components while controlling the current ripple a current controlled variable inductor (VI) is proposed. Being a current controlled device, the VI is composed of magnetic core materials, multiple windings with an interaction of main and auxiliary winding currents. These introduce design, suitable materials selection, characterization, and control challenges for integrating it into power electronic converters for practical applications.

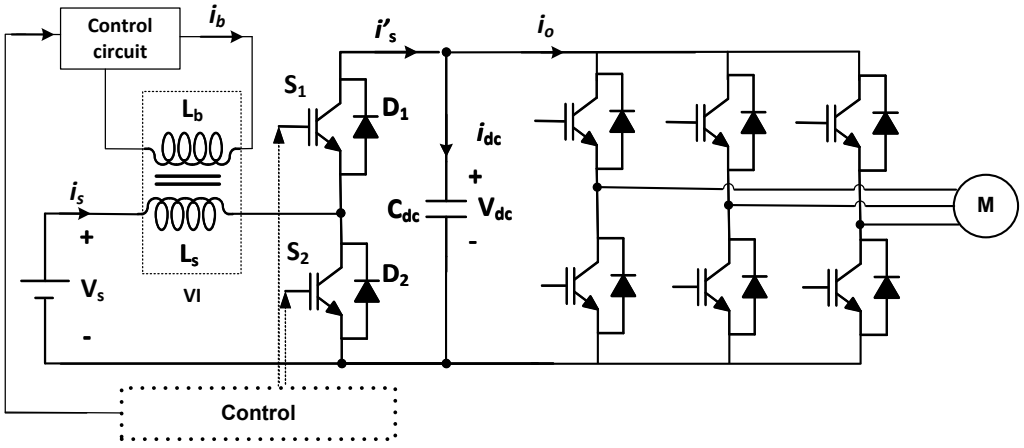

Figure 7.1: A variable inductor-based power conversion architecture

The detailed modeling and characterization of a small-scale VI is provided in [139]. Its design is addressed in [257] and the selection of suitable magnetic core materials based on the weighted property method is dealt in [258]. Nonetheless, its control for systems integration and its impact on the performance of DC-DC converters is not yet addressed. The focus of this paper is to tackle the control issues and analyze the performance improvements due to its integration into powertrain DC-DC converters.

Several magnetic control based converters are proposed in literature [16], [108], [139], [147],[106]. The first three are based on the VI and focused on ripple and saturation control. The last two are based on magnetorheological fluid and permanent magnet based respectively focused on the proof of concept of small-scale converters. Nonetheless, the detailed performance analysis and closed loop system control for integration of such converters is yet to be addressed. Furthermore, the power inductor of such types of converters are either composed of multiple windings, a permanent magnet or magnetorheological fluid. This mandates a suitable strategy for a smooth operation of the device and performance enhancement of the power conversion components. A simple strategy based on heuristic approach that relates the currents between the two windings of the magnetic device is presented in [139]. Nonetheless, for large-scale integration of the VI into powertrain DC-DC converters, a systematic strategy that considers variations of permeability of the magnetic cores to estimate the auxiliary winding current is essential.

The main objective of this paper is to provide a simple dynamic strategy for controlling the inductance of magnetic core material to enhance the performance of the powertrain DC-DC converter, and control of the powertrain DC-DC converter. The behavior of the power inductor with different levels of current is extracted from intensive FEA simulations (MagNet infolytica), simulations and the characteristics (linkage flux to main winding current, and the inductance to the main winding) are used to model the magnetic device. The model obtained from FEA simulations is used to study the feasibility of a large-scale magnetic control-based converter, to validate the proposed strategy and quantify the performance improvements.

This paper is organized as follows. Section 7.2 provides the description of the study system and the design of the DC-DC converter taking into consideration a three-wheel recreational vehicle. The modeling of the VI, the DC-DC converter and the control are provided in section 7.3. Section 7.4 provides the detailed simulations of the converter and evaluation of different parameters to quantify the improvements and validate the proposed strategy. Finally, the concluding remarks and future directions are presented in section V.

7.2 System Description and Design

The study system is composed of energy storage system as a source, half-bridge DC-DC converter module, an inverter, an electrical motor, and the control layer as shown in Figure 7.1. This configuration is commonly used by several automotive manufacturers such as Toyota Prius. The traction DC-DC converter enable DC-link regulation, enhance the main energy storage system life time, and extends the motor speed range and improve the efficiency of the electric drive [259]. In such types of converters, the size and performance are dominated by the magnetic components. In order to have compact power conversion unit with improved performance, the classical power inductor is replaced with a VI as shown in Figure 7.1.

The control layer is composed of the main converter control and a strategy. The strategy decides the mode of operation of the auxiliary winding and estimates the amount of auxiliary winding current needed to regulate the magnetic property of the magnetic core. The proposed strategy helps in maintaining the inductance at higher currents and stabilize the controllers.

Unlike the classical constant value model, the inductance is modelled using the 2-D lookup table. For developing the control and the strategy, the inductance vs current curve is obtained from FEA simulations. The inductance is calculated from the linkage flux obtained from the FEA. The model of the inductor which shows the dependence of inductance on the main and auxiliary winding currents was created in a 2-D lookup table in Matlab/Simulink environment.

From a given specifications of a desired application, the parameters of the DC-DC converter can be selected based on the fundamental design procedures. Based on the specifications provided in Table 7.1, the passive components and the operating range of duty cycles are estimated as shown below.

Table 7.1: Converter Specifications

Parameter	Symbol	Value
Input voltage range (V)	V_s	40-85
Nominal input voltage (V)	$V_{s\ nom}$	48
Output voltage range (V)	V_o	90-120
Nominal output voltage (V)	$V_{o\ nom}$	96
Current ripple*	ΔI	30%
Voltage ripple	ΔV	2%
Nominal power (kW)	P_{nom}	33
Peak power (kW)	P_{max}	82
PWM switching frequency (kHz)	f_{sw}	20
Calculated Parameters		
Inductance (μH)	4.57	
DC-Link Capacitor (mF)	4.2	
Duty Cycle Range (%)	6 - 67	
Switching Device	FZ1200R45HL3	

* Selected within a range that minimize the inductor size and maximize the flexibility of the auxiliary winding current control.

These specifications are obtained from a specific requirement of the three wheel recreational vehicle [154] shown in Figure 7.2. In boost/buck modes of operation, the range of duty cycle operations, the inductance and capacitance are estimated using the formulas presented in Table 7.2.

Figure 7.2: e-TESC Lab Three-wheel recreational vehicle

Table 7.2: Formulas for different Modes of operation

	Boost Mode	Buck Mode
$D_{\min\_boost}$	$1-\left(\frac{V_{in\_max}}{V_{out\_min}}\right)$	$\frac{V_{in\_min}}{V_{out\_min}}$
D_{nom_boost}	$1-\left(\frac{V_{in\_nom}}{V_{out\_nom}}\right)$	$\frac{V_{in\_nom}}{V_{out\_nom}}$
$D_{\max\_boost}$	$1-\left(\frac{V_{in\_min}}{V_{out\_max}}\right)$	$\frac{V_{in\_max}}{V_{out\_max}}$
Δi_L	$\frac{V_{in\_min}D_{max}}{L_{boost}f_{sw}}$	$\frac{(V_{in\_max}-V_{out\_min})D_{max}}{L_{buckt}f_{sw}}$
Δv_{out}	$\frac{V_{dc}D_{max}}{RCf_{sw}}$	$\frac{V_{dc}D_{max}}{RCf_{sw}}$
$L_{boost/buck}$	$\frac{V_{in\_min}D_{max}}{\Delta i_L f_{sw}}$	$\frac{(V_{in\_max}-V_{out\_min})D_{max}}{\Delta i_L f_{sw}}$
C	$\frac{V_{dc}D_{max}}{R\Delta v_{out}f_{sw}}$	$\frac{(1-D_{min})}{8L\Delta v_{out}{f_{sw}}^2}$

In Table 7.2, $D_{\min\_boost}$, D_{nom_boost}, D_{max_boost}, V_{in_min}, V_{in_nom},, V_{in_max}, V_{out_min}, V_{out_nom} and V_{out_max} are the minimum duty cycle, nominal duty cycle, maximum duty cycle, minimum input voltage, nominal input voltage, maximum input voltage, minimum output voltage, nominal output voltage and maximum output voltage respectively.

The minimum inductance required for bidirectional operation can be selected as the maximum of the inductances in row 7 of Table 7.2, as shown in (7.1). To assure CCM operation, an inductor value greater than the minimum values in (1) should be selected.

$$L_{\_min} = max(L_{boost}, L_{buck}) \tag{7.1}$$

7.3 Modeling and Control

7.3.1 Variable Inductor Modeling using FEA

The modelling of the VI with different levels of main and auxiliary winding currents is obtained from a thorough FEA simulations. The power inductor is designed to meet the requirements of a powertrain DC-DC converter for a three wheel recreational vehicle presented in [154]. For different levels of currents, the inductance, linkage flux and permeability vs currents are investigated, and the required curves are obtained in order to provide the characterization of the VI. The main winding currents are varied from 0-2500A, in steps of 1A, and the auxiliary winding currents are varied from 0-5A, in steps of 0.5 A. The inductance characterization as a function of the main and auxiliary winding currents is shown in Figure 7.3.

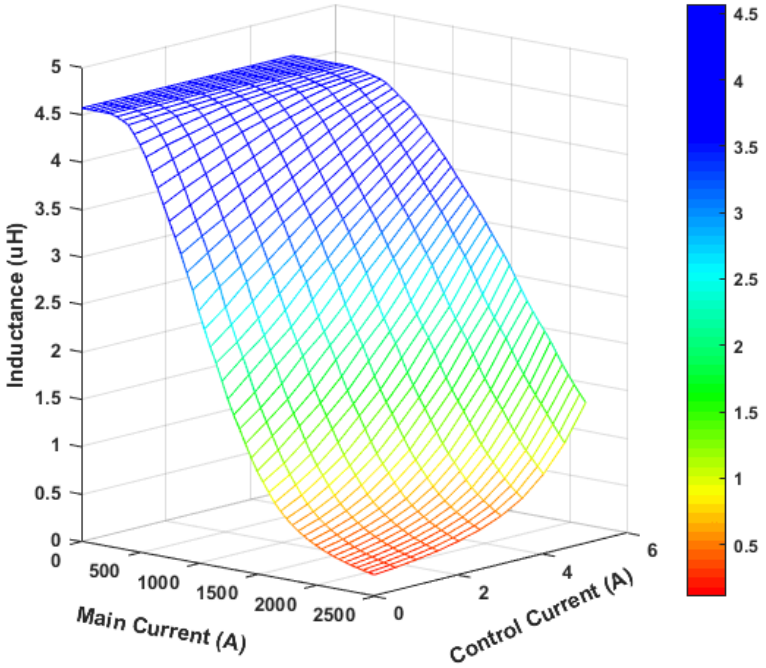

Figure 7.3: Inductance vs main winding current for different auxiliary winding currents

The inductance variation of the VI is derived from linkage flux information using the procedures presented in detail in [17]. The characteristics curves obtained in this section are used in the model of the power inductor to investigate the features of the VI for improving the performance of powertrain DC-DC converters. As is revealed in Figure 7.3, the saturation level of the power inductor is increased significantly as we increase the levels of current in the auxiliary winding of the VI.

7.3.2 Converter Modeling

Using the modelling procedures presented in [157], the modelling of the half bridge converter is illustrated in detail in this section: The state variables are i_L, and v_{dc}. The two switches of the converter are controlled in a complementary manner. The state equations for different modes of operation of the converter can be derived as shown below.

Mode 1: Switches S_2 is on and D_1 is off. Applying the basic Kirchhoff's laws in this mode of operation, the dynamic equations that describe the inductor voltage and the capacitor current can be expressed as:

$$\begin{cases} \dfrac{di_{s(t)}}{dt} = \dfrac{v_{s\,(t)}}{L} \\ \dfrac{dv_{dc(t)}}{dt} = -\dfrac{v_{dc\,(t)}}{RC_{dc}} \end{cases} \tag{7.2}$$

Mode 2: Switches S_2 is off and D_1 is on. The inductor voltage and capacitor voltage are expressed by set differential equations in (4).

$$\begin{cases} \dfrac{di_{s(t)}}{dt} = \dfrac{v_{s\,(t)}}{L} - \dfrac{v_{dc\,(t)}}{L} \\ \dfrac{dv_{dc(t)}}{dt} = \dfrac{i_{s\,(t)}}{C_{dc}} - \dfrac{v_{dc\,(t)}}{RC_{dc}} \end{cases} \tag{7.3}$$

Considering ideal components, the average model of the converter over a switching period is expressed as:

$$\frac{di_{s(t)}}{dt} = \frac{v_s(t)}{L} - \frac{\big(1 - d_s(t)\big)v_{dc}(t)}{L} \tag{7.4}$$

$$\frac{dv_{dc(t)}}{dt} = \frac{i_s(1 - d(t))}{C_{dc}} - \frac{v_{dc}\,(t)}{C_{dc}R} \tag{7.5}$$

where, i_s, v_s, v_{dc}, d_s, L and R are the current across the power inductor, the source voltage, the dc-link voltage, the duty cycle, the inductance of the power inductor and the resistance of the load respectively. After linearizing (4) and (5), neglecting the DC and second order AC quantities the average model of the converter can be expressed as:

$$\frac{d\widehat{\imath_L}(t)}{dt} = \frac{\widehat{v_s}(t)}{L} - \frac{(1-D)\,\widehat{v_{dc}}(t)}{L} + \frac{\widehat{d}(t)V_{dc}}{L} \tag{7.6}$$

$$\frac{d\,\widehat{v_{dc}}(t)}{dt} = \frac{((I_L\,\widehat{d}(t) + \widehat{\imath_L}(t) + \widehat{\imath_L}(t)D)}{C_{dc}} - \frac{\widehat{v_{dc}}(t)}{C_{dc}R} \tag{7.7}$$

After simplifying and taking the Laplace transform, the transfer functions can be expressed as:

$$\frac{\widehat{\imath_s}(s)}{\widehat{d}(s)} = \frac{(C_{dc}V_{dc})s + 2(1-D)I_s}{(LC_{dc}\,)s^2 + \frac{L}{R}s + (1-D)^2} \tag{7.8}$$

$$\frac{\widehat{v_{dc}}(s)}{\widehat{\imath_s}(s)} = \frac{(1-D)V_{dc} - (LI_s\,)s}{(C_{dc}V_{dc})s + 2(1-D)I_s} \tag{7.9}$$

The expressions in (8) and (9) are the control to input current and current to output small signal transfer functions respectively.

7.3.3 Control Design

The inner loop and outer loop controllers for the transfer functions shown in (8) and (9) are designed using affine parameterization. The affine parametrization approach is simple and makes the selection and tuning of model based controllers easier [260], [96]. Furthermore, it ensures the stability of the system with the variations of the operating conditions. Unlike the classical approaches, this method starts with the nominal closed loop transfer function and enables open loop design to closed loop implementation [261].

Figure 7.4 reveals the standard closed loop system with a negative feedback and affine parameterization illustration. For a given transfer function $G(s)$ and a controller $C(s)$ the closed loop transfer function $T(s)$ is expressed as in (7.10).

$$T(s) = \frac{G(s)C(s)}{1 + G(s)C(s)} \tag{7.10}$$

Introducing $Q(s)$ in series with the transfer function $G(s)$, as shown in Figure 7.4 (b), where $Q(s)$ is selected in such away it provides equivalence to the classical closed loop transfer function as in (7.11).

$$T(s) = Q(s)G(s) \tag{7.11}$$

Depending on the relative degree and type of $G(s)$ stability situation and presence of non-minimum phase zeros (NMPZ), $Q(s)$ is derived as:

$$Q(s) = F_Q(s)\, G^i(s) \tag{7.12}$$

where $F_Q(s)$ the transfer function is defined for the performance expected taking into consideration of the dynamic characteristics of the plant. $G^i(s)$ is $(G(s))^{-1}$ for stable systems with minimum phase zero (MPZ) plants. On the other hand, the NMPZ are excluded from $(G(s))^{-1}$.

From (7.10) and (7.11), the controller can be deduced from the Q plant and the transfer function of the plant as shown in (7.13).

$$C(s) = \frac{Q(s)}{1 - Q(s)G(s)} \tag{7.13}$$

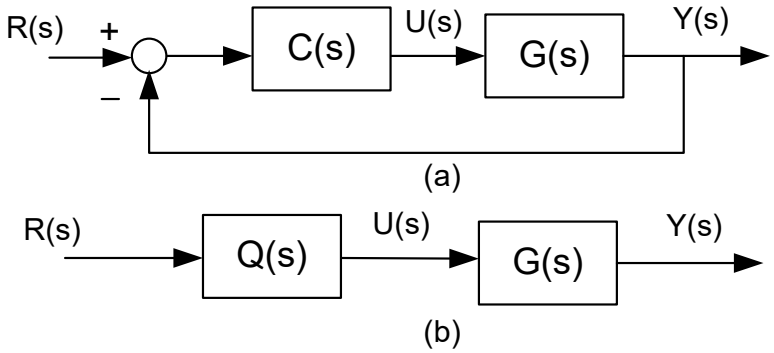

Figure 7.4: (a) Standard closed loop system (b) Affine parameterization representation of closed loop system

For the study system, the inner loop current controller and the outer loop voltage controller are designed using the procedures presented in this section. The inner loop the transfer function has a relative degree 1 with one minimum phase zero and two stable poles, subsequently $F_Q(s)$ with relative degree of one is suitable for estimating the Q function and can be expressed as:

$$F_Q(s) = \frac{1}{1 + \alpha_x s} \tag{7.14}$$

where α_x is a tuning parameter and is equal to the reciprocal of desired natural frequency ($w_{v/i}$) and the desired damping factor ($\gamma_{v/i}$).

$$Q_i(s) = \frac{s^2 + \frac{1}{RC_{dc}}s + \frac{(1-D)^2}{(LC_{dc})}}{\frac{2((1-D)I_s}{LC_{dc}}(1+\alpha s)(\frac{C_{dc}V_{dc}}{(1-D)I_s})s + 1)} \tag{7.15}$$

Similarly, the outer loop has one pole and NMPZ. For such types of plants, the NMPZ is eliminated for obtaining the $Q_v(s)$ [260]. Hence, the system will have a relative degree of one, $F_Q(s)$ can be selected the same as (7.14) with values of α different from (7.14) and the $Q_v(s)$ will be as shown in (7.16).

$$Q_v(s) = \frac{1 + \frac{C_{dc}V_{dc}}{2(1-D)I_s}s}{\frac{V_{dc}}{2I_s}(1+\alpha s)} \tag{7.16}$$

Using (7.15) and (7.16) the current controller and voltage controller are designed using the equations as shown in Table III. The PID controller which is shown in (7.17) is commonly used industrial applications.

$$C(s) = K_{p,v/i} + \frac{K_{i,v/i}}{s} + \frac{K_{d,v/i}}{sT_{d,v/i} + 1} \tag{7.17}$$

where $K_{p,v/i}$, $K_{i,v/i}$, $K_{d,v/i}$, $T_{d,v/i}$ are the proportional gain, integral gain, differential gain and filter time constant in respective order. Relating the gain parameters of the PID to controller obtained using affine parameterization the values of the controllers gains will be easily obtained as shown in Table 7.3.

Table 7.3: Controllers for the main converter

	Voltage Controller Parameters	Current Controller Parameters
$w_{v/i}$	$\frac{2\pi F_{sw}}{100}$	$\frac{2\pi F_{sw}}{10}$
$\gamma_{v/i}$	0.707	0.707
$K_{p,v/i}$	$\frac{\tau_{p,v}}{K_{o,v}(\alpha_v + \tau_{z,v})}$	$\frac{2\gamma w\,(\alpha_i + \beta) - \alpha_i \beta w^2}{K_{o,i}(\alpha_i + \beta)^2}$
$K_{i,v/i}$	$\frac{1}{K_{o,v}(\alpha_v + \tau_{z,v})}$	$\frac{w^2}{K_{o,i}(\alpha_i + \beta)}$
$K_{d,v/i}$	0	$\frac{(\alpha_i + \beta)^2 - 2\gamma w(\alpha_i + \beta)\alpha_i\beta - ((\alpha_i \beta w)^2}{K_{o,i}(\alpha_i + \beta)^2}$
$T_{d,v/i}$	0	$\frac{\alpha_i \beta}{K_{o,i}(\alpha_i + \beta)}$

In Table 7.3, $K_{o,v} = \frac{V_{dc}}{2I_s}$, $\tau_{p,v} = \frac{C_{dc}V_{dc}}{2(1-D)I_s}$, $\tau_{z,v} = \frac{(LI_s)}{(1-D)V_{dc}}$, $w = \frac{(1-D)}{\sqrt{(LC_{dc})}}$, $K_{o,i} = \frac{2((1-D)I_s}{LC_{dc}}$, and $\beta = \frac{C_{dc}V_{dc}}{2(1-D)I_s}$ are parameters of the transfer functions.

7.3.4 Current follower strategy

The proposed current follower strategy determines the amount of auxiliary winding current based on the main winding levels of current. It enables the smooth operation of the VI depending on the levels of main winding currents. The strategy is developed based on the linkage flux (λ) vs main winding current (i_s) characterization curves.

The λ-i_s characterization curves of the magnetic core material are obtained from a series of FEA simulations for different levels of currents in the main and auxiliary windings. For each λ-i_s curve, the point of maximum value of the slope of the change of linkage flux to change of main winding current ($\frac{d\lambda}{\mathrm{d}i_s}$) is determined using a moving slope estimation, and the corresponding values of main and auxiliary winding are recorded. Using the main and auxiliary winding currents values in the corresponding curves, a simple mathematical relationship as in (18) is deduced using the curve fitting tool in Matlab®. The strategy enables the smooth operation of the power inductor for different loading situations by controlling the magnetic properties of the magnetic core material.

In normal operation, that is for currents lower than the saturation level of the magnetic core, the auxiliary winding will be idle, as a result the current follower strategy sets the reference current of the auxiliary winding zero. For current levels higher than the saturation current, the auxiliary winding current reference will be set in accordance to the analytical expression shown in (18). Due to its simplicity the proposed strategy can easily implemented in microcontrollers for real time applications.

$$i_b(i_s) = \begin{cases} 0, & i_s < i_{s\_sat} \\ ai_s^2 + bi_s + c & i_{s\_sat} \leq i_s \leq 2500 \end{cases} \tag{7.18}$$

where $a = 3.52 * 10^{-6}$, $b = 0.0159$ and $c = -12.96$.

7.4 Simulation and Evaluations

7.4.1 Simulation System

The vehicle under study is a three-wheel sports vehicle with a detailed specifications of the vehicle presented in [154]. The objective of the simulation is to illustrate the impact of the variable inductor and the proposed strategy for powertrain DC-DC converters for such types of vehicles. Furthermore, it is used to evaluate the controllers of the main converter and the proposed strategy for a full-scale VI based converter. The full-scale parameters of the converter are used to evaluate the suitability of the proposed on line current follower strategy and the controllers taking into consideration the varying nature the target application. The dynamic model of the power inductor

is extracted from a series of FEA simulations and included in the system modeling as a 2D lookup table.

To validate the model of the study system, the controllers and the strategy, simulations are carried out in MATLAB/SIMULINK. The simulation system is shown in Figure 7.5.

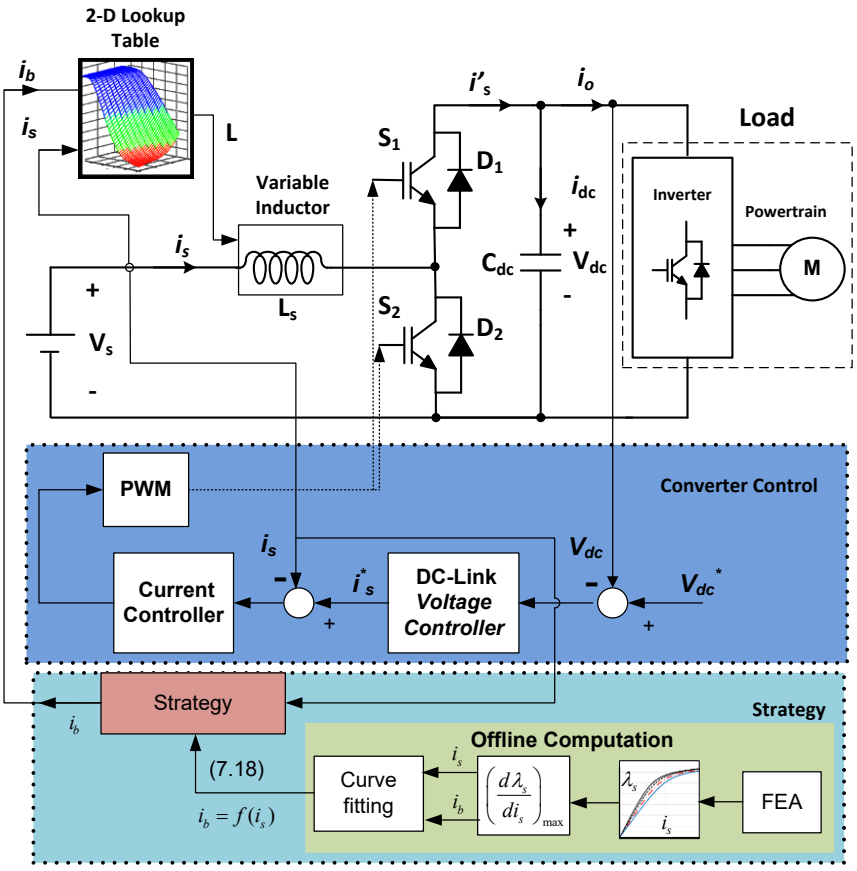

Figure 7.5: Simulation schematic diagram

7.4.2 Evaluations

To verify the suitability of the strategy for controlling the variable inductor for EV applications and the proposed control approach, several parameters such as the current ripple ratio, the inductance variation, the efficiency, and components stresses are considered to evaluate the merits of the VI for powertrain DC-DC converters.

The inductance curves and the current ripple variations are essential parameters that can be used to evaluate the performance improvements of the developed system and the control strategy. Figure 7.6 shows the demanded load power, the inductance currents, the inductance and the control current profiles in respective order. As is revealed in Figure 7.6 (b), the current ripple is significantly reduced when an auxiliary winding current is applied in accordance to the proposed strategy. Similarly, the inductance can be controlled when the main winding currents are increased significantly even higher than the saturation currents.

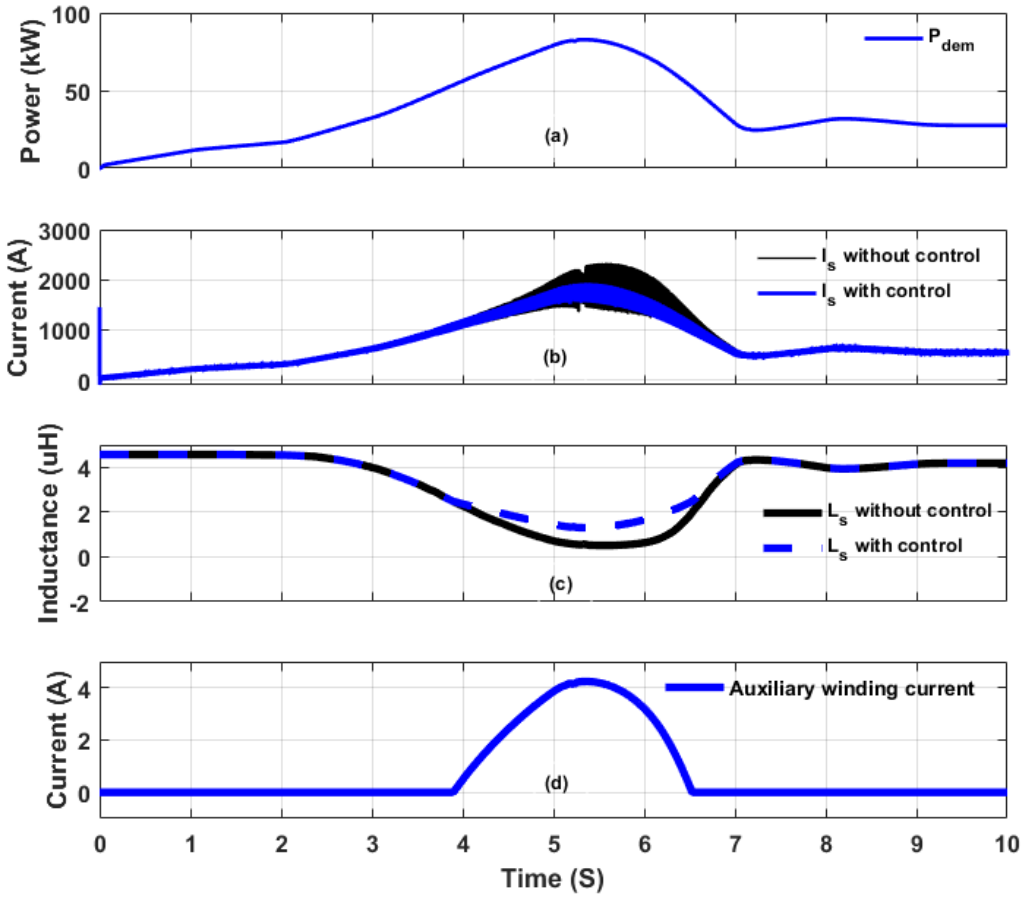

Figure 7.6: Large Scale Simulation results (a) demanded load power (b) inductor currents (c) inductance (d) auxiliary winding current

The switching stress in DC-DC converters is quantified as switch stress parameter (SSP_i), which is expressed for the i^{th} switch in the converter.

$$SSP_i = V_{dcpk,i}\, I_{spk,i} \tag{7.19}$$

where $V_{dcpk,i}$, and $I_{spk,i}$ is the peak voltage and peak current across the i^{th} switch.

By dynamically regulating the inductance of the power inductor with the help of the proposed strategy, the current ripple of the power inductor is reduced significantly. Subsequently, the losses across the components will be controlled and the stress across the switches and ESSs will be reduced. The simulation results in Figure 7.7 (a) and Figure 7.7 (b) reveal the effectiveness of the proposed strategy, the functionality of the model and the added values of VI integration to powertrain DC-DC converters.

The energy storage (battery) stresses which can affect its lifetime can be quantified by the peak current variations, RMS current, continuous current, and the coefficient of variation. The RMS current is related to the heating effect of the current and is responsible for the losses and it is estimated as:

$$I_{srms} = \sqrt{\frac{1}{n}\sum_{k=0}^{n} \left(I_s\,(k)\right)^2} \tag{7.20}$$

The standard deviation of the battery current also shows how the currents are spread from the continuous value of battery current. Higher value reveals the battery is exposed to wider range of current variations which is not good for its lifetime. The standard deviation (σ) is expressed as:

$$\sigma = \sqrt{\frac{1}{n}\sum_{k=0}^{n} (I_s\,(k) - \mu)^2} \tag{7.21}$$

The coefficient of variation which provides the ratio of the standard deviation to mean of the battery current is an essential parameter that gives the degree of variation of the battery current which is related to the lifetime of the battery. Smaller value signifies the degree of variation of the battery

current is small, hence the impact on the lifetime of the battery is smaller. The coefficient of variation is expressed as:

$$C_v = \frac{\sigma}{\mu} \tag{7.22}$$

where μ is the mean current of the battery over the time under consideration. Figure 7.7 (a) reveals the normalized values of I_{srms} , σ, SSP and C_v for the converter under study with conventional inductance and no control strategy (without control), and with VI and control strategy (with control). In the considered simulation time and the load profile shown in Figure.7.7 (a), a decrease of 6.15% in the I_{srms} , 10.55% decrease in σ, 17.87% decrease in SSP and 6.73% decrease in C_v is noted in Figure 7.7 (a). This reveals significant improvements due to the magnetic control and the proposed strategy.

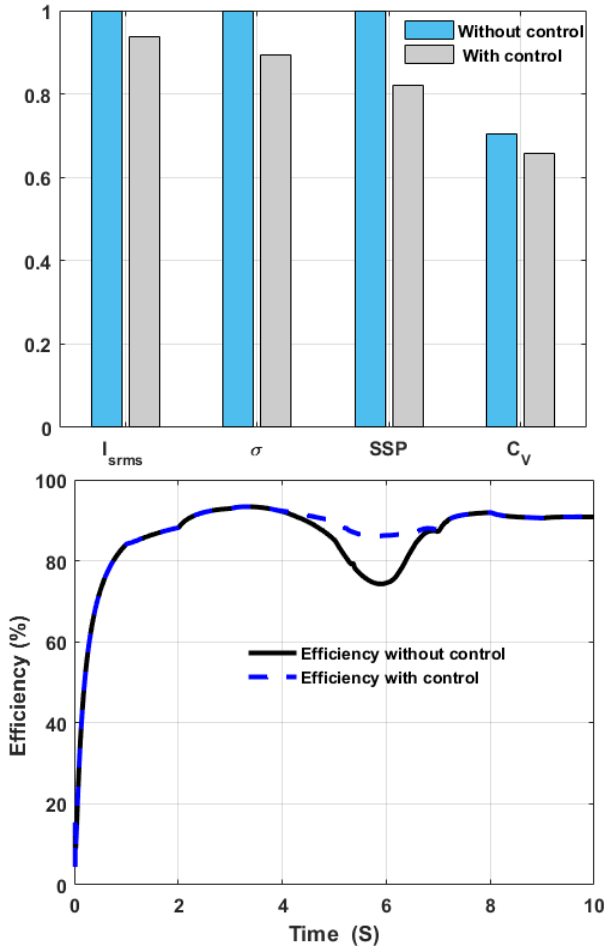

(a)

(b)

Figure 7.7: Performance enhancements due to VI (a) Summary of comparison results (b) Performance efficiency of powertrain DC-DC converter

The increase of current ripple leads to the increase of magnetic components losses, conduction losses and increase the stress in active switches. To quantify these concepts, it is important to include the impact of ripple current in influencing the copper and core losses. The detailed analytical expressions which relate this explanation are presented in [17]. The levels of current ripple also influence the switching losses. With the help of VI and the proposed strategy to the current ripple across the power inductor can be dynamically controlled as a result, the copper, core losses and devices stress are reduced. The efficiency which is an important metric of comparison and it is considered in evaluating the performance of the VI-based converter. In estimating the efficiency, the losses due to passive components including the auxiliary winding, the main winding, the energy source power losses and the active components power losses are considered.

Similarly, the conduction losses of the power switches will be affected by the levels of current ripples, considering IGBT switching device [262]. This can be illustrated using the mathematical relationships shown below. Assuming r to be the ratio of the peak-to-peak ripple current (I_{pk-pk}) to the average current (I_{savg}) across a power inductor.

$$P_{C\_IGBT} = 2I_T V_{CEST} + 2(1-D)I_o V_F + 2r_c\left(I_{T\_rms}\right)^2 \tag{7.23}$$

$$I_{T_{rms}} = I_{savg}\sqrt{D\left(1+\frac{r^2}{12}\right)} \tag{7.24}$$

where I_{IGBT} is the average IGBT current, V_{CEST} the voltage drop across the IGBT, I_o is the output current, V_F forward diode voltage, r_c is the collector emitter on state resistance and I_{T_rms} is the IGBT rms current.

Similarly, the conduction losses in a diode can be expressed as:

$$P_{C\_D} = 2V_D I_D + 2r_D\left(I_{D\_rms}\right)^2 \tag{7.25}$$

where V_D , I_D , r_D , I_{D_rms} are the diode forward voltage, average diode current, diode forward resistance and diode rms current respectively. In the same fashion, the current ripple affects the last

term in (7.25). Figure 7.7(b) reveals the efficiency curves of the converters with VI and control strategy (dotted lines) and with classical inductor and no strategy (solid line) for the load profile shown in Figure 7.6(a).With the VI and the proposed strategy up to 13.70% efficiency improvements are obtained for currents much higher than the rated current of the power inductor.

7.5 Conclusion

This paper provides a simple strategy for controlling the magnetic properties of the VI in order to improve the performance of large-scale powertrain DC-DC converter. The cascaded control loop parameters of the powertrain DC-DC converter are designed using affine parameterization approach. The integration of the VI in largescale powertrain DC-DC converter, its control and the proposed strategy for improving the performance are evaluated through simulations. The results reveal significant improvements in the aging index of energy storage systems (6.73% in the battery current coefficient of variation) and switching stress parameter (17.87% reduction). Furthermore, a worth recording up to 13.70% efficiency improvements are noted. The future directions will focus on the experimental validation of the proposed strategy and implementation of the large-scale VI based powertrain DC-DC converter.

7.6 Acknowledgment

This work was supported in part by Grant 950-230672 from Canada Research Chairs Program, in part by Grant RGPIN-2017-05924 from the Natural Sciences and Engineering Research Council of Canada, in part by Arbour Foundation Scholarship, University of Sherbrooke Faculty of Engineering Excellence Scholarship and by projects UID/MULTI/00308/2019 and by the European Regional Development Fund through the COMPETE 2020 Program and FCT – Portuguese Foundation for Science and Technology within projects ESGRIDS (POCI-01-0145-FEDER-016434) and MAnAGER (POCI-01-0145-FEDER-028040).

Chapter 8 Conclusions and Future Directions

8.1 Conclusions

This thesis explored the viability of VI for improving the performance and reducing the size and weight of DC-DC converters for electrified vehicles. To this end, the classical power inductor is replaced by a VI. This helps in enhancing the current capacity of power inductors, control the current ripple, reduces switching and magnetic losses, and reduces the stresses applied to switching devices.

A particular importance is given to the experimental investigation of a small-scale VI prototype to demonstrate the concept and explore its feasibility (chapter 3). Subsequently, a comprehensive finite element characterization is performed in order to determine the intrinsic functionality of the passive component in order to assess its suitability for electric vehicles applications (chapter 4). The results demonstrated the promising potential of the VI for improving the performance of the DC-DC converters and better utilization of the core by reducing its size for applications with a wide range of load variations such as electric vehicles.

To reduce the traditional oversizing of power inductors in DC-DC converters for EV applications, a systematic method of VI design based on RMS current is developed and presented in chapter 5. The design procedure is illustrated with a VI designed for a bidirectional DC-DC converter for a three-wheel recreational electric vehicle. With the proposed method, it is possible to maximize the reduction in size and weight of power inductors for traction applications leading to the overall converter size reduction. In the design of power inductors for powertrain DC-DC converters, the selection of magnetic core materials is a vital step. As such, in Chapter 6, we propose a systematic approach for selecting suitable magnetic core materials for powertrain DC-DC converters using the weighted property method and multi-attribute decision making analytical hierarchy process.

For system-level integration and smooth functionality of the VI in DC-DC converters, a saturation management strategy and closed loop system control are vital. In chapter 7, a simple strategy is

proposed to estimate the necessary auxiliary winding current to manage the saturation in accordance to the currents requested by the load. An affine parameterization approach is used to define the controller's parameters. Furthermore, a comprehensive evaluation of large-scale DC-DC converter with VI designed with the procedure presented in chapter 6 is carried out in order to assess the importance of the magnetic device for vehicle applications.

To recap, this thesis systematically addressed research challenges of integrating VI in DC-DC converters for EVs and revealed the significance of VI for improving the performance of such types of converters. Furthermore, a systematic VI design procedure and a comprehensive magnetic core materials selection approach for powertrain DC-DC converters are proposed. Finally, a simple strategy is defined in order to estimate the auxiliary winding currents for continuously regulating the magnetic permeability of the VI. The effectiveness of the VI for such type of application has been validated by a small-scale proof of concept prototype and large-scale intensive simulations for a three-wheeled recreational vehicle.

8.2 Future Directions

This thesis has shown the significance of the VI concept in improving the performance and reducing the size of bulky power inductors in powertrain DC-DC converters. Nonetheless, there are numerous areas in which this work can be further explored. Some of these include:

This thesis focused on the introduction of VI half-bridge converter for powertrain DC-DC converters. Furthermore, the concept can be useful in the innovation of several power electronic topologies for applications with wide range of load applications such as electrified vehicles, renewable energy resources, avionics, marine and pulsed applications.

The behavior and characterization of the VI are provided with the help of experimental studies and FEA simulations which take more time. Analytical models and methods would provide faster results. Hence developing analytical models of this device and its characterization is worth exploring.

The proposed design procedure can be further improved by taking into consideration the thermal characteristics of the VI and better designs can be attained with the help of magnetic core materials selection approach presented in Chapter 6 and multi-objective optimization approaches.

This thesis revealed the promising significance of VI in half-bridge converter improvement. The VI and a permanent magnet can further help in scaling down the size and performance of power electronic converters. Hence, this area is also worth investigating.

In this thesis, Si-based switching devices are considered, integration of the VI with WBG based converters can be of interest for further reduction of the size of passive components and improving the performance of converters.

Finally, hardware-in-the-loop validation and a full-scale experimental prototype are indeed appreciated to provide more realistic validations of the proposed approach.

8.3 Conclusions (FR)

Cette thèse a exploré la viabilité de l'usage du concept de bobine variable pour améliorer les performances et réduire la taille et le poids des convertisseurs CC-CC pour les véhicules électrifiés. Pour cela, l'inductance de puissance classique des convertisseur CC-CC a été remplacée par une bobine variable. Cela permet d'améliorer la capacité de gestion du courant des inductances de puissance, de contrôler l'ondulation du courant et réduire les pertes magnétiques et par commutation, bien comme les contraintes appliquées aux dispositifs de commutation. Une attention particulière est accordée à l'étude expérimentale d'un prototype de bobine variable à petite échelle pour démontrer le concept et explorer sa faisabilité (chapitre 3). Par la suite, une caractérisation complète par éléments finis a été développée pour déterminer le fonctionnement intrinsèque de ce composant passif et ainsi évaluer sa faisabilité pour des applications véhiculaires (chapitre 4). Les résultats ont démontrés le potentiel prometteur de la bobine variable pour l'amélioration des performances du convertisseur CC- CC et une meilleur utilisation du noyau par sa réduction de la taille pour les applications avec une large gamme de variations du courant de charge, comme le cas d'une chaîne de traction d'un véhicule électrifié.

Pour réduire le traditionnel surdimensionnement des inductances de puissance dans les convertisseurs CC-CC pour des applications de traction électrique, une méthode systématique de design de bobine variable basée sur le courant RMS a été développée et présentée au chapitre 5. La procédure de design est illustrée par un exemple d'une bobine variable pour un convertisseur CC-CC bidirectionnel pour un véhicule récréatif à trois roues véhicule électrique. Avec la méthode proposée, il est possible de maximiser la réduction de la taille et le poids des bobines de puissance pour les applications de traction conduisant à la réduction globale de la taille du convertisseur. Dans ce design systématique, la sélection des matériaux du noyau magnétique est une étape essentielle. Pour cela au chapitre 6, nous proposons une approche pour sélectionner le matériau du noyau magnétique approprié pour les convertisseurs CC-CC utilisés dans la chaine de traction en utilisant la méthode des propriétés pondérées et le processus de hiérarchie analytique de prise de décision multi-attributs.

Pour une intégration au niveau du système et le bon fonctionnement de la bobine variable dans les convertisseurs CC-CC, une stratégie de gestion de la saturation et une commande du système en boucle fermée sont essentiels. Dans le chapitre 7, une stratégie simple est proposée pour estimer le courant nécessaire à l''enroulement auxiliaire pour une gestion de la saturation en fonction du courant demandé par la charge. Une méthode de synthèse affine a été utilisée pour définir les paramètres des contrôleurs. En outre, une évaluation complète par simulation du convertisseur CC-CC à grande échelle avec la bobine variable issue de la méthode de design systématique est effectuée afin d'évaluer l'importance de l'impact de ce nouveau dispositif magnétique pour des applications véhiculaires.

En résumé, cette thèse a abordée les défis de recherche de l'intégration de bobines variables dans les convertisseurs CC-CC pour les véhicules électriques et a démontrée l'importance de ce dispositif magnétique pour l'amélioration des performances de ce type de convertisseurs. De plus, une procédure de design systématique de bobines variables a été mise en œuvre et une approche complète de sélection de matériaux magnétiques pour les noyaux des convertisseurs CC-CC utilisés dans les chaines de traction sont proposées. Enfin, une stratégie simple est définie afin d'estimer les courants de l'enroulement auxiliaire pour réguler en continu la perméabilité magnétique de la bobine variable. L'efficacité de la bobine variable pour ce type d'application a

été validée par un prototype de preuve de concept à petite échelle et des simulations intensives de convertisseur CC-CC à grande échelle pour un véhicule récréatif à trois roues.

References

[1] R. M. Henderson, S. A. Reinert, P. Dekhtyar, and A. Migdal, "Climate change in 2018: Implications for business," *risk,* vol. 1, 2015.

[2] A. Schäfer, J. B. Heywood, H. D. Jacoby, and I. A. Waitz, *Transportation in a climate-constrained world*: MIT press, 2009.

[3] EIA. *Total Energy Annual Data* -. [Online]. Available: https://www.eia.gov/totalenergy/data/annual/index.php. [Accessed: 22-Oct-2019].

[4] B. Bilgin, P. Magne, P. Malysz, Y. Yang, V. Pantelic, M. Preindl*, et al.*, "Making the Case for Electrified Transportation," *IEEE Transactions on Transportation Electrification,* vol. 1, no.1, pp. 4-17, 2015.

[5] J. Tollefson, "Car industry: Charging up the future," *Nature,* vol. 456, no.7221, pp. 436-440, 2008.

[6] W. Enang and C. Bannister, "Modelling and control of hybrid electric vehicles (A comprehensive review)," *Renewable and Sustainable Energy Reviews,* vol. 74, pp. 1210-1239, 2017.

[7] M. Guerra. *Predictions for the New Year in Analog & Power Electronics*. [Online]. Available: www.electronicdesign.com/power/predictions-new-year-analog-power-electronics. [Accessed: 29-Dec-2017].

[8] *The Global Electric Vehicle Market In 2019 – Virta*. [Online]. Available: https://www.virta.global/global-electric-vehicle-market. [Accessed 3-Jan-2020].

[9] B. Nykvist and M. Nilsson, "Rapidly falling costs of battery packs for electric vehicles," *Nature Climate Change,* vol. 5, no.4, pp. 329-332, 2015/04/01 2015.

[10] G. Abad, *Power Electronics and Electric Drives for Traction Applications*: John Wiley & Sons, 2016.

[11] K. Chau and Y. Wong, "Hybridization of energy sources in electric vehicles," *Energy Conversion and Management,* vol. 42, no.9, pp. 1059-1069, 2001.

[12] T. Burress, "Benchmarking EV and HEV technologies," *Oak Ridge National Laboratory,* 2014.

[13] H. Wen, W. Xiao, X. Wen, and P. Armstrong, "Analysis and evaluation of DC-link capacitors for high-power-density electric vehicle drive systems," *IEEE Transactions on Vehicular Technology,* vol. 61, no.7, pp. 2950-2964, 2012.

[14] A. Abdelrahman, K. Algarny, and M. Youssef, "A Novel Platform for Power Train Modeling of Electric Cars with Experimental Validation Using Real-Time Hardware in-the-Loop (HIL): A Case Study of GM Chevrolet Volt 2nd Generation," *IEEE Transactions on Power Electronics,* 2018.

[15] R. Hooper, B. Guy, and R. Perrault, "A current-controlled variable inductor," *Instrumentation & Measurement Magazine, IEEE,* vol. 14, no.4, pp. 39-44, 2011.

[16] M. S. Perdigão, J. P. F. Trovão, J. M. Alonso, and E. S. Saraiva, "Large-signal characterization of power inductors in EV bidirectional DC–DC converters focused on core size optimization," *IEEE Transactions on Industrial Electronics,* vol. 62, no.5, pp. 3042-3051, 2015.

[17] M. Beraki, J. P. Trovão, and M. Perdigão, "Characterization of variable inductors using finite element analysis," *Simulation Modelling Practice and Theory,* vol. 97, p. 101952, 2019.

[18] L. Kumar, K. K. Gupta, and S. Jain, "Power electronic interface for vehicular electrification," in *Industrial Electronics (ISIE), 2013 IEEE International Symposium on*, 2013, pp. 1-6.

[19] H. Chen, H. Kim, R. Erickson, and D. Maksimović, "Electrified Automotive Powertrain Architecture Using Composite DC–DC Converters," *IEEE Transactions on Power Electronics,* vol. 32, no.1, pp. 98-116, 2017.

[20] M. Hirakawa, M. Nagano, S. Hashino, and T. Shimizu, "High Power Density Technologies on EV Bidirectional DC/DC Converters: Downsizing Effect using Close-Coupled Inductors," SAE Technical Paper2011.

[21] J. O. Estima and A. J. M. Cardoso, "Efficiency analysis of drive train topologies applied to electric/hybrid vehicles," *IEEE Transactions on Vehicular Technology,* vol. 61, no.3, pp. 1021-1031, 2012.

[22] D. Urciuoli and C. Tipton, "Development of a 90 kW bi-directional DC-DC converter for power dense applications," in *Applied Power Electronics Conference and Exposition, 2006. APEC'06. Twenty-First Annual IEEE*, 2006, p. 4 pp.

[23] K. Tytelmaier, O. Husev, O. Veligorskyi, and R. Yershov, "A review of non-isolated bidirectional dc-dc converters for energy storage systems," in *2016 II International Young Scientists Forum on Applied Physics and Engineering (YSF)*, 2016, pp. 22-28.

[24] C. Li, L. Herrera, J. Jia, L. Fu, A. Isurin, A. Cook*, et al.*, "Design and Implementation of a Bidirectional Isolated Ćuk Converter for Low-Voltage and High-Current Automotive DC Source Applications," *Vehicular Technology, IEEE Transactions on,* vol. 63, no.6, pp. 2567-2577, 2014.

[25] H. Chen, K. Sabi, H. Kim, T. Harada, R. Erickson, and D. Maksimovic, "A 98.7% efficient composite converter architecture with application-tailored efficiency characteristic," *IEEE Transactions on Power Electronics,* vol. 31, no.1, pp. 101-110, 2015.

[26] L. Wuhua and H. Xiangning, "Review of Nonisolated High-Step-Up DC/DC Converters in Photovoltaic Grid-Connected Applications," *Industrial Electronics, IEEE Transactions on,* vol. 58, no.4, pp. 1239-1250, 2011.

[27] S. A. Gorji, H. G. Sahebi, M. Ektesabi, and A. B. Rad, "Topologies and Control Schemes of Bidirectional DC–DC Power Converters: An Overview," *IEEE Access,* vol. 7, pp. 117997-118019, 2019.

[28] S. Waffler, J. Biela, and J. W. Kolar, "Output ripple reduction of an automotive multi-phase bi-directional dc-dc converter," in *Energy Conversion Congress and Exposition, 2009. ECCE 2009. IEEE*, 2009, pp. 2184-2190.

[29] L. Jiang, C. C. Mi, S. Li, M. Zhang, X. Zhang, and C. Yin, "A novel soft-switching bidirectional DC–DC converter with coupled inductors," *IEEE Transactions on Industry Applications,* vol. 49, no.6, pp. 2730-2740, 2013.

[30] Z. Yao and S. Lu, "A Simple Approach to Enhance the Effectiveness of Passive Currents Balancing in an Interleaved Multiphase Bidirectional DC–DC Converter," *IEEE Transactions on Power Electronics,* vol. 34, no.8, pp. 7242-7255, 2018.

[31] A. Kolli, A. Gaillard, A. De Bernardinis, O. Bethoux, D. Hissel, and Z. Khatir, "A review on DC/DC converter architectures for power fuel cell applications," *Energy Conversion and Management,* vol. 105, pp. 716-730, 2015/11/15/ 2015.

[32] Y. Du, S. Lukic, B. Jacobson, and A. Huang, "Review of high power isolated bi-directional DC-DC converters for PHEV/EV DC charging infrastructure," in *2011 IEEE Energy Conversion Congress and Exposition*, 2011, pp. 553-560.

[33] D. M. Bellur and M. K. Kazimierczuk, "DC-DC converters for electric vehicle applications," in *2007 Electrical Insulation Conference and Electrical Manufacturing Expo*, 2007, pp. 286-293.

[34] F. Sobrino-Manzanares and A. Garrigos, "Bidirectional, interleaved, multiphase, multidevice, soft-switching, FPGA-controlled, buck–boost converter with PWM real-time reconfiguration," *IEEE Transactions on Power Electronics,* vol. 33, no.11, pp. 9710-9721, 2018.

[35] Y. Du, X. Zhou, S. Bai, S. Lukic, and A. Huang, "Review of non-isolated bi-directional DC-DC converters for plug-in hybrid electric vehicle charge station application at municipal parking decks," in *2010 Twenty-Fifth Annual IEEE Applied Power Electronics Conference and Exposition (APEC)*, 2010, pp. 1145-1151.

[36] F. L. Tofoli, D. d. C. Pereira, W. J. d. Paula, and D. d. S. O. Júnior, "Survey on non-isolated high-voltage step-up dc-dc topologies based on the boost converter," *IET Power Electronics,* vol. 8, no.10, pp. 2044-2057, 2015.

[37] A. Adib, K. K. Afridi, M. Amirabadi, F. Fateh, M. Ferdowsi, B. Lehman*, et al.*, "E-Mobility—Advancements and Challenges," *IEEE Access,* vol. 7, pp. 165226-165240, 2019.

[38] J. C. Rosas-Caro, J. M. Ramirez, F. Z. Peng, and A. Valderrabano, "A DC-DC multilevel boost converter," *IET Power Electronics,* vol. 3, no.1, pp. 129-137, 2010.

[39] W. H. Martinez and C. A. Cortes, "High power density interleaved DC-DC converter for a high performance electric vehicle," in *2013 Workshop on Power Electronics and Power Quality Applications (PEPQA)*, 2013, pp. 1-6.

[40] R. Giral, L. Martinez-Salamero, and S. Singer, "Interleaved converters operation based on CMC," *IEEE Transactions on Power Electronics,* vol. 14, no.4, pp. 643-652, 1999.

[41] N. Liqin, D. J. Patterson, and J. L. Hudgins, "A high power, current sensorless, bi-directional, 16-phase interleaved, DC-DC converter for hybrid vehicle application," in *Energy Conversion Congress and Exposition (ECCE), 2010 IEEE*, 2010, pp. 3611-3617.

[42] O. Hegazy, R. Barrero, J. V. Mierlo, P. Lataire, N. Omar, and T. Coosemans, "An Advanced Power Electronics Interface for Electric Vehicles Applications," *IEEE Transactions on Power Electronics,* vol. 28, no.12, pp. 5508-5521, 2013.

[43] B. A. Miwa, D. M. Otten, and M. F. Schlecht, "High efficiency power factor correction using interleaving techniques," in *Applied Power Electronics Conference and Exposition, 1992. APEC '92. Conference Proceedings 1992., Seventh Annual*, 1992, pp. 557-568.

[44] L. Po-Wa, L. Yim-Shu, D. K. W. Cheng, and L. Xiu-Cheng, "Steady-state analysis of an interleaved boost converter with coupled inductors," *IEEE Transactions on Industrial Electronics,* vol. 47, no.4, pp. 787-795, 2000.

[45] W. Li and X. He, "Review of Nonisolated High-Step-Up DC/DC Converters in Photovoltaic Grid-Connected Applications," *IEEE Transactions on Industrial Electronics,* vol. 58, no.4, pp. 1239-1250, 2011.

[46] J. Czogalla, L. Jieli, and C. R. Sullivan, "Automotive application of multi-phase coupled-inductor DC-DC converter," in *38th IAS Annual Meeting on Conference Record of the Industry Applications Conference, 2003.*, 2003, pp. 1524-1529 vol.3.

[47] W. H. Martinez and C. A. Cortes, "High power density interleaved DC-DC converter for a high performance electric vehicle," in *Power Electronics and Power Quality Applications (PEPQA), 2013 Workshop on*, 2013, pp. 1-6.

[48] F. S. Garcia, J. A. Pomilio, and G. Spiazzi, "Modeling and Control Design of the Interleaved Double Dual Boost Converter," *IEEE Transactions on Industrial Electronics,* vol. 60, no.8, pp. 3283-3290, 2013.

[49] G. Calderon-Lopez, A. J. Forsyth, and D. R. Nuttall, "Design and Performance Evaluation of a 10-kW Interleaved Boost Converter for a Fuel Cell Electric Vehicle," in *Power Electronics and Motion Control Conference, 2006. IPEMC 2006. CES/IEEE 5th International*, 2006, pp. 1-5.

[50] O. Hegazy, J. V. Mierlo, and P. Lataire, "Analysis, Modeling, and Implementation of a Multidevice Interleaved DC/DC Converter for Fuel Cell Hybrid Electric Vehicles," *IEEE Transactions on Power Electronics,* vol. 27, no.11, pp. 4445-4458, 2012.

[51] M. Kabalo, D. Paire, B. Blunier, D. Bouquain, M. G. Simoes, and A. Miraoui, "Experimental Validation of High-Voltage-Ratio Low-Input-Current-Ripple Converters for Hybrid Fuel Cell Supercapacitor Systems," *IEEE Transactions on Vehicular Technology,* vol. 61, no.8, pp. 3430-3440, 2012.

[52] Y. Jang and M. M. Jovanovic, "New two-inductor boost converter with auxiliary transformer," *IEEE Transactions on Power Electronics,* vol. 19, no.1, pp. 169-175, 2004.

[53] C.-M. Lai, Y.-C. Lin, and D. Lee, "Study and Implementation of a Two-Phase Interleaved Bidirectional DC/DC Converter for Vehicle and DC-Microgrid Systems," *Energies,* vol. 8, no.9, pp. 9969-9991, 2015.

[54] M. Daouda, J. P. Trovao, R. G. Rubio, and M. C. Ta, "Comparison of Bidirectional Quasi Z-Source- and Bidirectional Conventional Two-Stage-Inverter for Electric Traction System," in *2018 IEEE Vehicle Power and Propulsion Conference (VPPC)*, 2018, pp. 1-6.

[55] P. S. Shenoy and P. T. Krein, "Local control of multiple module dc-dc converters," in *Control and Modeling for Power Electronics (COMPEL), 2010 IEEE 12th Workshop on*, 2010, pp. 1-6.

[56] H. Wen and B. Su, "Hybrid-mode interleaved boost converter design for fuel cell electric vehicles," *Energy Conversion and Management,* vol. 122, pp. 477-487, 2016.

[57] R. Saadi, M. Bahri, M. Y. Ayad, M. Becherif, O. Kraa, and A. Aboubou, "Dual Loop Control of Fuel Cell Source Using Non-isolated IBC-IDDB Converter for Hybrid Vehicle Applications," *Energy Procedia,* vol. 50, pp. 155-162, 2014/01/01 2014.

[58] O. Hegazy, R. Barrero, J. Van Mierlo, P. Lataire, N. Omar, and T. Coosemans, "An advanced power electronics interface for electric vehicles applications," *IEEE transactions on power electronics,* vol. 28, no.12, pp. 5508-5521, 2013.

[59] S. Yang, L. Chen, M. K. Alam, F. Xu, and Y. Zhou, "Switching Frequency Optimization of Boost Converter for HEV Applications," SAE Technical Paper 0148-7191, 2017.

[60] A. V. R. Ahmed M. Abou-Alfotouh, Hsueh-Rong Chang, and Craig Winterhalter, "A 1-MHz hard-switched silicon carbide DC-DC converter," *IEEE Transactions on Power Electronics,* vol. 21, no.4, pp. 880-889, 2006.

[61] R. L. Steigerwald, R. W. De Doncker, and H. Kheraluwala, "A comparison of high-power DC-DC soft-switched converter topologies," *IEEE transactions on industry applications,* vol. 32, no.5, pp. 1139-1145, 1996.

[62] R. C. N. Pilawa-Podgurski, A. D. Sagneri, J. M. Rivas, D. I. Anderson, and D. J. Perreault, "Very High Frequency Resonant Boost Converters," in *2007 IEEE Power Electronics Specialists Conference*, 2007, pp. 2718-2724.

[63] Y. Han, G. Cheung, A. Li, C. R. Sullivan, and D. J. Perreault, "Evaluation of magnetic materials for very high frequency power applications," *IEEE Transactions on Power Electronics,* vol. 27, no.1, pp. 425-435, 2011.

[64] K. V. Singh, H. O. Bansal, and D. Singh, "A comprehensive review on hybrid electric vehicles: architectures and components," *Journal of Modern Transportation,* vol. 27, no.2, pp. 77-107, 2019.

[65] A. Gattozzi, S. Strank, S. Pish, J. Herbst, R. Hebner, and F. Engelkemeir, "Power converter design options for the 12 kVdc bus system," in *Electric Ship Technologies Symposium (ESTS), 2017 IEEE*, 2017, pp. 246-250.

[66] D. Han and B. Sarlioglu, "Comprehensive study of the performance of SiC MOSFET-based automotive DC–DC converter under the influence of parasitic inductance," *IEEE Transactions on Industry Applications,* vol. 52, no.6, pp. 5100-5111, 2016.

[67] X. She, A. Q. Huang, Ó. Lucía, and B. Ozpineci, "Review of silicon carbide power devices and their applications," *IEEE Transactions on Industrial Electronics,* vol. 64, no.10, pp. 8193-8205, 2017.

[68] R. S. Yang, A. J. Hanson, B. A. Reese, C. R. Sullivan, and D. J. Perreault, "A low-loss inductor structure and design guidelines for high-frequency applications," *IEEE Transactions on Power Electronics,* 2019.

[69] K. O. Armstrong, S. Das, and J. Cresko, "Wide bandgap semiconductor opportunities in power electronics," in *2016 IEEE 4th Workshop on Wide Bandgap Power Devices and Applications (WiPDA)*, 2016, pp. 259-264.

[70] J. Schäfer, D. Bortis, and J. W. Kolar, "Optimal Design of Highly Efficient and Highly Compact PCB Winding Inductors," in *2018 IEEE 19th Workshop on Control and Modeling for Power Electronics (COMPEL)*, 2018, pp. 1-8.

[71] W. G. Hurley and W. H. Wölfle, *Transformers and inductors for power electronics: theory, design and applications*: John Wiley & Sons, 2013.

[72] Z. Dang and J. A. A. Qahouq, "Evaluation of High-Current Toroid Power Inductor With NdFeB Magnet for DC–DC Power Converters," *IEEE Transactions on Industrial Electronics,* vol. 62, no.11, pp. 6868-6876, 2015.

[73] S. Ahsanuzzaman, T. McRae, M. M. Peretz, and A. Prodic, "Low-volume buck converter with adaptive inductor core biasing," in *Applied Power Electronics Conference and Exposition (APEC), 2012 Twenty-Seventh Annual IEEE*, 2012, pp. 335-339.

[74] Y. Bi and D. C. Jiles, "Finite element modeling of an electrically variable inductor," *Magnetics, IEEE Transactions on,* vol. 35, no.5, pp. 3517-3519, 1999.

[75] M. Perdigao, J. Alonso, M. Dalla Costa, and E. Saraiva, "A variable inductor MATLAB/Simulink behavioral model for application in magnetically-controlled electronic ballasts," in *Power Electronics, Electrical Drives, Automation and Motion, 2008. SPEEDAM 2008. International Symposium on*, 2008, pp. 349-354.

[76] M. S. Perdigao, M. F. Menke, R. Seidel, R. A. Pinto, and J. M. Alonso, "A Review on Variable Inductors and Variable Transformers: Applications to Lighting Drivers," *IEEE Transactions on Industry Applications,* vol. 52, no.1, pp. 531-547, 2016.

[77] Y. Hu, L. Huber, and M. M. Jovanović, "Single-stage, universal-input AC/DC LED driver with current-controlled variable PFC boost inductor," *IEEE Transactions on Power Electronics,* vol. 27, no.3, pp. 1579-1588, 2012.

[78] C. W. Lufcy, "A survey of magnetic amplifiers," *Proceedings of the IRE,* vol. 43, no.4, pp. 404-413, 1955.

[79] J.-u. W. Hsu, A. P. Hu, A. Swain, X. Dai, and Y. Sun, "A new contactiess power pick-up with continuous variable inductor control using magnetic amplifier," in *2006 International Conference on Power System Technology*, 2006, pp. 1-8.

[80] V. S. Costa, M. S. Perdigão, A. S. Mendes, D. Abbes, and A. Aitouche, "Analysis and simulation of a LLC-VI resonant converter for solar applications," in *2017 52nd International Universities Power Engineering Conference (UPEC)*, 2017, pp. 1-6.

[81] L. Zhang, W. G. Hurley, and W. H. Wölfle, "A new approach to achieve maximum power point tracking for PV system with a variable inductor," *Power Electronics, IEEE Transactions on,* vol. 26, no.4, pp. 1031-1037, 2011.

[82] J. M. Alonso, M. A. Dalla Costa, M. Rico-Secades, J. Cardesin, and J. Garcia, "Investigation of a New Control Strategy for Electronic Ballasts Based on Variable Inductor," *Industrial Electronics, IEEE Transactions on,* vol. 55, no.1, pp. 3-10, 2008.

[83] H. Yuequan, L. Huber, Jovanovic, x, and M. M., "Single-Stage, Universal-Input AC/DC LED Driver With Current-Controlled Variable PFC Boost Inductor," *Power Electronics, IEEE Transactions on,* vol. 27, no.3, pp. 1579-1588, 2012.

[84] D. Medini and S. Ben-Yaakov, "A current-controlled variable-inductor for high frequency resonant power circuits," in *Applied Power Electronics Conference and Exposition, 1994. APEC'94. Conference Proceedings 1994., Ninth Annual*, 1994, pp. 219-225.

[85] J. M. Alonso, M. S. Perdigão, D. Gacio, L. Campa, and E. S. Saraiva, "Achieving constant frequency operation in DC-DC resonant converters through magnetic control," in *Energy Conversion Congress and Exposition (ECCE), 2010 IEEE*, 2010, pp. 2011-2018.

[86] A. Dimitrovski, Z. Li, and B. Ozpineci, "Applications of saturable-core reactors (SCR) in power systems," in *2014 IEEE PES T&D Conference and Exposition*, 2014, pp. 1-5.

[87] G. Tsolaridis and J. Biela, "Interleaved hybrid control concept for multiphase DC-DC converters," in *Energy Conversion Congress and Exposition (ECCE), 2017 IEEE*, 2017, pp. 3069-3076.

[88] J. Abu-Qahouq, H. Mao, and I. Batarseh, "Multiphase voltage-mode hysteretic controlled DC-DC converter with novel current sharing," *IEEE Transactions on Power Electronics,* vol. 19, no.6, pp. 1397-1407, 2004.

[89] S.-C. Tan, Y.-M. Lai, and K. T. Chi, "General design issues of sliding-mode controllers in DC–DC converters," *IEEE Transactions on Industrial Electronics,* vol. 55, no.3, pp. 1160-1174, 2008.

[90] B. Allaoua, B. Mebarki, and A. Laoufi, "A robust fuzzy sliding mode controller synthesis applied on boost DC-DC converter power supply for electric vehicle propulsion system," *International Journal of Vehicular Technology,* vol. 2013, 2013.

[91] H. Al-Baidhani and M. K. Kazimierczuk, "PWM-based proportional-integral sliding-mode current control of DC-DC boost converter," in *Texas Power and Energy Conference (TPEC), 2018 IEEE*, 2018, pp. 1-6.

[92] R.-J. Wai and L.-C. Shih, "Design of voltage tracking control for DC–DC boost converter via total sliding-mode technique," *IEEE Transactions on Industrial Electronics,* vol. 58, no.6, pp. 2502-2511, 2011.

[93] A. V. Sant and K. Rajagopal, "PM synchronous motor speed control using hybrid fuzzy-PI with novel switching functions," *IEEE Transactions on Magnetics,* vol. 45, no.10, pp. 4672-4675, 2009.

[94] A. V. Sant and K. R. Rajagopal, "PM Synchronous Motor Speed Control Using Hybrid Fuzzy-PI With Novel Switching Functions," *IEEE Transactions on Magnetics,* vol. 45, no.10, pp. 4672-4675, 2009.

[95] W. Xiao, H. Wen, and H. Zeineldin, "Affine parameterization and anti-windup approaches for controlling DC-DC converters," in *Industrial Electronics (ISIE), 2012 IEEE International Symposium on*, 2012, pp. 154-159.

[96] W. Xiao and P. Zhang, "Photovoltaic voltage regulation by affine parameterization," *International journal of green energy,* vol. 10, no.3, pp. 302-320, 2013.

[97] G. C. Goodwin, S. F. Graebe, and M. E. Salgado, "Control system design," *Upper Saddle River,* 2001.

[98] J. Kan, Y. Wu, Y. Tang, S. Xie, and L. Jiang, "Hybrid Control Scheme for Photovoltaic Micro-Inverter with Adaptive Inductor," *IEEE Transactions on Power Electronics,* 2018.

[99] J. M. Alonso, M. S. Perdig, J. Ribas, D. Gacio, and E. S. Saraiva, "Optimizing Universal Ballasts Using Magnetic Regulators and Digital Control," *IEEE Transactions on Industrial Electronics,* vol. 58, no.7, pp. 2860-2871, 2011.

[100] M. S. Perdigao, J. M. Alonso, M. A. D. Costa, and E. S. Saraiva, "A variable inductor MATLAB/Simulink behavioral model for application in magnetically-controlled electronic ballasts," in *Power Electronics, Electrical Drives, Automation and Motion, 2008. SPEEDAM 2008. International Symposium on*, 2008, pp. 349-354.

[101] F. Machado, J. P. F. Trovão, and C. H. Antunes, "Effectiveness of Supercapacitors in Pure Electric Vehicles Using a Hybrid Metaheuristic Approach," *IEEE Transactions on Vehicular Technology,* vol. 65, no.1, pp. 29-36, 2016.

[102] O. C. Onar, J. Kobayashi, D. C. Erb, and A. Khaligh, "A Bidirectional High-Power-Quality Grid Interface With a Novel Bidirectional Noninverted Buck–Boost Converter for PHEVs," *IEEE Transactions on Vehicular Technology,* vol. 61, no.5, pp. 2018-2032, 2012.

[103] R. d. Castro, R. E. Araujo, J. P. F. Trovao, P. G. Pereirinha, P. Melo, and D. Freitas, "Robust DC-Link Control in EVs With Multiple Energy Storage Systems," *IEEE Transactions on Vehicular Technology,* vol. 61, no.8, pp. 3553-3565, 2012.

[104] Y. Cho and J. S. Lai, "High-Efficiency Multiphase DC-DC Converter for Fuel-Cell-Powered Truck Auxiliary Power Unit," *IEEE Transactions on Vehicular Technology,* vol. 62, no.6, pp. 2421-2429, 2013.

[105] D. Han, J. Noppakunkajorn, and B. Sarlioglu, "Comprehensive Efficiency, Weight, and Volume Comparison of SiC- and Si-Based Bidirectional DC-DC Converters for Hybrid Electric Vehicles," *IEEE Transactions on Vehicular Technology,* vol. 63, no.7, pp. 3001-3010, 2014.

[106] Z. Dang and J. A. Abu Qahouq, "Evaluation of High Current Toroid Power Inductor with NdFeB Magnet for DC-DC Power Converters," *Industrial Electronics, IEEE Transactions on,* vol. PP, no.99, pp. 1-1, 2015.

[107] L. Reuben, *Electronic Transformers and Circuits*: New York; Chapman & Hall: London, 1947.

[108] S. M. Ahsanuzzaman, T. McRae, M. M. Peretz, and A. Prodić, "Low-volume buck converter with adaptive inductor core biasing," in *2012 Twenty-Seventh Annual IEEE Applied Power Electronics Conference and Exposition (APEC)*, 2012, pp. 335-339.

[109] M. Hirakawa, Y. Watanabe, M. Nagano, K. Andoh, S. Nakatomi, S. Hashino*, et al.*, "High power DC/DC converter using extreme close-coupled inductors aimed for electric vehicles," in *Power Electronics Conference (IPEC), 2010 International*, 2010, pp. 2941-2948.

[110] S. m. Dwari and L. Parsa, "A Novel High Efficiency High Power Interleaved Coupled-Inductor Boost DC-DC Converter for Hybrid and Fuel Cell Electric Vehicle," in *2007 IEEE Vehicle Power and Propulsion Conference*, 2007, pp. 399-404.

[111] J. M. Alonso, M. S. Perdigão, J. Ribas, D. Gacio, and E. S. Saraiva, "Optimizing Universal Ballasts Using Magnetic Regulators and Digital Control," *IEEE Transactions on Industrial Electronics,* vol. 58, no.7, pp. 2860-2871, 2011.

[112] A. S. Kislovski, "Quasi-linear controllable inductor," *Proceedings of the IEEE,* vol. 75, no.2, pp. 267-269, 1987.

[113] Y. Hu, L. Huber, and M. Jovanović, "Current-controlled variable inductor," ed: Google Patents, 2012.

[114] E. Rozanov and S. Ben-Yaakov, "A SPICE behavioral model for current-controlled magnetic inductors," in *Electrical and Electronics Engineers in Israel, 2004. Proceedings. 2004 23rd IEEE Convention of*, 2004, pp. 338-341.

[115] R. Kadri, J. P. Gaubert, and G. Champenois, "An Improved Maximum Power Point Tracking for Photovoltaic Grid-Connected Inverter Based on Voltage-Oriented Control," *IEEE Transactions on Industrial Electronics,* vol. 58, no.1, pp. 66-75, 2011.

[116] S. Barg, K. Ammous, H. Mejbri, and A. Ammous, "An improved empirical formulation for magnetic core losses estimation under nonsinusoidal induction," *IEEE Transactions on Power Electronics,* vol. 32, no.3, pp. 2146-2154, 2017.

[117] J. D. V. Wyk and F. C. Lee, "On a Future for Power Electronics," *IEEE Journal of Emerging and Selected Topics in Power Electronics,* vol. 1, no.2, pp. 59-72, 2013.

[118] D. Heredero-Peris and S. Galceran-Arellano, "Design methodology for a dc–dc power conversion system with EIS capability for battery packs," *Simulation Modelling Practice and Theory,* vol. 87, pp. 15-34, 2018.

[119] A. J. Hanson, J. A. Belk, S. Lim, C. R. Sullivan, and D. J. Perreault, "Measurements and performance factor comparisons of magnetic materials at high frequency," *IEEE Transactions on Power Electronics,* vol. 31, no.11, pp. 7909-7925, 2016.

[120] M. S. Rylko, B. J. Lyons, J. G. Hayes, and M. G. Egan, "Revised magnetics performance factors and experimental comparison of high-flux materials for high-current DC–DC inductors," *IEEE Transactions on Power Electronics,* vol. 26, no.8, pp. 2112-2126, 2011.

[121] M. S. Perdigão, M. Menke, A. Seidel, R. A. Pinto, and J. M. Alonso, "A review on variable inductors and variable transformers: Applications to lighting drivers," *IEEE Transactions on Industry Applications,* vol. 52, no.1, pp. 531-547, 2016.

[122] O. Ichinokura, T. Kagami, T. Jinzenji, M. Maeda, and Y. Wakiya, "High speed variable-inductor controlled with DC-DC converter," *IEEE transactions on magnetics,* vol. 31, no.6, pp. 4247-4249, 1995.

[123] J. D. Pollock, W. Lundquist, and C. R. Sullivan, "Predicting inductance roll-off with DC excitations," in *2011 IEEE Energy Conversion Congress and Exposition*, 2011, pp. 2139-2145.

[124] G. R. C. Mouli, J. Schijffelen, P. Bauer, and M. Zeman, "Estimation of ripple and inductance roll off when using powdered iron core inductors," in *PCIM Europe 2016; International Exhibition and Conference for Power Electronics, Intelligent Motion, Renewable Energy and Energy Management*, 2016, pp. 1-8.

[125] M. Luo, D. Dujic, and J. Allmeling, "Modeling Frequency Independent Hysteresis Effects of Ferrite Core Materials Using Permeance–Capacitance Analogy for System-Level Circuit Simulations," *IEEE Transactions on Power Electronics,* vol. 33, no.12, pp. 10055-10070, 2018.

[126] G. Di Capua and N. Femia, "A novel method to predict the real operation of ferrite inductors with moderate saturation in switching power supply applications," *IEEE Transactions on Power Electronics,* vol. 31, no.3, pp. 2456-2464, 2015.

[127] J. M. Alonso, G. Martínez, M. Perdigão, M. R. Cosetin, and R. N. d. Prado, "A Systematic Approach to Modeling Complex Magnetic Devices Using SPICE: Application to Variable Inductors," *IEEE Transactions on Power Electronics,* vol. 31, no.11, pp. 7735-7746, 2016.

[128] S. Sezen, E. Karakas, K. Yilmaz, and M. Ayaz, "Finite element modeling and control of a high-power SRM for hybrid electric vehicle," *Simulation Modelling Practice and Theory,* vol. 62, pp. 49-67, 2016.

[129] S. D. Sudhoff, G. M. Shane, and H. Suryanarayana, "Magnetic-equivalent-circuit-based scaling laws for low-frequency magnetic devices," *IEEE Transactions on Energy Conversion,* vol. 28, no.3, pp. 746-755, 2013.

[130] S. Ouagued, Y. Amara, and G. Barakat, "Comparison of hybrid analytical modelling and reluctance network modelling for pre-design purposes," *Mathematics and Computers in Simulation,* vol. 130, pp. 3-21, 2016.

[131] X. Chen, J. Hu, K. Chen, and Z. Peng, "Modeling of electromagnetic torque considering saturation and magnetic field harmonics in permanent magnet synchronous motor for HEV," *Simulation Modelling Practice and Theory,* vol. 66, pp. 212-225, 2016.

[132] M. Eslamian, B. Vahidi, and S. H. Hosseinian, "Combined analytical and FEM methods for parameters calculation of detailed model for dry-type transformer," *Simulation Modelling Practice and Theory,* vol. 18, no.3, pp. 390-403, 2010/03/01/ 2010.

[133] M. Mu, F. Zheng, Q. Li, and F. C. Lee, "Finite element analysis of inductor core loss under DC bias conditions," *IEEE Transactions on Power electronics,* vol. 28, no.9, pp. 4414-4421, 2013.

[134] R. A. Salas and J. Pleite, "Simulation of Waveforms of a Ferrite Inductor with Saturation and Power Losses," *Materials,* vol. 7, no.3, pp. 1850-1865, 2014.

[135] Y. Su, Q. Li, and F. C. Lee, "FEA modeling of the low profile coupled inductor with non-uniform flux distribution," in *Applied Power Electronics Conference and Exposition (APEC), 2013 Twenty-Eighth Annual IEEE*, 2013, pp. 2416-2423.

[136] A. M. Knight and J. Salmon, "3D finite element analysis of coupled inductors for multilevel inverter output," in *Electromagnetic Field Computation (CEFC), 2010 14th Biennial IEEE Conference on*, 2010, pp. 1-1.

[137] Y. Bi and D. C. Jiles, "Finite element modeling of an electrically variable inductor," *IEEE Transactions on Magnetics,* vol. 35, no.5, pp. 3517-3519, 1999.

[138] M. S. Perdigão, S. Ferreira, M. Martins, A. Mendes, and J. M. Alonso, "Finite element analysis of a variable inductor for an RSCC based LED lamp driver," in *Industry Applications Society Annual Meeting, 2015 IEEE*, 2015, pp. 1-8.

[139] M. W. Beraki, J. P. F. Trovão, M. S. Perdigão, and M. R. Dubois, "Variable Inductor Based Bidirectional DC–DC Converter for Electric Vehicles," *IEEE Transactions on Vehicular Technology,* vol. 66, no.10, pp. 8764-8772, 2017.

[140] F. Fouad, T. Nehl, and N. Demerdash, "Saturated transformer inductances determined by energy perturbation techniques," *IEEE Transactions on Power Apparatus and Systems,* no.11, pp. 4185-4193, 1982.

[141] A. EPCOS, "Ferrites and accessories-SIFERRIT material N87," *Data Sheet, September,* 2006.

[142] R. Escarela-Perez, E. Campero-Littlewood, M. A. Arjona-Lopez, and A. Laureano-Cruces, "Comparison of two techniques for two-dimensional finite-element inductance computation of electrical machines," *IEE Proceedings - Electric Power Applications,* vol. 152, no.4, pp. 855-861, 2005.

[143] J. Li, T. Abdallah, and C. R. Sullivan, "Improved calculation of core loss with nonsinusoidal waveforms," in *Conference Record of the 2001 IEEE Industry Applications Conference. 36th IAS Annual Meeting (Cat. No. 01CH37248)*, 2001, pp. 2203-2210.

[144] J. Muhlethaler, J. Biela, J. W. Kolar, and A. Ecklebe, "Improved core-loss calculation for magnetic components employed in power electronic systems," *IEEE Transactions on Power electronics,* vol. 27, no.2, pp. 964-973, 2011.

[145] J. Reinert, A. Brockmeyer, and R. W. De Doncker, "Calculation of losses in ferro-and ferrimagnetic materials based on the modified Steinmetz equation," *IEEE Transactions on Industry applications,* vol. 37, no.4, pp. 1055-1061, 2001.

[146] J. Biela, U. Badstuebner, and J. W. Kolar, "Impact of power density maximization on efficiency of DC-DC converter systems," *IEEE Transactions on Power Electronics,* vol. 24, no.1, pp. 288-300, 2009.

[147] D. W. Kim, H. Cha, S. H. Lee, and D. H. Kim, "Characteristic of a Variable Inductor Using Magnetorheological Fluid for Efficient Power Conversion," *IEEE Transactions on Magnetics,* vol. 49, no.5, pp. 1901-1904, 2013.

[148] P. Wallmeier, "Improved analytical modeling of conductive losses in gapped high-frequency inductors," *IEEE Transactions on Industry Applications,* vol. 37, no.4, pp. 1045-1054, 2001.

[149] A. W. Lotfi and M. A. Wilkowski, "Issues and advances in high-frequency magnetics for switching power supplies," *Proceedings of the IEEE,* vol. 89, no.6, pp. 833-845, 2001.

[150] V. Monteiro, J. Pinto, B. Exposto, L. F. Monteiro, C. Couto, and J. L. Afonso, "A novel concept of unidirectional bridgeless combined boost-buck converter for EV battery

chargers," in *2015 IEEE 24th International Symposium on Industrial Electronics (ISIE)*, 2015, pp. 190-195.

[151] H. Ye, P. Magne, B. Bilgin, S. Wirasingha, and A. Emadi, "A comprehensive evaluation of bidirectional boost converter topologies for electrified vehicle applications," in *Industrial Electronics Society, IECON 2014-40th Annual Conference of the IEEE*, 2014, pp. 2914-2920.

[152] V. Leonavicius, M. Duffy, U. Boeke, and S. Mathuna, "Comparison of realization techniques for PFC inductor operating in discontinuous conduction mode," *IEEE Transactions on Power Electronics,* vol. 19, no.2, pp. 531-541, 2004.

[153] O. Ichinokura, T. Kagami, T. Jinzenji, M. Maeda, and Y. Wakiya, "High speed variable-inductor controlled with DC-DC converter," *Magnetics, IEEE Transactions on,* vol. 31, no.6, pp. 4247-4249, 1995.

[154] J. P. F. Trovão, M.-A. Roux, É. Ménard, and M. R. Dubois, "Energy-and power-split management of dual energy storage system for a three-wheel electric vehicle," *IEEE Transactions on Vehicular Technology,* vol. 66, no.7, pp. 5540-5550, 2017.

[155] J. M. Alonso, M. A. Dalla Costa, M. Rico-Secades, J. Cardesin, and J. Garcia, "Investigation of a new control strategy for electronic ballasts based on variable inductor," *IEEE Transactions on Industrial Electronics,* vol. 55, no.1, pp. 3-10, 2008.

[156] C. W. T. McLyman, *Transformer and inductor design handbook*: CRC press, 2016.

[157] R. W. Erickson and D. Maksimovic, *Fundamentals of power electronics*: Springer Science & Business Media, 2007.

[158] H. Chen, H. Kim, R. Erickson, and D. Maksimović, "Electrified automotive powertrain architecture using composite DC–DC converters," *IEEE Transactions on Power Electronics,* vol. 32, no.1, pp. 98-116, 2016.

[159] A. Hilal and B. Cougo, "Optimal inductor design and material selection for high power density inverters used in aircraft applications," in *Electrical Systems for Aircraft, Railway, Ship Propulsion and Road Vehicles & International Transportation Electrification Conference (ESARS-ITEC), International Conference on*, 2016, pp. 1-6.

[160] J. McLean, "Inductor design using amorphous metal C-cores," *IEEE Circuits and Devices Magazine,* vol. 12, no.5, pp. 26-30, 1996.

[161] P. Ohodnicki, A. Leary, M. E. McHenry, G. Nojima, and A. Hefner, "State-of-the-art of HF soft magnetics and HV/UHV silicon carbide semiconductors," in *PCIM Europe 2016; International Exhibition and Conference for Power Electronics, Intelligent Motion, Renewable Energy and Energy Management*, 2016, pp. 1-10.

[162] D. Schumacher, B. Bilgin, and A. Emadi, "Inductor design for multiphase bidirectional DC-DC boost converter for an EV/HEV application," in *Transportation Electrification Conference and Expo (ITEC), 2017 IEEE*, 2017, pp. 221-228.

[163] C. R. Sullivan, "Prospects for advances in power magnetics," in *CIPS 2016; 9th International Conference on Integrated Power Electronics Systems; Proceedings of*, 2016, pp. 1-9.

[164] H. Matsumori, T. Shimizu, X. Wang, and F. Blaabjerg, "A Practical Core Loss Model for Filter Inductors of Power Electronic Converters," *IEEE Journal of Emerging and Selected Topics in Power Electronics,* vol. 6, no.1, pp. 29-39, 2018.

[165] M. Mu, "High frequency magnetic core loss study," Virginia Polytechnic Institute and State University, 2013.

[166] C. W. T. McLyman and C. W. T. McLyman, *Magnetic core selection for transformers and inductors: a user's guide to practice and specification*: M. Dekker, 1997.

[167] W. Shen, F. Wang, D. Boroyevich, and C. W. Tipton, "Loss characterization and calculation of nanocrystalline cores for high-frequency magnetics applications," *IEEE Transactions on Power Electronics,* vol. 23, no.1, pp. 475-484, 2008.

[168] Magnetics. *Powder Core Loss Calculation*. Available: https://www.mag-inc.com/Design/Design-Guides/Powder-Core-Loss-Calculation

[169] Y. Wang, G. Calderon-Lopez, and A. J. Forsyth, "High-Frequency Gap Losses in Nanocrystalline Cores," *IEEE Transactions on Power Electronics,* vol. 32, no.6, pp. 4683-4690, 2017.

[170] S. Maniktala, *Switching power supply design & optimization*: McGraw-Hill, Inc., 2004.

[171] Y. Liu, K.-Y. See, S. Yin, R. Simanjorang, C. F. Tong, A. Nawawi*, et al.*, "LCL Filter Design of a 50-kW 60-kHz SiC Inverter with Size and Thermal Considerations for Aerospace Applications," *IEEE transactions on Industrial Electronics,* vol. 64, no.10, pp. 8321-8333, 2017.

[172] A. Goldman, *Magnetic components for power electronics*: Springer Science & Business Media, 2012.

[173] X. She, X. Yu, F. Wang, and A. Q. Huang, "Design and demonstration of a 3.6-kV–120-V/10-kVA solid-state transformer for smart grid application," *IEEE Transactions on Power Electronics,* vol. 29, no.8, pp. 3982-3996, 2014.

[174] S. Kimura, Y. Itoh, W. Martinez, M. Yamamoto, and J. Imaoka, "Downsizing effects of integrated magnetic components in high power density DC–DC converters for EV and HEV applications," *IEEE Transactions on Industry Applications,* vol. 52, no.4, pp. 3294-3305, 2016.

[175] J. Biela, M. Schweizer, S. Waffler, and J. W. Kolar, "SiC versus Si—Evaluation of potentials for performance improvement of inverter and DC–DC converter systems by SiC power semiconductors," *IEEE transactions on industrial electronics,* vol. 58, no.7, pp. 2872-2882, 2011.

[176] O. Gutfleisch, M. A. Willard, E. Brück, C. H. Chen, S. Sankar, and J. P. Liu, "Magnetic materials and devices for the 21st century: stronger, lighter, and more energy efficient," *Advanced materials,* vol. 23, no.7, pp. 821-842, 2011.

[177] Q. Li, M. Lim, J. Sun, A. Ball, Y. Ying, F. C. Lee*, et al.*, "Technology road map for high frequency integrated DC-DC converter," in *Applied Power Electronics Conference and Exposition (APEC), 2010 Twenty-Fifth Annual IEEE*, 2010, pp. 533-539.

[178] B.-G. You, J.-S. Kim, B.-K. Lee, G.-B. Choi, and D.-W. Yoo, "Optimization of powder core inductors of buck-boost converters for hybrid electric vehicles," in *Vehicle Power and Propulsion Conference, 2009. VPPC'09. IEEE*, 2009, pp. 730-735.

[179] A. Krings, A. Boglietti, A. Cavagnino, and S. Sprague, "Soft magnetic material status and trends in electric machines," *IEEE transactions on industrial electronics,* vol. 64, no.3, pp. 2405-2414, 2017.

[180] D. Rahman, A. J. Morgan, Y. Xu, R. Gao, W. Yu, D. C. Hopkins*, et al.*, "Design methodology for a planarized high power density EV/HEV traction drive using SiC power modules," in *Energy Conversion Congress and Exposition (ECCE), 2016 IEEE*, 2016, pp. 1-7.

[181] Y. Itoh, S. Kimura, J. Imaoka, and M. Yamamoto, "Inductor loss analysis of various materials in interleaved boost converters," in *2014 IEEE Energy Conversion Congress and Exposition (ECCE)*, 2014, pp. 980-987.

[182] M. S. Rylko, J. G. Hayes, and M. G. Egan, "Experimental investigation of high-flux density magnetic materials for high-current inductors in hybrid-electric vehicle DC-DC converters," in *2010 IEEE Vehicle Power and Propulsion Conference*, 2010, pp. 1-7.

[183] M. Gerber, J. Ferreira, I. Hofsajer, and N. Seliger, "A very high density, heatsink mounted inductor for automotive applications," in *Industry Applications Conference, 2002. 37th IAS Annual Meeting. Conference Record of the*, 2002, pp. 948-954.

[184] W. Yu, H. Qian, and J.-S. Lai, "Design of high-efficiency bidirectional DC–DC converter and high-precision efficiency measurement," *IEEE Transactions on Power Electronics,* vol. 25, no.3, pp. 650-658, 2010.

[185] N. Igarashi, M. Uozumi, T. Kosuge, A. Sato, K. Kusawake, and K. YAMAGUCHI, "Pure Iron Based Soft Magnetic Composite Core that Enables Downsizing Automotive Reactors," *SEI Technical Review,* no.186, pp. 92-97, 2015.

[186] T. Salem, D. Urciuoli, V. Lubomirsky, and G. Ovrebo, "Design considerations for high power inductors in dc-dc converters," in *Applied Power Electronics Conference, APEC 2007-Twenty Second Annual IEEE*, 2007, pp. 1258-1263.

[187] M. Pavlovsky, G. Guidi, and A. Kawamura, "Assessment of coupled and independent phase designs of interleaved multiphase buck/boost DC-DC converter for EV power train," *IEEE Transactions on Power Electronics,* vol. 29, no.6, pp. 2693-2704, 2014.

[188] M. Pavlovsky, Y. Tsuruta, and A. Kawamura, "Automotive DC-DC converter designed for high power-density and high efficiency," in *Integrated Power Systems (CIPS), 2008 5th International Conference on*, 2008, pp. 1-5.

[189] M. Pavlovsky, Y. Tsuruta, and A. Kawamura, "Recent improvements of efficiency and power density of DC-DC converters for automotive applications," in *Power Electronics Conference (IPEC), 2010 International*, 2010, pp. 1866-1873.

[190] M. Pavlovsky, Y. Tsuruta, and A. Kawamura, "Fully bi-directional dc-dc converter for EV power train with power density of 40 kW/l," in *Energy Conversion Congress and Exposition, 2009. ECCE 2009. IEEE*, 2009, pp. 1768-1774.

[191] A. Kawamura, M. Pavlovsky, and Y. Tsuruta, "State-of-the-art high power density and high efficiency DC-DC chopper circuits for HEV and FCEV applications," in *Proc of IEEE Power Electronics and Motion Control Conference (EPE-PEMC 2008)*, 2008, pp. 7-20.

[192] J. Elmes, "High-density And High-efficiency Soft Switching Modular Bi-directional Dc-dc Converter For Hybrid Electric Vehicles," 2010.

[193] J. Elmes, R. Kersten, I. Batarseh, M. Pepper, and K. Mansfield, "Modular bidirectional DC-DC converter for hybrid/electric vehicles with variable-frequency interleaved soft-switching," in *Vehicle Power and Propulsion Conference, 2009. VPPC'09. IEEE*, 2009, pp. 448-454.

[194] D. Urciuoli and T. Salem, "New Nanocrystalline Core Performance Versus Finemet (Registered) for High-power Inductors," ARMY RESEARCH LAB ADELPHI MD2008.

[195] G. Sarriegui, S. Beushausen, and R. W. De Doncker, "Comparison of high frequency inductors for bidirectional DC-DC converters for electric vehicles," in *Power Electronics and Applications (EPE'16 ECCE Europe), 2016 18th European Conference on*, 2016, pp. 1-8.

[196] H. Kim, H. Chen, D. Maksimovic, and R. Erickson, "Design of a high efficiency 30 kw boost composite converter," in *Energy Conversion Congress and Exposition (ECCE), 2015 IEEE*, 2015, pp. 4243-4250.

[197] B.-G. You, B.-K. Lee, S.-W. Lee, M.-C. Jeong, J.-h. Kim, and I.-B. Jeong, "Improvement of the thermal flow with potting structured inductor for high power density in 40kW DC-DC converter," in *Vehicle Power and Propulsion Conference (VPPC), 2012 IEEE*, 2012, pp. 1027-1032.

[198] B.-G. You, S.-W. Lee, G.-B. Choi, D.-W. Yoo, and B.-k. Lee, "Comparison of simulation and experimental results for Mega Flux inductors in hybrid electric vehicles," in *Power Electronics and ECCE Asia (ICPE & ECCE), 2011 IEEE 8th International Conference on*, 2011, pp. 1950-1957.

[199] M. Mu and F. C. Lee, "Comparison and selection of magnetic materials for coupled inductor used in interleaved three-level multi-phase DC-DC converters," in *Energy Conversion Congress and Exposition (ECCE), 2015 IEEE*, 2015, pp. 3529-3534.

[200] M. S. Rylko, K. J. Hartnett, J. G. Hayes, and M. G. Egan, "Magnetic material selection for high power high frequency inductors in dc-dc converters," in *Applied Power Electronics Conference and Exposition, 2009. APEC 2009. Twenty-Fourth Annual IEEE*, 2009, pp. 2043-2049.

[201] S. M. Alloys. (12 February 2019). *Simplified Method Of Selecting Soft Magnetic Alloys*.

[Online]. Available: http://www.softmagneticalloy.com/selecting_soft_magnetic_alloys.html. [Accessed: 12-Feb-2019].

[202] B. D. Cullity and C. D. Graham, *Introduction to magnetic materials*: John Wiley & Sons, 2011.

[203] H. Gavrila and V. Ionita, "Crystalline and amorphous soft magnetic materials and their applications- status of art and challenges," *Journal of Optoelectronics and Advanced Materials(Romania),* vol. 4, no.2, pp. 173-192, 2002.

[204] H. Lu, Y. Guo, J. Zhu, J. Zhong, and J. Jin, "Soft Magnetic Materials for High Frequency High Power Density Transformers in Power Electronic Systems," *Academic Magazine,* 2007.

[205] Micrometals. *Technical Bulletin High Frequency Sendust Material*. [Online]. Available: www.micrometalsarnoldpowdercores.com/upload/HighFrequencySendustTechnicalBulletin.[1].pdf. [Accessed: 03-Jul-2018].

[206] G. T. Nikolov and V. C. Valchev, "Nanocrystalline magnetic materials versus ferrites in power electronics," *Procedia Earth and Planetary Science,* vol. 1, no.1, pp. 1357-1361, 2009.

[207] C. C. WeymanLundquist.. *A Fresh Look at Design of Buck and Boost inductors for SMPS Converters*. [Online].Available: https://www.wcmagnetics.com/wp-content/uploads/2015/04/Boost-Inductor-Design.pdf.[Accessed: 25-Apr-2019].

[208] Y. Liu, H. A. Mantooth, J. C. Balda, and C. Farnell, "A Variable Inductor BasedLCLFilter for Large-Scale Microgrid Application," *IEEE Transactions on Power Electronics,* vol. 33, no.9, 2018.

[209] W. G. Hurley and W. H. Wölfle, *Transformers and inductors for power electronics: theory, design and applications*: John Wiley & Sons, 2013.

[210] A. Kouchaki and M. Nymand, "High efficiency three-phase power factor correction rectifier using SiC switches," in *Power Electronics and Applications (EPE'17 ECCE Europe), 2017 19th European Conference on*, 2017, pp. P. 1-P. 10.

[211] M. A. Swihart. *Inductor Cores – Material and Shape Choices*. [Online]. Available: https://www.mag-inc.com/getattachment/Design/Design-Guides/Inductor-Cores-Material-and-Shape-Choices/Inductor-Cores-Material-and-Shape-Choices-08142013.pdf?lang=en-US [Accessed: 20-Mar-2019].

[212] J. Imaoka, K. Okamoto, M. Shoyama, Y. Ishikura, M. Noah, and M. Yamamoto, "Modeling, Magnetic Design, Simulation Methods, and Experimental Evaluation of Various Powder Cores Used in Power Converters Considering Their DC Superimposition Characteristics," *IEEE Transactions on Power Electronics,* 2018.

[213] R. MBK, "Review on magnetic components: Design & consideration in VHF circuit applications," *Journal of Power Electronics,* vol. 9, no.2, pp. 180-187, 2009.

[214] J. Cros, P. Viarouge, and M. T. Kakhki, "Design and optimization of soft magnetic composite machines with finite element methods," *IEEE Transactions on Magnetics,* vol. 47, no.10, pp. 4384-4390, 2011.

[215] A. Schoppa, P. Delarbre, and A. Schatz, "Optimal use of soft magnetic powder composites (SMC) in electric machines," in *Proceedings of the 2013 International Conference on Powder Metallurgy & Particulate Materials*, 2013.

[216] M. Kącki, M. S. Rylko, J. G. Hayes, and C. R. Sullivan, "Magnetic material selection for EMI filters," in *Energy Conversion Congress and Exposition (ECCE), 2017 IEEE*, 2017, pp. 2350-2356.

[217] S. I. Components. *Choice of the Magnetic Core*. [Online]. Available: http://www.sirio-ic.com/index.php/en/i-magneticore-en.html. [Accessed: 26-Jan- 2018].

[218] MSTATOR. *Amorphous and nanocrystalline soft magnetic alloys*. [Online].Available: http://en.mstator.ru/products/amorf. [Accessed: 02-Feb- 2018]

[219] T. Oda, S. Miyazaki, and E. Shimazu, "The Reactor Core for HEV Boost Converter," *NTN TECHNICAL REVIEW,* no.81, pp. 46-51, 2013.

[220] A. Stadler, T. Stolzke, and C. Gulden, "Optimized filter inductors for a 1MW windmill demonstrator with an objective to reduced converter size," in *Power Electronics and Applications (EPE'15 ECCE-Europe), 2015 17th European Conference on*, 2015, pp. 1-6.

[221] M. Pavlovsky, S. W. H. de Haan, and J. A. Ferreira, "Reaching high power density in multikilowatt DC–DC converters with galvanic isolation," *IEEE transactions on Power Electronics,* vol. 24, no.3, pp. 603-612, 2009.

[222] M. A. Willard, "Stronger, lighter, and more energy efficient: Challenges of magnetic material development for vehicle electrification," *Frontiers of Engineering,* 2013.

[223] A. BFi. *A user guide to soft magnetic materials (part 2 of 4)*. [Online]. Available: http://52ebad10ee97eea25d5e-d7d40819259e7d3022d9ad53e3694148.r84.cf3.rackcdn.com/Acal_BFi_user_guide_to_soft_magnetic_materials_part_2.pdf. [Accessed: 24-Jan- 2018]

[224] H. Sheng, W. Shen, H. Wang, D. Fu, Y. Pei, X. Yang*, et al.*, "Design and implementation of a high power density three-level parallel resonant converter for capacitor charging pulsed-power supply," *IEEE Transactions on Plasma Science,* vol. 39, no.4, pp. 1131-1140, 2011.

[225] K. Mueller and R. Heinrich, "Modern high voltage drive train architecture to accommodate the needs for a variety of components for future automotive applications," in *CoFAT*, 2013.

[226] m. o. t. CWS Coil Winding Specialist, inductors, coils and chokes. *Application Notes: How To Select And Use Ferrite/Nanocrystalline Common Mode Chokes* [Online]. Available: http://www.coilws.com/index.php?main_page=index&cPath=208_211_250. [Accessed: 08-Jan- 2019]

[227] M. A. Willard, "Stronger, lighter, and more energy efficient: Challenges of magnetic material development for vehicle electrification," in *Frontiers of Engineering; Reports on Leading-Edge Engineering from the 2012 Symposium, National Academy of Engineering*, 2013.

[228] A. M. Leary, P. R. Ohodnicki, and M. E. McHenry, "Soft magnetic materials in high-frequency, high-power conversion applications," *Jom,* vol. 64, no.7, pp. 772-781, 2012.

[229] K. Senda, M. Namikawa, and Y. Hayakawa, "Electrical steels for advanced automobiles–core materials for motors, generators and high-frequency reactors," *JFE Steel Research Department, Tokyo, Tech. Rep,* vol. 4, 2004.

[230] (11 March 2019). *Hybrid cars & Electric cars*. [Online]. Available: https://www.hitachimetals.com/automotive-related/automotive-components-materials/documents/HEV_EV.pdf. [Accessed: 11-Mar-2019]

[231] C. S. Corporation. *Innovative Technological Advancements MAGNETIC POWDER CORES.* [Online]. Available: http://www.mhw-intl.com/assets/CSC/CSC_Catalog.pdf.[Accessed: 20-Feb-2018]

[232] B. J. Lyons, J. G. Hayes, and M. G. Egan, "Design algorithm for high-current gapped foil-wound inductors in low-to-medium frequency dc-dc converters," in *Power Electronics Specialists Conference, 2007. PESC 2007. IEEE*, 2007, pp. 1760-1766.

[233] A. M. Technologies. (2015, 15 January 2019). *Soft Magnetic Applications Guide*. [Online]. Available: www.arnoldmagnetics.com. [Accessed: 15-Jan-2019]

[234] J. S. Corporation. *Super Core TM Electrical steel sheets for high-frequency application*. [Online]. Available: http://www.jfe-steel.co.jp/en/products/electrical/catalog/f1e-002.pdf [Accessed: 22-Feb-2018]

[235] E. P. Wohlfarth, *Ferromagnetic materials: a handbook on the properties of magnetically ordered substances* vol. 2: Elsevier, 1980.

[236] A. Hilal, M.-A. Raulet, C. Martin, and F. Sixdenier, "A Comparative study: dynamic and thermal behavior of Nanocrystalline and Powder magnetic materials in a power converter application," *Journal of Electronic Materials,* vol. 44, no.10, pp. 3768-3776, 2015.

[237] G. Herzer, "Modern soft magnets: Amorphous and nanocrystalline materials," *Acta Materialia,* vol. 61, no.3, pp. 718-734, 2013.

[238] R. Chen, Z. Dong, Z. Zhang, H. Gui, J. Niu, R. Ren*, et al.*, "Core Characterization and Inductor Design Investigation at Low Temperature," in *2018 IEEE Energy Conversion Congress and Exposition (ECCE)*, 2018, pp. 4218-4225.

[239] S. Balci, I. Sefa, and M. B. Bayram, "Core material investigation of medium-frequency power transformers," in *Power Electronics and Motion Control Conference and Exposition (PEMC), 2014 16th International*, 2014, pp. 861-866.

[240] H. Chan, K. Cheng, T. Cheung, and C. Cheung, "Study on magnetic materials used in power transformer and inductor," in *Power Electronics Systems and Applications, 2006. ICPESA'06. 2nd International Conference on*, 2006, pp. 165-169.

[241] A. Castaldo. *Switching regulator fundamentals Application Report Switching regulator fundamentals*. [Online]. Available: http://www.ti.com/lit/an/snva559c/snva559c.pdf. [Accessed: 5- Dec-2018]

[242] Magnetics. *Magnetic Cores for Switching Power Supplies*. [Online]. Available: https://www.mag-inc.com/Media/Magnetics/File-Library/Product%20Literature/General%20Information/ps-01.pdf?ext=.pdf [Accessed: 26- Jan-2018]

[243] Magnetics. *Magnetic Cores For Switching Power Supplies*. [Online]. Available: www.mag-inc.com/getattachment/e9423fd3-3a4f-43a8-b857-0dfe08dc83db/ps-02.pdf?lang=en-US . [Accessed: 23- Feb-2018]

[244] E. D. Langlois, T. C. Monson, D. L. Huber, and J. Watt, "Finite element modeling of nanoscale-enabled microinductors for power electronics," *Journal of Materials Research,* vol. 33, no.15, pp. 2223-2233, 2018.

[245] *Magnetics - Core Loss Calculation*. [Online]. Available: https://www.mag-inc.com/Design/Design-Guides/Powder-Core-Loss-Calculation. [Accessed: 24-Oct-2018]

[246] R. Garcia, A. Escobar-Mejia, K. George, and J. C. Balda, "Loss comparison of selected core magnetic materials operating at medium and high frequencies and different excitation voltages," in *Power Electronics for Distributed Generation Systems (PEDG), 2014 IEEE 5th International Symposium on*, 2014, pp. 1-6.

[247] R. Likert, "A technique for the measurement of attitudes," *Archives of psychology,* 1932.

[248] B. Dehghan-Manshadi, H. Mahmudi, A. Abedian, and R. Mahmudi, "A novel method for materials selection in mechanical design: combination of non-linear normalization and a modified digital logic method," *Materials & design,* vol. 28, no.1, pp. 8-15, 2007.

[249] R. W. Saaty, "The analytic hierarchy process—what it is and how it is used," *Mathematical modelling,* vol. 9, no.3-5, pp. 161-176, 1987.

[250] R. Nasiri-Zarandi, M. Mirsalim, and A. Cavagnino, "Analysis, optimization, and prototyping of a brushless DC limited-angle torque-motor with segmented rotor pole tip structure," *IEEE Transactions on Industrial Electronics,* vol. 62, no.8, pp. 4985-4993, 2015.

[251] W. G. Hurley, T. Merkin, and M. Duffy, "The performance factor for magnetic materials revisited: The effect of core losses on the selection of core size in transformers," *IEEE Power Electronics Magazine,* vol. 5, no.3, pp. 26-34, 2018.

[252] W. Zhuang, S. Li, X. Zhang, D. Kum, Z. Song, G. Yin*, et al.*, "A survey of powertrain configuration studies on hybrid electric vehicles," *Applied Energy,* vol. 262, p. 114553, 2020.

[253] J. P. F. Trovão and P. J. G. Pereirinha, "Control scheme for hybridised electric vehicles with an online power follower management strategy," *IET Electrical Systems in Transportation,* vol. 5, no.1, pp. 12-23, 2015.

[254] J. Sakly, A. B. B. Abdelghani, I. Slama–Belkhodja, and H. Sammoud, "Reconfigurable DC/DC Converter for Efficiency and Reliability Optimization," *IEEE Journal of Emerging and Selected Topics in Power Electronics,* vol. 5, no.3, pp. 1216-1224, 2017.

[255] R. M. Schupbach and J. C. Balda, "Comparing DC-DC converters for power management in hybrid electric vehicles," in *IEEE International Electric Machines and Drives Conference, 2003. IEMDC'03.*, 2003, pp. 1369-1374 vol.3.

[256] M. Ortuzar, J. Moreno, and J. Dixon, "Ultracapacitor-Based Auxiliary Energy System for an Electric Vehicle: Implementation and Evaluation," *IEEE Transactions on Industrial Electronics,* vol. 54, no.4, pp. 2147-2156, 2007.

[257] M. Beraki, J. P. Trovão, and M. Perdigao, "Design of Variable Inductor for Powertrain DC-DC Converter," in *2019 IEEE 28th International Symposium on Industrial Electronics (ISIE)*, Vancouver, BC, Canada, 2019, pp. 822-827.

[258] M. Beraki, J. P. Trovão, and M. Perdigao, "Comprehensive Comparison and Selection of Magnetic Materials for Powertrain DC-DC Converters," *IET Electrical Systems in Transportation,* 2019.

[259] H. Ye, P. Magne, B. Bilgin, S. Wirasingha, and A. Emadi, "A comprehensive evaluation of bidirectional boost converter topologies for electrified vehicle applications," in *IECON 2014 - 40th Annual Conference of the IEEE Industrial Electronics Society*, Dallas, TX,USA, 2014, pp. 2914-2920.

[260] G. C. Goodwin, S. F. Graebe, and M. E. Salgado, *Control system design*: Upper Saddle River, NJ: Prentice Hall, 2001.

[261] W. Xiao, *Photovoltaic power system: modeling, design, and control*: John Wiley & Sons, 2017.

[262] P. Magne, L. Ping, B. Bilgin, and A. Emadi, "Investigation of impact of number of phases in interleaved dc-dc boost converter," in *2015 IEEE Transportation Electrification Conference and Expo (ITEC)*, 2015, pp. 1-6.